

A Study on the Microstructure, Rate-Dependent Mechanical Responses, and Failure Mechanisms
of a Novel TiAl/Ti₃Al-Al₂O₃ Cermet

by

Haoyang Li

A thesis submitted in partial fulfillment of the requirements for the degree of

Master of Science

Department of Mechanical Engineering
University of Alberta

© Haoyang Li, 2019

Abstract

Faculty of Engineering

Department of Mechanical Engineering

Master of Science

By Haoyang Li

Detailed characterization and experimental studies have been carried out on a novel self-propagating high-temperature synthesized $(\gamma + \alpha_2) - \text{TiAl}/\text{Ti}_3\text{Al}-\text{Al}_2\text{O}_3$ cermet to investigate the microstructure, rate-dependent mechanical response, and rate-dependent failure mechanisms under uniaxial compressive loading. Cermet materials have gained significant research attentions recently in structural applications because they process greater ductility and toughness over most advanced ceramics while maintaining moderate strength and hardness. To apply a material in full-scale industrial applications, a comprehensive understanding of the material microstructure and its rate-dependent responses is critical. For the $(\gamma + \alpha_2) - \text{TiAl}/\text{Ti}_3\text{Al}-\text{Al}_2\text{O}_3$ cermet studied in this thesis, limited information is provided in the literature regarding the mechanical properties, stress-strain response, failure mechanisms, and their rate-dependency. This thesis seeks to address this gap and provide an in-depth investigation of the $(\gamma + \alpha_2) - \text{TiAl}/\text{Ti}_3\text{Al}-\text{Al}_2\text{O}_3$ cermet. This thesis consists mainly of two parts, which are adapted from the two published journal articles written by the author. A progressive study has been carried out in this thesis by first examining the as-received material microstructure, followed by a series of mechanical testing and post-mortem analysis.

In the first part of this thesis, the micro/nanostructural features and mechanical responses of the $(\gamma + \alpha_2) - \text{TiAl}/\text{Ti}_3\text{Al}-\text{Al}_2\text{O}_3$ cermet were explored. The material composition, phase distribution, and

elemental concentration were characterized. Three phases were identified in the cermet, including γ -TiAl, α_2 -TiAl, and Al_2O_3 . The material exhibited ultrafine microstructure, with the size of alumina particles between 0.5 microns to 1.5 microns and occupying $65 \pm 1\%$ areal fraction of the material. Some alumina particles are connected to form clusters in the material, where a heterogeneous and complex microstructure is observed. Transmission electron microscopy investigation found iron/nickel-based nano-precipitates, and these were believed to be contributing to the mechanical properties of the material. The rate-dependency on the compressive strength, stress-time history profile, and failure mechanisms were studied by quasi-static and dynamic uniaxial compression. Surface texturing behavior was observed under dynamic loading condition using high-speed imaging, which was further explored in the second part of this thesis.

In the second part of this thesis, the rate-dependent mechanical properties and failure of the cermet were investigated using mechanical testing and advanced characterization tools. Quasi-static and dynamic uniaxial compression tests coupled with high-speed imaging and digital image correlation were used to determine the rate-dependency of stress-strain behavior, compressive strength, and failure strain. The stress-strain curves in the dynamic experiments exhibited a series of alternating stress relaxation and strain hardening cycles, where a 1.3 times increase in compressive strength from 2780 ± 60 MPa to 3410 ± 247 MPa, and a 1.4 times increase in failure strain from 0.0166 ± 0.0017 to 0.0264 ± 0.0032 were determined with a seven order increase in strain rates from $\sim 10^{-4}$ s^{-1} to $\sim 10^3$ s^{-1} . The scatter in strength and failure strain measurements indicate large variability in the material, especially for such composites with complex microstructures. Advanced characterization tools, including scanning electron microscopy, high-resolution (scanning) transmission electron microscopy, and two-dimensional x-ray diffraction were used to map out the failure mechanisms activated under the different loading rates, specifically focused on identifying

causalities of the texturing and soften/hardening cycling. Globally distributed dislocations and twinning were observed as a consequence of dynamic loading, and extensive cleavage in the titanium aluminide phase, void growth, transgranular cracking, and particle fracture were identified as dominant failure mechanisms activated under high strain rate loading. Crystalline texturing with profound microstructural evolution in the titanium aluminide phase was also found under dynamic loading, and this was correlated with the macroscopic surface texturing observed using high-speed imaging and the cyclical stress relaxation and strain hardening behavior in the stress-strain curves. The crystalline texturing, which manifested globally as the surface texturing behavior, is thought to be the consequence of dynamic recrystallization and grain reorientation, although additional studies are needed.

Overall, this thesis presents: 1. A preliminary data set of the $(\gamma + \alpha_2) - \text{TiAl/Ti}_3\text{Al-Al}_2\text{O}_3$ cermet for material design, manufacturing, and modeling of advanced cermets; and 2. A thorough understanding of the rate-dependency of the $(\gamma + \alpha_2) - \text{TiAl/Ti}_3\text{Al-Al}_2\text{O}_3$ cermet and provides insights in cermet material micromechanical modeling and improvement.

Preface

(Mandatory due to collaborative work)

Chapter 3 of this thesis has been published as Li, H. Y., P. Motamedi, and J. D. Hogan. "Characterization and mechanical testing on novel $(\gamma + \alpha_2)$ -TiAl/Ti₃Al/Al₂O₃ cermet." *Materials Science and Engineering: A* 750 (2019): 152-163. I, the first author of this publication, was responsible for conducting experiments, operating some of the characterization apparatuses (e.g., scanning electron microscopy), data collection and analysis, and manuscript composition. Pouyan Motamedi, the co-author of this publication, provided the x-ray diffraction and transmission electron microscopy data and contributed to manuscript edits. Dr. James Hogan, my supervisor, defined the scope of this publication, provided guidance in experiments and data analysis, and contributed to manuscript edits as well.

Chapter 4 of this thesis is under reviewed in *Composite Part B: Engineering* at the date of submission. I, the first author of this publication, was responsible for conducting experiments, operating some of the characterization apparatuses (e.g., scanning electron microscopy), data collection and analysis, and manuscript composition. Pouyan Motamedi, the co-author of this publication, provided the x-ray diffraction and contributed to manuscript edits. The transmission electron microscopy data presented in this work was in collaboration with EAG Laboratories, from which they provided the micrographs and I conducted all the analysis. Dr. James Hogan, my supervisor, defined the scope of this publication, provided guidance in experiments and data analysis, and contributed to manuscript edits as well.

“The greatest enemy of knowledge is not ignorance; it is the illusion of knowledge.”

-Stephen Hawking

Dedicated to my family and friends

Acknowledgement

This research was sponsored by the Natural Sciences and Engineering Research Council of Canada (Grant #2016-04685) with support from PRE Labs Inc. and Lumiant Corporation.

I would like to begin by thanking my supervisor, Dr. James Hogan, whose knowledge, expertise, and patience were critical to the success of my study and completion of this thesis. His guidance from the beginning of my research played a profound role for me to develop excellent research skills, outstanding writing and planning capabilities, and obtained great collaborative opportunities. His expertise in material science and experimental mechanics provided me confidence to pursue the research topic of this thesis, and his approachability and kindness gave me the feeling of a family during the period I spent in the group. Without his helps, this work would not be possible and for that I am truly grateful.

Next, I would like to extend my appreciation to my groupmates, especially to Benhour Amirian, Calvin Lo, Brendan Koch, and Pouyan Motamedi, for their countless helps in my projects, which supported me throughout my degree. I would like to thank Benhour, who jointly worked in the same project with me, gave me great ideas on how to proceed with my research and taught me valuable knowledge on material modeling. I would like to thank Calvin Lo, who would tolerate my endless complaints and show interest in my results. I would also like to think him for the support during my experiments, where numerous mistakes could happen without his helps. I would like to thank Brendan Koch, who showed great interests in my research and gave me invaluable opinions during group meetings. Furthermore, I would like to express my gratitude to Pouyan, for his patience when I started asking “stupid” questions on x-ray diffraction and crystallinity. Your expertise in material science contributed greatly in our papers, and your passion towards new

things will always motivate me. For other groupmates (Kapil Bhagavathula, Piotr Nicewicz, and Michael Conway, etc.), I would like to thank the warm environment you guys gave me during my degree, and the success of this thesis would not be possible without you. Here, I sincerely wish you all the best, and good luck on your future research and careers.

Furthermore, I would like to express my appreciation to the supporting staff at the University of Alberta and the Mechanical Engineering machine shop, especially to the legend Bernie Faulkner for his helps in running experiments and his insightful conversations. His appearance made the whole experiments filled with efficiency and joys. I sincerely wish you all the best in your retired life and keep up the funs and joys everyday with your family.

Last, but certainly not the least, I would like to thank my family and friends for giving me countless care and patience throughout the last two years. Your support gave me the strength and motivation to push through the degree and for that I am grateful. These encouragements will definitely accompany me in the future whenever I face a wall and hesitate to move on.

Contents

Abstract.....	ii
Preface.....	v
Acknowledgement	viii
List of Figures.....	xiii
List of Tables	xxi
Abbreviations.....	xxii
Symbols.....	xxiii
Chapter 1: Introduction.....	1
1.1 Motivations on studying cermets	1
1.1.1 Developments of Metallic Matrix Composites and Cermets.....	1
1.2 Thesis Objectives	5
1.3 Thesis Goals.....	6
1.4 Contributions.....	6
1.5 Thesis Structure.....	8
Chapter 2: Motivations for Studying the TiAl/Ti ₃ Al-Al ₂ O ₃ Cermet.....	10
2.1 The Novelty and Attractive Properties of the TiAl/Ti ₃ Al-Al ₂ O ₃ Cermet for Protection Applications	10
2.2 Using Advanced Material Characterization Techniques in Understanding Material Microstructures	13

2.3 Rate-Dependent Properties and Mechanisms and Importance in Protection Applications	14
Chapter 3: Characterization and Mechanical Testing on Novel ($\gamma + \alpha_2$) - TiAl/Ti ₃ Al/Al ₂ O ₃ Cermet.....	17
Chapter 4: On the Rate-Dependency of Mechanical Properties and Failure Mechanisms of a ($\gamma + \alpha_2$) - TiAl/Ti ₃ Al-Al ₂ O ₃ Cermet.....	51
Chapter 5: Concluding Remarks.....	111
5.1 Conclusion.....	111
4.2 Implication	113
4.3 Future Works and Recommendations	115
Bibliography.....	117
Appendix A: Self-Propagating High-Temperature Synthesis (SHS): A Brief Summary.....	148
Appendix B: Digital Image Correlation (DIC): A Brief Summary	152
B.1 A Brief Summary of the DIC theory	152
B.2 Speckle Pattern.....	156
Appendix C: Supplementary Scanning Electron Microscopy/Transmission Electron Microscopy Micrographs.....	159
C.1 As-received material.....	159
C.2 Fracture surface of fragments recovered from quasi-static testing.....	161
C.3 Polished fracture surface of fragments recovered from quasi-static testing.....	163

C.4	Fracture surface of fragments recovered from dynamic testing	164
C.5	Polished fracture surface of fragments recovered from dynamic testing	165
C.6	TEM investigation on the as-received material	167
C.7	TEM investigation on the dynamically deformed material	168

List of Figures

- Figure 1.1: Schematic depictions of the three main MMC systems, categorized through the types of reinforcements used. This image is taken from the book titled “Comprehensive Composite Materials” written by Anthony Kelly and Carl Zweben [3].....3

- Figure 3.1: Schematic of the MTS machine experimental setup.....25

- Figure 3.2: Schematic of the modified Split Hopkinson Pressure Bar (SHPB) experimental setup.....27

- Figure 3.3: EDS concentration mapping with BSE-SEM image showing the distributions of selected elements. The concentration of the elements is ordered based on the color sequence in the visible light spectrum with a color bar shown below the maps. (a) FESEM image showing the phase distribution, where the black regions correspond to the alumina phase and the white regions correspond to the titanium aluminide phase; (b) Distribution and concentration of Al in the FESEM image; (c) Distribution and concentration of O in the FESEM image; (d) Distribution and concentration of Ti in the FESEM image.....31

- Figure 3.4: XRD spectrum of the cermet showing three distinct phases presented in the material. The legend shows the phases associated with each color, along with their corresponding space groups.....33

- Figure 3.5: Transmission electron micrographs showing: (a) Individual alumina particles (darker) and the “coral” network formed by connected alumina particles under bright field mode, (b) corresponding EDS map of titanium further proves the composition of particles and highlights the alumina network, and (c) the grain boundary between two titanium aluminide grain.....34

- Figure 3.6: EDX mapping of a TEM micrograph on the TiAl grain showing compositions and distributions of the nano-precipitates on the grain. (a) TEM micrograph of a TiAl grain showing white “dots” distributed throughout, (b) Distribution of the iron element on the grain where “green” indicates the presence of iron, and (c) Distribution of nickel element on the grain where “red” indicates the presence of nickel.....35

- Figure 3.7: Stress history in quasi-static uniaxial compression with corresponding images at six different times showing the failure process of the material.....37

- Figure 3.8: Stress history in dynamic (SHPB) uniaxial compression with corresponding images at six different times. The red arrow shows the formation of the primary crack, the blue arrows shows the formation of the secondary cracks, and the dashed circle indicates the formation of the texturing.....40

- Figure 3.9: Semi-log plot of the compressive strength of the cermet with respect to the strain rates under uniaxial loading.....41

- Figure 3.10: Summary of the compressive strength of the cermet with respect to strain rate under uniaxial compression with comparison to alumina AD995 manufactured by Coorstek. The alumina data was gathered from both experiments conducted in the author’s lab and data reported in literature.....48

- Figure 4.1: SEM and TEM micrographs examining the microstructural features of the as-received material. (a) BSE-SEM image on the polished surface showing the phase distribution and alumina clusters; the black regions correspond to the alumina phase and the white regions correspond to the titanium aluminide phases; (b) FESEM image on cleaned fracture surface showing shapes and sizes of alumina and titanium aluminide grains; the red arrows indicate the individual alumina grains, and the blue arrows point to the $(\gamma + \alpha_2) - \text{TiAl/Ti}_3\text{Al}$ lamellae. The titanium aluminide phase appears grayer in the image than the brighter alumina grains; (c) Bright field TEM image showing grain surfaces and grain boundaries. Residual stresses are present on most of the alumina grains, where dislocations (white arrows) and microcrack (red arrow) are observed on the alumina grain at the top left corner. Duplex microstructure of titanium aluminide phase, including clean γ grains and $(\gamma + \alpha_2)$ lamellae on γ grains are obtained. No specific orientation of the lamellar structure is found in the as-received material.....66

- Figure 4.2: (a) Schematic of the 2D-XRD test setup and scan parameters; (b) A representative 2D frame showing typical arcs indicating a random orientation and a preferred orientation. The directions of integration (θ and Ψ) are from right to left and from bottom to top, respectively.....69

- Figure 4.3: (a) A typical speckle pattern produced for DIC analysis for the quasi-static test. The compressive loading direction is vertical. (b) A typical speckle pattern produced for DIC analysis for the dynamic test. The compressive loading direction is vertical. Metallic paint was used for both cases in (a) and (b). The painted surfaces are always the biggest surface (2.7 mm x 3.5 mm) of the specimens. Isotropic and highly contrasted speckle patterns are obtained in both (a) and (b).....74

- Figure 4.4: (a) Stress-strain curves of the TiAl/Ti₃Al-Al₂O₃ cermet under quasi-static uniaxial compression. The $\epsilon = 0.001$ strain line indicates where the stiffnesses are computed; (b) Still images showing typical post-peak structural fragments corresponding to two of the tests (QS sp1 & QS sp5) in (a). The data points on the x-axis in (a) are indications of when the images are extracted. The arrows shown in the fragment images are evidence of lamellar tearing along the loading direction, as one of the fracture modes under quasi-static loading.....78

- Figure 4.5: (a) Stress-strain curves for dynamic uniaxial compression tests. The $\epsilon = 0.1\%$ strain line indicates where the stiffnesses are computed for each curve; (b) A sequence of still images of sample DYN sp2 showing typical post-peak fracture paths of the cermet under dynamic loading. The red dot shown on the x-axis in (a) indicates the starting point of when the images are extracted. The red arrows in the images in (b) show a primary split crack along the loading direction, and the blue arrows show crack branching from the primary cracks, as well as cracks activated during further loading; (c) A sequence of representative still images taken from the tests using unpainted specimen to reveal the surface deformation features. The red circle highlights where the texturing is observed on the specimen surface. Splitting and branching cracks are also identified that are similar to (b).....82

- Figure 4.6: Semi-log plot of the uniaxial compressive strength of the TiAl/Ti₃Al-Al₂O₃ cermet as a function of the strain rate. The dynamic compressive strength is approximately 1.3 times the quasi-static compressive strength with an seven order increase in strain rate (from $\sim 10^{-4} \text{ s}^{-1}$ to $\sim 10^3 \text{ s}^{-1}$). In addition, the material appears to be more rate sensitive at high strain rates.....83

- Figure 4.7: Micrographs taken on the fracture surface showing the fractography of the TiAl/Ti₃Al-Al₂O₃ cermet under quasi-static uniaxial compression. (a) A global view of the crack propagation, where the yellow arrows indicate the compressive loading direction, and the blue arrows indicate the intergranular fracture in the titanium aluminide matrix and cleavage in the titanium aluminide lamellar planes; (b) A magnified view in the vicinity of the crack in (a) showing typical deformation mechanisms, including grain boundary delamination, particle pull-out, and dimpling; (c – f) FESEM image with the corresponding EDS maps showing the phases where the intergranular fracture happens. (c) FESEM micrograph showing an intergranular crack passing through the field of view, where a triple junction is formed; (d) Distribution of the Al element in the FESEM image; (e) Distribution of the O element in the FESEM image; (f) Distribution of the Ti element in the FESEM image. In each EDS map, a brighter color indicates a higher concentration of such element.....86

- Figure 4.8: Micrographs showing the fractography of the TiAl/Ti₃Al-Al₂O₃ cermet under dynamic uniaxial compression. (a – b) FESEM images taken on the polished fracture surface revealing the sub-surface damage of the cermet. (a) Extensive particle fracture and particle interface fracture are observed in the alumina phase (phase with darker color), and a crack (indicated by a white arrow) propagates along and through the alumina particles with void growth identified on the crack path; (b) A global view of the sub-surface damage on the polished fracture surface showing the density of the void growth (shown as dark color) under dynamic compressive loading. (c – e) FESEM images taken on the fracture surface showing different deformation mechanisms activated in the material. (c) A typical fracture plane under dynamic loading showing extensive amounts of cleavage in the titanium aluminide matrix; (d) A magnified view on three of the major fracture sites in the material, including particle fracture, matrix fracture, and intergranular fracture; (e) A microcrack propagates through the field of view horizontally with (f) the corresponding Al element map to identify the phases along the crack. Particle pull-out is also observed on the fracture surface in (e).....89

- Figure 4.9: TEM micrographs showing microstructure evolution under dynamic uniaxial compressive loads. (a) A global view of the TEM lamella showing the alumina clusters (lighter regions) and the titanium aluminide lamellae (darker regions). The orientation of the titanium aluminide lamellae (red arrow) is approximately 30° with respect to the horizontal plane. (b) SAED pattern corresponding to the circled region in (a) identifying the presence of γ and α_2 lamellae. The orientation is specified in the figure, and it corresponds to the lamellar orientation in (a). (c – e) Bright field TEM on the alumina-titanium aluminide boundary and the corresponding EDS maps showing the lamellae compositions. The alumina-titanium aluminide boundary is identified by dashed lines in (c). In each EDS map, a brighter color indicates a higher concentration of the corresponding element. (f) High-resolution TEM showing crystalline lattice structure of an adjacent γ/α_2 lamellae. The grain boundary is indicated by a dashed red line.....92

- Figure 4.10: Bright field TEM micrograph showing the deformation mechanisms activated under dynamic uniaxial compressive loads. (a) Residual stress (appeared as dark contour lines) and dislocations (indicated by white arrows) are observed on the alumina grains. A microcrack (indicated by a red arrow) is initiated from the dislocation tip and propagate through the alumina grain. (b) Delamination occurs at the alumina-titanium aluminide grain boundary. Nano-twins (indicated by yellow arrows) are observed crossing the titanium aluminide lamellar boundaries and forming periodic curved structures. (c) Different types of dislocation activities, including dislocation walls, networks, and tangling are observed within titanium aluminide lamellae and at the lamellar boundaries. (d) High-resolution TEM micrograph showing dislocation pileup at the alumina-titanium aluminide grain boundary.....95

- Figure 4.11: X-ray diffraction analysis of the as-received TiAl/Ti₃Al-Al₂O₃ cermet, and of a polished fracture surface taken from a quasi-static fragment and a dynamic fragment showing phases changes and crystallinity evolution during uniaxial compressive loading at different strain rates. (a) $\theta - 2\theta$ equivalent spectrum plots showing an amorphous peak occurs in the dynamic fragment, where no additional phase changes occur under both quasi-static and dynamic loading; (b) 2D diffraction frame revealing crystalline texturing evolves at different loading rates. The light intensity is integrated from right to left to obtain the 1-D spectrums. Typical peaks corresponding to the three phases are pointed out by red arrows to show the texturing evolution in different phases. Significant crystalline texturing is observed in the dynamic fragment on both γ -TiAl and α_2 -Ti₃Al phases, whereas alumina phase remains in its randomly orientated polycrystalline structure.....98

- Figure 4.12: Summary of the compressive strength of the cermet at different strain rates (in log scale). A curve fit in the form of $\sigma_c = a * \dot{\epsilon}^n + \sigma_{Qs_{avg}}$ is used to determine the rate-dependency exponent, n , for compressive strength as well as the transitional strain rate. This is evaluated to be 80 to 500 s⁻¹. This method has been used widely in studying the rate dependency of brittle materials [89, 90]. The fitted coefficient, “ a ” is close to 1 with a R^2 value of 0.9, indicating a good fit.....105

- Figure A.1: Reaction model of 3TiO₂-7Al powder at high temperatures. This image is taken from Shen et al. [51].....141

- Figure B.1: Schematic of a reference subset before deformation and a target subset after deformation. The center position of the target subset is obtained through searching the peak position of the distribution of the correlation coefficient. The insert shows a 3 x 3 local discrete correlation coefficient distribution, where $C(0,0)$ is the point with the maximum correlation coefficient obtained from an integer pixel displacement searching scheme. This image is taken from Pan [75, 76].....144

- Figure B.2: Flowchart summarizing data processing procedures by using the testing apparatus coupled with digital image correlation to obtain stress-strain curves with MATLAB.....149

- Figure C.1: FE-SEM image of polished as-received specimen surface showing surface features, such as pores and defects.....150

- Figure C.2: The corresponding BSE-SEM micrograph of Fig. C1 showing phase distribution.....151

- Figure C.3: FE-SEM micrograph showing a magnified view of the pores on the polished as-received specimen surface.....151

- Figure C.4: FE-SEM micrograph on the fracture surface (not from testing) of the specimen showing two-phase titanium aluminide lamellar structure, equiaxed titanium aluminide and alumina grains.....152

- Figure C.5: FE-SEM micrograph on the fracture surface of a fragment recovered from quasi-static testing showing intergranular cracking and particle delamination.....152

- Figure C.6: FE-SEM micrograph on the fracture surface of a fragment recovered from quasi-static testing showing tearing of the titanium aluminide phase (gray color).....153

- Figure C.7: FE-SEM micrograph on the fracture surface of a fragment recovered from quasi-static testing showing a dominating crack formed roughly in the direction of compression.....153

- Figure C.8: FE-SEM micrograph on the fracture surface of a fragment recovered from quasi-static testing showing particle pulled-out in the vicinity of a microcrack.....154

- Figure C.9: FE-SEM micrograph on the polished fracture surface of a fragment recovered from quasi-static testing showing a microcrack across the field of view with voids along the path.....154

- Figure C.10: FE-SEM micrograph on the polished fracture surface of a fragment recovered from quasi-static testing showing some void growth (black dots). Minimum amount of particle fractures is observed.....155

- Figure C.11: FE-SEM micrograph on the fracture surface of a fragment recovered from dynamic testing showing extensive cleavage of the titanium aluminide phase and alumina particle pulled-out.....155

- Figure C.12: FE-SEM micrograph on the fracture surface of a fragment recovered from dynamic testing showing planar tearing of titanium aluminide and alumina particle fracture.....156

- Figure C.13: FE-SEM micrograph on the polished fracture surface of a fragment recovered from dynamic testing showing extensive void growth within or surrounding the alumina phase (gray).....156

- Figure C.14: FE-SEM micrograph on the polished fracture surface of a fragment recovered from dynamic testing showing a triple junction of microcracks and extensive particle fracture. Transgranular fracture is also dominant.....157

- Figure C.15: FE-SEM micrograph on the polished fracture surface of a fragment recovered from dynamic testing showing a magnified view of particle fracture. The extent of particle damage along and in the vicinity of a microcrack is significant.....157

- Figure C.16: (a) S-TEM micrograph on an as-received specimen showing individual alumina grains and alumina clusters (gray). The titanium aluminide phase exhibits randomly orientated lamellar structure and equiaxed grains; (b) Corresponding Ti element map of (a); (c) Corresponding Al element map of (a); (d) Corresponding O element map of (a).....158

- Figure C.17: Bright field TEM micrograph on an as-received specimen showing a magnified view of an alumina grain, where dislocations and residual stresses resulting from manufacturing are observed.....158

- Figure C.18: (a) S-TEM micrograph on a dynamically deformed specimen showing alumina clusters (gray). The titanium aluminide phase exhibits uniformly orientated lamellar structure and no equiaxed grains is observed; (b) Corresponding Ti element map of (a); (c) Corresponding Al element map of (a); (d) Corresponding O element map of (a).....159

- Figure C.19: Bright field TEM micrograph on a dynamically deformed specimen showing uniformly orientated ($\gamma + \alpha_2$) titanium aluminide lamellar structure with extensive dislocations located in between the lamella.....159

- Figure C.20: Dark field TEM micrograph on a dynamically deformed specimen focusing on the lamellar structure. A large variation of lamellar width is observed. EDS examination demonstrates an alternating γ/α_2 feature.....160

- Figure C.21: Bright field TEM micrograph on a dynamically deformed specimen showing twinning within a lamellae.....160

- Figure C.22: High-resolution TEM micrograph on a dynamically deformed specimen showing dislocation pileup at the alumina (white)-titanium aluminide (black) interface.....161

List of Tables

- Table 2.1: As-received mechanical properties with comparison to 99.5% purity alumina by Coorstek. Inc.....13

- Table 3.2: The weight and the atomic percentage of the primary and secondary elements present in the EDS scan. Here carbon, zirconium, and potassium are considered as the secondary elements in the material.....32

- Table 4.1: Equations for the algorithm and software settings used for DIC analysis in both quasi-static and dynamic tests.....75

Abbreviations

γ -TiAl	Gamma-phase Titanium Aluminide
α_2 -Ti ₃ Al	Alpha2-phase Titanium Aluminide
Al ₂ O ₃	Aluminum Oxide/Alumina
MMC	Metal Matrix Composite
SHS	Self-propagating High-temperature Synthesis
EDM	Electron Discharge Machining
SEM	Scanning Electron Microscopy
BSE	Back-Scatter Electron
(HR)-(S)TEM	(High-Resolution)-(Scanning)Transmission Electron Microscopy
EDS	Energy-Dispersive X-ray Spectroscopy
SAED	Selected Area Electron Diffraction
XRD	X-Ray Diffraction
FIB	Focus Ion Beam
SHPB	Split-Hopkinson Pressure Bar
DIC	Digital Image Correlation
AOI	Area Of Interest
ZNSSD	Zero-Normalized Sum of Squared Difference

Note: Only major abbreviations are listed here.

Symbols

a	Fitted coefficient	Unitless
A_s	Cross-sectional area of the specimen	m^2
A_o	Cross-sectional area of the bar	m^2
c	Material sound velocity	m/s
D	Diameter of the projectile	m
E	Stiffness of the ceramic target	MPa
E_0	Stiffness of the bar	Pa
$f(x_i, y_j)$	Intensity function (reference frame)	Unitless
$g(x'_i, y'_i)$	Intensity function (deformed frame)	Unitless
HV	Vickers hardness	MPa
K_{Ic}	Fracture toughness	$MPa \cdot m^{\frac{1}{2}}$
m	Mass of the projectile	Kg
M	Subset dimension	Pixel
n	Rate-dependency exponent	Unitless
P_0	Reference penetration of projectile in backing rolled homogeneous armor	m
P_r	Residual penetration of projectile in backing rolled homogeneous armor	m
R_s	Rate sensitivity	Unitless
t_c	Target thickness	m
T	Thickness of the projectile	m

V_{50}	Ballistic limit	m/s
(x_i, y_i)	Coordinate of interpolation point (reference frame)	Pixel
(x'_i, y'_i)	Coordinate of interpolation point (deformed frame)	Pixel
ρ_0	Density of the backing rolled homogeneous armor	kg/m ³
ρ_t	Density of the target	kg/m ³
σ_{max}	Peak stress	MPa
$\sigma(t)$	Time-resolved nominal axial stress	Pa
σ_c	Peak compressive strength	MPa
σ_d	Dynamic flow stress (at a constant plastic strain)	MPa
σ_e	Quasi-static compressive strength of the target (used in ballistic limit)	Pa
σ_s	Quasi-static flow stress (at a constant plastic strain)	MPa
σ_{QSavg}	Average quasi-static compressive strength	MPa
ε_t	Time-resolved transmitted strain	Unitless
$\dot{\varepsilon}$	Strain rate	s ⁻¹
$\dot{\varepsilon}_d$	Corresponding dynamic strain rate (at a constant plastic strain)	s ⁻¹
$\dot{\varepsilon}_s$	Corresponding quasi-static strain rate (at a constant plastic strain)	s ⁻¹
2θ	Bragg angle in XRD	°
Ψ	Integration arc angle in 2D-XRD	°
Γ	Projectile constant	Unitless

Chapter 1: Introduction

1.1 Motivations on studying cermets

1.1.1 Developments of Metallic Matrix Composites and Cermets

1.1.1.1 Brief History of Metallic Matrix Composites

Metal Matrix Composites (MMCs) have attracted extensive research interests since the 1960s [1]. The initiation of works on combining metals and different types of reinforcements was the development of consolidated mixtures of aluminum/alumina powders in 1924 by Schmidt [2]. From there, MMCs have been broadly defined as any composites having a metallic (intermetallic included) constituent being the matrix of the material, provided that the reinforcement contents (mainly ceramics) are high enough to possess the load transfer capacity under the influence of stress [3]. The advantages of MMCs can be verified through comparison with conventional metals and the other advanced composite termed polymer matrix composites (PMCs) [4]. With respect to metals, MMCs offer the following advantages [3]:

- High strength-to-weight ratio
- Good dimensional stability
- High elevated temperature stability (i.e., creep strength)
- Improved cyclic fatigue strength

By including a non-metallic phase (e.g., ceramic) into the metallic matrix, the overall density of the composite will decrease because of the lower density of non-metallic phase. Furthermore, the strength (e.g., usually refers to compressive strength in the ceramic case) will generally increase because the higher compression tolerance of ceramics. In addition, due to the strong performance

at high temperature and high hardness, creep and fatigue-related properties are usually also improved [91 – 94].

With respect to PMCs, MMCs offer the following advantages [4]:

- High strength and stiffness
- Improved high-temperature properties
- High electrical and thermal conductivity
- Good transverse properties (PMCs are usually good in unidirectional loading)

In general, three categories (see Fig. 1.1) are defined for MMCs: 1. Monofilaments-reinforced MMCs; 2. Whiskers/fibers-reinforced MMCs; and 3. Particulate-reinforced MMCs. The TiAl/Ti₃Al-Al₂O₃ cermet studied in this thesis belongs to the particulate reinforced MMC category, which is also called the discontinuously reinforced metal composites (DE-MMCs). Starting from the 1980s, the main focus on the DE-MMCs were on Al-based matrices reinforced with SiC particles, Al₂O₃ particles, or short fibers [3]. This type of MMC is worth studying because of several favorable properties they could potentially have [1, 4]:

- High stiffness and hardness
- High workability
- Low density
- Adequate toughness
- Relatively low cost with suitable initial powders and fabrication methods

With the variation of the reinforcement contents, the term “cermet” has been designated to the DE-MMCs where a higher amount of ceramic particulate reinforcements (> 50 vol%) are combined within a metallic matrix [5, 6]. Although some studies [7] claimed a much higher reinforcement

volume percentage ($> 70 \text{ vol\%}$), the definition of cermet remains a vague concept in the materials science community. In this thesis, we adapt the concept of cermet to denote that a significant amount of ceramic phase is integrated into a metallic phase, and it has a permanent effect on the mechanical properties of the original metal. This is chosen instead of defining a specific volume percentage (e.g., $> 70\%$) or specific types of matrix and reinforcements (e.g., TiC reinforced Ni alloy at an early stage [3]) to compensate for the large variety of research conducted and the word “cermet” being used among them.

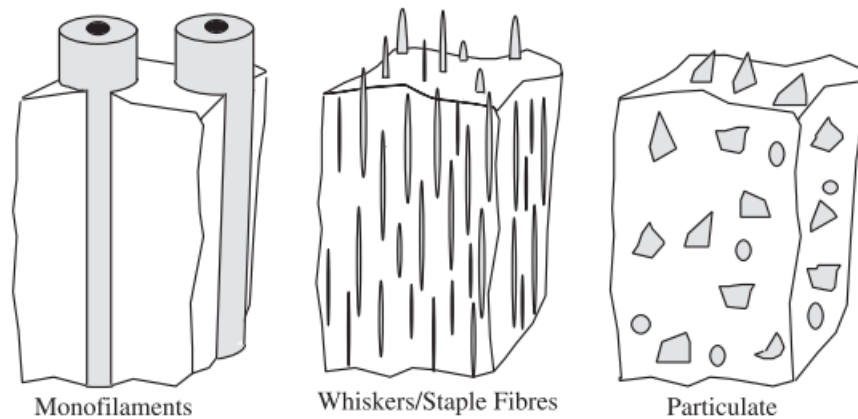


Figure 1.1: Schematic depictions of the three main MMC systems, categorized through the types of reinforcements used. This image is taken from the book titled “Comprehensive Composite Materials,” written by Anthony Kelly and Carl Zweben [3].

1.1.1.2 The Development of Cermets

With high loading of ceramic particles, ceramic networks with connected particles are usually formed in the metallic matrix, and this enhances the load transfer capacity in the material. Thus, the properties of cermets approach that of ceramics, such as high hardness and stiffness but relatively low toughness [3]. As a result of the relatively new concept, researchers have classified cermets in different ways, such as metallic phase, ceramic phase, or based on their intended applications (e.g., Goetzl in 1984 [8], Ettmayer in 1989 [9]). In this thesis, we adapt Mari’s approach [10] since it is the most recent documentation on the history of cermets (published in

2011). In his review, Mari [10] defined three classes of cermet by their refractory components [10]. The first class was called “hardmetal,” and this consists of ceramics that were constituted of carbides, nitrides, borides, and silicides of the metals in the fourth to six groups of the periodic table. The second class was termed “cermet,” and this consists of some of the hardest carbides and nitrides like SiC and B₄C. Large differences in elastic modulus and thermal expansion from metals usually made these cermets of little practical interest. The third class was called “oxide cermet,” which consists of oxide ceramics like Al₂O₃ and ZrO₂. This class of materials’ high resistance to chemicals and the refractory character of these oxide ceramics has stimulated engineering research effort towards cermet development for dental [3] and high strain rate applications, such as ballistic protection applications [4].

While the intended use of cermets has been to replace metallic alloys or monolithic ceramics in some high temperature and high rate applications, such as cutting tools, turbine blades, and aircraft engine components [9, 10], this thesis focuses on exploring interests of the TiAl/Ti₃Al-Al₂O₃ cermet in ballistic protection applications. The interest in using cermets to replace advanced ceramics in body armor has existed since the 1970s (and likely before). The main motivation behind cermet research has been to introduce ductility of metals while preserving some favorable properties of ceramics, such as high stiffness and hardness. This combination of properties was believed to augment their impact performance through a reduction in the depth of penetration and delayed axial cracking [12]. The seminal work of Wilkins et al. [12] in 1969 and Landingham and Casey [13] in 1972 also demonstrated the importance of microstructure (e.g., size and distribution of ceramic phase in the metal) on the impact performance of cermets. Some cermet systems studied in their works were: 1. TiC-steel system; 2. B₄C-Al system; 3. Be₄B-B system; and 4. Be₄B-Ni system. These works served as the foundation for the subsequent studies, which increased in

frequency in the 1990s when fabrication technologies were able to produce cermets at near 100% theoretical densities with comparable hardness and densities to conventional advanced ceramics (e.g., alumina at $\sim 4 \text{ g/cm}^3$). In addition, the wettability between the metallic and ceramic phases improved greatly from advanced fabrication methods, where internal defects decreased considerably due to the better bonding mechanisms. Examples include: $\text{Al}_2\text{O}_3\text{-Al}$ (3.53 to 3.74 g/cm^3) [14], $\text{TiB}_2\text{-B}_4\text{C}$ (3.25 g/cm^3 to 3.6 g/cm^3) [15], $\text{Cr-Cr}_2\text{S}_3$ (4 g/cm^3 to 5.4 g/cm^3) [16], and $\text{B}_4\text{C-Al}$ cermet (2.62 g/cm^3) [17]. In recent works, cermet systems using advanced fabrication methods have been developed for ballistic impact testing. Examples include: EN AC-44200 $\text{Al-Al}_2\text{O}_3$ cermet systems (squeeze casting) [18], $\text{Al-(Al}_2\text{O}_3 \text{ 45 vol\% + TiB}_2 \text{ 10 vol\%)}$ cermet systems (pressure infiltration) [19], and TiC-Ni cermet systems (liquid phase sintering) [6].

1.2 Thesis Objectives

The objective of this thesis is to utilize the advanced characterization tools (e.g., microscopy, crystallography) and high-speed imaging techniques to probe the rate-dependent mechanical properties and failure mechanisms of a $\text{TiAl/Ti}_3\text{Al-Al}_2\text{O}_3$ cermet across different length scales. Once the characterization and mechanical testing data are obtained, they will be linked into a framework for future systematic studies on similar cermet materials and provide a roadmap for studying dynamic failure of particle-reinforced metallic matrix composites. This data will also be valuable in generating micromechanical material models by providing microstructural inputs, rate-dependent mechanical properties, and insights into dynamic failure mechanisms. Finally, the analysis obtained from the as-received material will be used to inform industrial partners for material microstructure refinement and material performance improvement in ballistic protection applications.

1.3 Thesis Goals

Through this research, the goals of this thesis are as follows:

- Systematically characterize the as-received (intact) material by using advanced microscopy (e.g., field emission scanning electron microscopy and x-ray diffraction), obtain microstructural information including phases and compositions, particle size and distribution, porosity and pore size, and nano-precipitates.
- Develop an applicable digital image correlation (DIC) procedure to measure small strains under compression at different loading rates. This includes understanding the DIC theory, creating repeatable and high-quality speckle patterns, assembling a proper lighting system, and mastering in using the DIC software.
- Study the rate-dependent compressive stress-strain responses and mechanical properties by conducting quasi-static and dynamic uniaxial compression tests on a standard MTS machine and split-Hopkinson pressure bar (SHPB) coupled with high-speed imaging and DIC.
- Study the rate sensitivity of the material in terms of peak compressive strength and flow stress and compare with other cermet systems.
- Study the rate-dependent failure mechanisms from postmortem analysis (fragments recovered from mechanical tests) using advanced microscopy and correlate the microscopic mechanism to the macroscopic surface deformation observed using high-speed imaging.

1.4 Contributions

The contributions from this thesis are summarized in the following statements:

- Generate and validate the protocol for using the novel DIC technique in measuring small strains on small-scale brittle specimens.
- Provide inputs for micromechanical material modeling (i.e., microstructure reconstruction) by quantifying microstructural information on the as-received TiAl/Ti₃Al-Al₂O₃ oxide cermet.
- Bridge the gap of a novel self-propagating high-temperature (SHS) synthesized TiAl/Ti₃Al-Al₂O₃ oxide cermet from the experimental mechanics point of view, where most of the literature on this material focuses on the fabrication methods with limited experimental works have been done.
- Address the gap in understanding rate-dependent material properties and failure by exploring the stress-strain behaviors under different loading rates. While most studies have been focusing on obtaining the quasi-static properties (e.g., strength, fracture toughness) of different cermets, understanding the dynamic behaviors of the material are of primary importance in using this material in ballistic protection applications.
- Identify multi-scale failure mechanisms and give insights on the rate-dependent failure of the material and provide sound validations on material modeling. A microstructure-properties relationship is developed through the investigation, and this is crucial in the design of next-generation protection materials.
- Demonstrate the advantages or disadvantages of the current material towards ballistic impact performance by comparing the obtained properties and mechanisms with other advanced ceramics and other cermet systems.

1.5 Thesis Structure

The layout of this thesis is as follows:

- Chapter 1: Introduction of this thesis, including motivations behind MMC and cermet research, important aspects (material science and experimental mechanics) in this thesis, the objectives, goals, and contributions.
- Chapter 2: This chapter explains the motivations behind studying the TiAl/Ti₃Al-Al₂O₃ cermet, which illustrates the novelty of the material and the importance of studying rate-dependent behaviors.
- Chapter 3: This chapter consists of a paper titled “Characterization and Mechanical Testing on Novel ($\gamma + \alpha_2$) - TiAl/Ti₃Al/Al₂O₃ Cermet” that was published in *Material Science and Engineering A* in March 2019 [61]. This first study provided detail characterizations on the as-received material, as well as preliminary mechanical testing results that have not been conducted on similar materials before.
- Chapter 4: This chapter consists of a second paper titled “On the Rate-dependency of Mechanical Properties and Failure Mechanisms of a ($\gamma + \alpha_2$) - TiAl/Ti₃Al-Al₂O₃ Cermet” that is under review by *Composite Part B: Engineering* at the date of submitting this thesis. This second study demonstrated aspects of rate-dependent stress-strain responses, rate-dependent failure mechanisms, and crystalline texturing behavior of the cermet material.
- Chapter 5: The concluding remarks of this thesis, future works, and recommendations towards material testing, design, and modeling will be outlined.

- Appendix A: Brief summary of the self-propagating high-temperature synthesis process.
- Appendix B: Brief summary of the Digital Image Correlation (DIC) technique.
- Appendix C: Supplementary scanning electron microscopy/transmission electron microscopy micrographs.

Chapter 2: Motivations for Studying the TiAl/Ti₃Al-Al₂O₃ Cermet

2.1 The Novelty and Attractive Properties of the TiAl/Ti₃Al-Al₂O₃ Cermet for Protection Applications

The ($\gamma + \alpha_2$) - TiAl/Ti₃Al-Al₂O₃ cermet studied in this thesis belongs to the “oxide cermet” class. Among promising oxide-based cermets materials for protection applications, the TiAl/Ti₃Al-Al₂O₃ cermet possesses a good combination of mechanical properties due to its three major constituents (i.e., γ -TiAl, α_2 -Ti₃Al, Al₂O₃). The two-phase titanium aluminide alloys, including the γ -TiAl and α_2 -Ti₃Al phases, have attracted attention in recent decades because of their low density (3.7 – 4.7 g/cm³), high melting temperature (\sim 1500 °C), and good combination of stiffness (\sim 180 GPa), specific strength (100 – 150 MPa/gcm⁻³), and toughness (11 – 20 MPa \sqrt{m}) [21 – 24]. Owing to its properties advantages towards metals and some other intermetallic alloys, TiAl-based alloys and its composites have become one of the competitive candidates in replacing the much heavier nickel-based superalloys in high-temperature applications (e.g., engine blade) [25]. Furthermore, among the various microstructures and properties shown in different TiAl alloys from diverse solidification paths, the ($\gamma + \alpha_2$) two-phase TiAl alloys consist of lamellar microstructures, and these are superior to most other TiAl alloys in terms of strength and toughness due to its unique microstructure [26]. In addition, because of the advantages demonstrated in particulate reinforced MMCs, adding ceramic particles into the TiAl alloys seems reasonable to further improve their mechanical properties, such as stiffness, hardness, and strength. In this case, alumina (Al₂O₃) with relatively low density (\sim 3.9 g/cm³) and moderate strength in the family of advanced ceramics (e.g.,

stiffness of 370 GPa and compressive strength of 2600 MPa for AD995 reported by Coorstek. Inc. [27]) is still one of the preferred candidates in the defense industry due to its low cost and availability [28].

Before advanced fabrication methods have been developed, particulate reinforced MMCs were often manufactured through infiltrating liquidized metallic/intermetallic alloys into compacted ceramics platforms [82]. These platforms need to be porous enough to allow for the infiltration, and this process usually leads to defective interfacial bonding between the matrix and the reinforcements [30]. The most recent approach to synthesize particulate reinforced MMCs would be the in-situ processes by which the composites are formed through high-temperature chemical reactions. Here the term “in-situ” denotes a sintering process that does not require the initial powder materials to be the exact phases in the final compacted products. Compared to conventional methods, in-situ techniques usually yield better interfacial bonding by direct phase forming through reactions [10], and this further strengthens the materials. With the advancement in in-situ manufacturing techniques such as reaction synthesis (RS) and spark plasma sintering (SPS), combining titanium aluminide alloys with alumina, as is done in our cermet material, seems promising due to their comparable densities ($\sim 3.9 \text{ g/cm}^3$ for both) and coefficients of thermal expansion ($\sim 8.2 \times 10^{-6} / ^\circ\text{C}$ for alumina [27] and $\sim 8.5 \times 10^{-6} / ^\circ\text{C}$ for titanium aluminide [29] at room temperature). In addition, the favorable thermite reactions between aluminum and titanium oxides results in the formation of alumina and metallic or aluminide phases (depending on the oxide used), and the low cost of aluminum and titanium oxide powders make combining aluminum and titanium dioxide attractive for mass production of advanced materials [31]. The TiAl/Ti₃Al-Al₂O₃ cermet studied in this thesis was fabricated through an in-situ self-propagation high-temperature sintering process (SHS), where aluminum (Al) and titanium dioxide (TiO₂) powders

were reacted under extremely high pressure and high temperature (i.e., $T \sim 1733$ K [51]), and the composite was formed within seconds. It is worth noting that the displacement reaction between Al and TiO_2 is exothermic and self-sustained, which makes the system favorable for sintering [32]. Details of the SHS process are documented in Appendix A of this thesis.

Shown in Table 2 are some quasi-static mechanical properties of the TiAl/Ti₃Al-Al₂O₃ (TitanMade L465) cermet studied in this thesis. The material is manufactured by Lumiant Corporation, British Columbia, and this data is provided by the company. Relevant properties of alumina are also listed in the table for direct comparison. The type of alumina ceramic termed “AD995” is used in this study, and it is manufactured by Coorstek, Inc., Colorado. The “995” denotes the density of the alumina (Al_2O_3) in this ceramic is 99.5% of its theoretical value. Alumina is used here for comparison because it is a standard ceramic armor material in use, and this gives a better knowledge of some of the attractive properties of the TiAl/Ti₃Al-Al₂O₃ cermet towards armor applications. The cermet has comparable density with alumina AD995 with an increase in flexural strength and fracture toughness, but with lower stiffness and hardness. This can serve as a preliminary observation on the effect of combining ceramic and metallic materials (in this case, intermetallic to be more specific). For ballistic impact, where dwell (stiffness and hardness dominate) and penetration (toughness dominates) are the two major phases before fragmentation [83], having a combination of relatively high stiffness and hardness and significant ductility seems promising. From this point of view, the TiAl/Ti₃Al-Al₂O₃ cermet could be a competitive candidate in armor applications, but this will be explored in this thesis.

Table 2.1: As-received mechanical properties with comparison to 99.5% purity alumina by Coorstek, Inc.

	TitanMade L465	Al ₂ O ₃ (AD995)
Density (g/cm ³)	3.9	3.9
Stiffness (GPa)	280	370
Hardness (GPa)	11	14.1
Flexural Strength (MPa)	925	375
Fracture Toughness (MPa m ^{1/2})	7.4	4 – 5
Nano-Hardness (GPa)	8 ± 2 (titanium aluminide) 22 ± 8 (alumina)	23 ± 11

2.2 *Using Advanced Material Characterization Techniques in Understanding Material Microstructures*

Characterization of a material is one of the critical parts in understanding material performance and its mechanical responses under loadings. The different stress-strain behavior, mechanical properties, and failure mechanisms of a material are usually an outcome of complex microstructural features. In addition, characterization is crucial in material design and optimization, where significant microstructure changes will occur if other reinforcements like alloying elements and nano-precipitates are introduced, or further processing like heat treatments are performed on the material [84 – 87]. Finally, connecting the specific microstructures to macroscopic material behaviors is important in micromechanical material modeling, and having good characterization can serve as modeling inputs and for validation [64, 88 – 90].

With the advancement of characterization techniques over the past decades, the length scale and accuracy of the investigation on material microstructures and crystallinity has improved

dramatically [57 – 60]. In this thesis, we apply multiple advanced microscopy techniques to qualify and quantify the as-received composition and microstructural, such as percentage volume of the phases, distribution of the alumina networks, alumina particle size, porosity level, pore size, and size of the nano-precipitates and their distributions. Further, we examine the postmortem fragments recovered from mechanical tests to identify the micro/nanoscale failure mechanisms and crystalline texturing. The above works were done by using high-resolution scanning electron microscopy (HR-SEM), high-resolution (scanning) transmission electron microscopy (HR-TEM/STEM), energy-dispersive x-ray spectroscopy (EDS) for both SEM and TEM, and two-dimensional x-ray diffraction (2D-XRD), all of which are presented and discussed in detail in the science chapters of the thesis. With this information, the microstructural features are well informed and ready to correlate with mechanical responses.

2.3 Rate-Dependent Properties and Mechanisms and Importance in Protection Applications

Most of the works in the early stage of cermet research are dedicated to the characterization of quasi-static mechanical properties with influences of the composition and microstructure [30 – 32]. Recently, non-conventional cermets, such as the oxide-based (e.g., Al_2O_3) and hard carbide-based (B_4C) cermets, have gained interest for application in extreme environments, such as high temperature [62, 63] and high loading rates [6, 20]. Therefore, it is reasonable to study the dynamic behaviors of the cermet materials, given that rate-dependent mechanical responses have been well-studied for their individual constituents (i.e., metals and ceramics [33 – 38]). Previous studies on cermets have shown that mechanical properties and fracture mechanisms are rate-dependent. For example, Rittel et al. [39] found that the dynamic fracture toughness of TiC/1080 steel cermet is significantly higher (by about a factor of 3) than its quasi-static counterpart. In another study, Kaplan et al. [40] showed that this increase was likely due to the change in fracture mechanisms

from quasi-static to dynamic condition by visualizing the change in the crack path with the help of transmission electron microscopy. Rate-dependent effects for the compressive strength were also studied in a WC-Co system by Mandel et al. [41], where it was found that the compressive strength increased with increasing strain rate, from 4370 MPa for WC-12Co under quasi-static loading to 6660 MPa for WC-6Co under dynamic loading (~ 1.5 times higher). Guden and Hall [42] also reported a difference in compressive failure stress with increasing strain rate (10^{-5} to $7 \times 10^2 \text{ s}^{-1}$) for an Al/Al₂O₃ cermet. Other studies on the rate-dependency of cermets have shown significant changes under dynamic loading in both mechanical properties and failure mechanisms [43 – 45].

However, little information is available on the rate-dependent behavior and fracture mechanisms of oxide cermets (in this thesis, the TiAl/Ti₃Al-Al₂O₃ cermet) even though they have gained recent engineering research interests towards defense and wear applications [10]. This is likely because the oxide forms of cermets, such as reinforced with Al₂O₃ and ZrO₂, are generally hard to manufacture as a result of their poor wettability with metals using conventional fabrication methods [46]. The poor wettability of oxide cermets leads to a reduction in toughening effects by the metallic phase [10], a counterproductive effect in cermet development. Based on the previous knowledge obtained from other cermet systems, it is safe to assume that rate-dependency on material properties and failure mechanisms could occur in the current material. This can be further proven by the established rate-sensitivity demonstrated in single TiAl alloys and alumina ceramics [47 – 50].

To date, literature published on the TiAl/Ti₃Al-Al₂O₃ cermet focused mainly on novel manufacturing processes and powder mixture formulations, with limited experimentation studies focusing on exploring the mechanical properties and fracture mechanisms [51, 52, 54 – 56]. For

example, Shen et al. [51] reported the quasi-static fracture toughness of the TiAl/Ti₃Al-Al₂O₃ cermet as a complementary part to discuss the quality of fabrication, while Lapin et al. [26] discussed the effect of the size and volume percentage of the alumina particles on the Vickers hardness and room temperature quasi-static compression properties of a directional solidified titanium aluminide alloy. In other works, attempts to model the reaction routes of the sintering processes [54] and microstructural investigations on adding secondary reinforcements (e.g., nano-precipitates) [55] or secondary processing (e.g., annealing) were presented. The lack of experimental studies on the TiAl/Ti₃Al-Al₂O₃ cermet and the gap between material science and experimental mechanics provide limited information on the material performance towards large-scale industrial applications. It is thus of essential importance to study the material more systematically for materials design and optimization, where material fabrication, characterization, and experimentation should be conducted simultaneously and coherently if the material is to be delivered for industrial integration. In this thesis, the TiAl/Ti₃Al-Al₂O₃ cermet is intended for ballistic protection applications, where high-velocity impact is prevalent. Thus, the limited information on high-rate properties and mechanisms of the material need to be addressed before utilizing the material for commercial use in, for example, body armors.

Chapter 3: Characterization and Mechanical Testing on Novel ($\gamma + \alpha_2$) - TiAl/Ti₃Al/Al₂O₃ Cermet¹

This chapter is adapted from the first paper published by the author in *Material Science and Engineering A* in March 2019. The texts, tables, and figures including their numbering and references are kept as they appeared in the published article. In this chapter, detail characterization has been carried out on the as-received TiAl/Ti₃Al-Al₂O₃ cermet to investigate the microstructural features. In addition, rate-dependent stress-time history curves and the corresponding surface deformation mechanisms are obtained from using quasi-static and dynamic compression tests. Several mechanical properties, such as the peak compressive strength, failure strain, and fracture toughness are compared with alumina AD995 (Cooresstek, Inc.), and insights have been given for the potential use of the cermet in protection applications.

¹ Information in this chapter has been published in: Li, H. Y., P. Motamedi, and J. D. Hogan. "Characterization and mechanical testing on novel ($\gamma + \alpha_2$)–TiAl/Ti₃Al/Al₂O₃ cermet." *Materials Science and Engineering: A* 750 (2019): 152-163.

Characterization and Mechanical Testing on Novel ($\gamma + \alpha_2$) - TiAl/Ti₃Al/Al₂O₃ Cermet

HY. Li^{a,*}, P. Motamedi^{a,b}, J.D. Hogan^a

^a *Department of Mechanical Engineering, The University of Alberta, Edmonton, AB T6G 2R3, Canada*

^b *Nanotechnology Research Centre, National Research Council Canada, 11421 Saskatchewan Dr., Edmonton, AB T6G 2R3, Canada*

Abstract

This study investigates the micro/nanostructural features and mechanical responses of a novel TiAl/Ti₃Al/Al₂O₃ cermet fabricated by self-propagation high-temperature synthesis. The microscopic diagnosis was used to examine the material composition, phase distribution, and elemental concentration of the cermet. Three phases were identified in the cermet, including γ -TiAl, α_2 -TiAl, and Al₂O₃. The material exhibited ultrafine microstructure with the size of alumina particles between 0.5 microns to 1.5 microns occupying $65 \pm 1\%$ areal fraction of the material. Transmission electron microscopy (TEM) was employed to examine the “coral” network of alumina particles with the titanium aluminide matrix, which was believed to be contributing to the failure of the material. Iron/nickel-based nano-precipitates were found through TEM as well, and these were believed to be contributing to the mechanical properties of the material. The rate-dependency on the compressive strength and failure mechanisms were studied by quasi-static and dynamic uniaxial compression, and it was found that the quasi-static and dynamic compressive strengths were 2400 ± 120 MPa and 3370 ± 450 MPa, respectively. The results are compared with those for alumina AD995, to highlight differences in mechanical properties, such as compressive

strength and failure strains. These findings serve as the preliminary dataset for material design, manufacturing, and modeling of advanced cermets.

Keywords: Cermets; microstructural characterization; uniaxial compression test; rate-dependency; compressive strength; failure mechanisms; material design and manufacturing

1. Introduction

Metal matrix composites (MMCs) are among the emerging materials for structural applications which have been extensively studied over the past century. Cemented carbide was the first major MMC invented in the 1920s. It was mainly used as cutting tools due to its superior hardness, when compared to conventional metals and ceramics. However, its high density (15.9 g/cm^3) limited its usage in applications, where high strength-to-weight ratio was required (e.g., body armor, turbine blades). In the 1930s, the term “cermet” was created to distinguish other ceramic-metallic composites, which consist mainly of carbides other than WC [3.1]. In 2001, Daniele Mari defined three classes of cermet by their refractory components [3.2]. The first class was called “hardmetal,” and this consisted of ceramics that were constituted of carbides, nitrides, borides, and silicides of the metals in the fourth to six groups of the periodic table. The second class was termed “cermet,” and this consists of some of the hardest carbides and nitrides like SiC and B₄C. Large differences in elastic modulus and thermal expansion from metals usually made these cermets of little practical interest. The third class was called “oxide cermet,” which consists of oxide ceramics like Al₂O₃ and ZrO₂. This class of materials’ high resistance to chemicals and the refractory character of these oxide ceramics has stimulated engineering research effort towards cermet development for dental [3.3] and high strain rate applications [3.4].

Interest in using cermets to replace advanced ceramics in body armor has existed since the 1970s (and likely before). This was motivated by the ability to add increased ductility to cermets, which

was believed to augment their impact performance through a reduction in the depth of penetration and delayed axial cracking [3.4]. The seminal work of Wilkins et al. [3.4] in 1969 and Landingham and Casey [3.5] in 1972 also demonstrated the importance of microstructure (e.g., size and distribution of ceramic phase in the metal) on the impact performance of cermets. This work served as the foundation for the subsequent studies, which increased in frequency in the 1990s when fabrication technologies were able to produce cermets at near 100% theoretical densities with comparable hardness and densities to conventional advanced ceramics (e.g., alumina at $\sim 4 \text{ g/cm}^3$). Examples include: $\text{Al}_2\text{O}_3\text{-Al}$ (3.53 to 3.74 g/cm^3) [3.6], $\text{TiB}_2\text{-B}_4\text{C}$ (3.25 g/cm^3 to 3.6 g/cm^3) [3.7], $\text{Cr-Cr}_2\text{S}_3$ (4 g/cm^3 to 5.4 g/cm^3) [3.8], and $\text{B}_4\text{C-Al}$ cermet (2.62 g/cm^3) [3.9]. The further integration of these materials in protection applications requires a better understanding of their rate-dependent behavior, which is addressed in this paper.

Previous studies on cermets have shown that mechanical properties and fracture mechanisms are rate-dependent, and this is important for their use in ballistic protection applications. For example, Rittel et al. [3.10] found that the dynamic fracture toughness of $\text{TiC}/1080$ steel cermet is significantly higher (by about a factor of 3) than its quasi-static counterpart. In another study, Kaplan [3.11] and his colleagues showed that this increase was likely due to the change in fracture mechanisms from quasi-static to dynamic condition by visualizing the change in the crack path with the help of transmission electron microscopy. Rate-dependent effects for the compressive strength were also studied in WC-Co system by Mandel et al. [3.12], where it was found that the compressive strength increased with increasing strain rate, from 4370 MPa for WC-12Co under quasi-static loading to 6660 MPa for WC-6Co under dynamic loading (~ 1.5 times higher). Guden and Hall [3.13] also reported a difference in compressive failure stress with increasing strain rate (10^{-5} to $7 \times 10^2 \text{ s}^{-1}$) for an $\text{Al}/\text{Al}_2\text{O}_3$ cermet. Other studies on the rate-dependency of cermets have

been showing significant changes under dynamic loading in both property and mechanisms [3.14 – 3.16]. Understanding the complex rate-dependent response of cermets is essential to further improving their usage in dynamic applications (e.g., body armor). We study these aspects in this paper for a novel $(\gamma + \alpha_2)$ - TiAl/Ti₃Al/Al₂O₃ cermet.

The $(\gamma + \alpha_2)$ - TiAl/Ti₃Al/Al₂O₃ cermet belongs to the “oxide cermet” class. This cermet is relatively new in the open literature (e.g., Shen et al. [3.17]), with limited information on its mechanical responses. Xiang et al. [3.18], Zhang et al. [3.19], and Huy et al. [3.20] only reported the quasi-static hardness and fracture toughness values of the as-fabricated cermets, with no rate-dependent information available in their studies. Instead, most of the available literature has focused on sintering and forging techniques, such as the Self-Propagation High-Temperature Sintering process (SHS) [3.20 – 3.22]. In these studies, some mechanical properties, such as density and toughness, have been calculated by chemistry means (e.g., density of state method (DOS), band structure, and chemical bonding) [3.17]. To address the gap in knowledge on the mechanical response of this material, this paper explores the mechanical behavior of the TiAl/Ti₃Al/Al₂O₃ cermet under both quasi-static and dynamic loading. Prior to the experiments, surface microscopy was first used to examine the microstructure and composition of the as-received material. This included scanning electron microscopy (SEM), transmission electron microscopy (TEM), x-ray diffraction (XRD), and energy-dispersive x-ray spectroscopy (EDS). Secondly, mechanical testing was carried out on a standard MTS machine at quasi-static strain rates and split Hopkinson pressure bar (SHPB) for dynamic strain rates. Mechanical properties and material performance under different loading conditions were compared with alumina AD995, which is an advanced ceramic that is being used in many defense applications. The results gathered

in this study can facilitate the understanding of the microstructure-property relationship, which is crucial in the design of next-generation protection materials.

2. Material

The as-received material is manufactured by Lumiant Corporation, British Columbia. The TiAl/Ti₃Al/Al₂O₃ cermet, commercially known as TitanMade L465, is fabricated through Self-Propagation High-Temperature Sintering. The powders used for sintering are titanium dioxide and aluminum. The primary and secondary reactions were well documented in Shen et al. [3.17] and Gaus et al. [3.23]. Once synthesized, the material is received as plates, and these plates are cut into cuboidal specimens with sizes of 2.3 mm x 2.5 mm x 2.7 mm by electrical discharge machining (EDM) for mechanical testing. Table 3.1 summarizes the mechanical properties of the material provided by the company. Comparable data for alumina AD995 (by Coorstek. Inc.) [3.24] is also shown in Table 3.1, and this is drawn upon later in the discussion when comparing the two materials. Note that all properties reported are measured by standard techniques under quasi-static condition. Shown in Table 3.1, the cermet has comparable density with alumina AD995 with an increase in flexural strength and fracture toughness, but with lower stiffness and hardness. This can serve as a preliminary observation on the effect of combining ceramic and metallic materials (in this case, intermetallic to be more specific). To explore the hardness and stiffness properties of the individual titanium aluminide and alumina phases, nanoindentation testing was performed by Anton Paar [3.25] on the Ultra Nanoindentation for 900 indents on an area of 270 μm x 270 μm using a peak load of 1 mN. The elastic moduli for titanium aluminide and alumina phases were found to be 178 ± 31 GPa and 278 ± 41 GPa, respectively. The hardnesses for the two phases were 8 ± 2 GPa for the titanium aluminide phase and 22 ± 8 GPa for the alumina phase. Nanoindentation

testing with the same setup was performed on alumina AD995 as well, which gave a hardness of 23 ± 11 GPa. These values are also shown in Table 3.1 as nano-hardness.

Table 3.1: As-received mechanical properties with comparison to 99.5% purity Alumina by Coorstek, Inc.

	TitanMade L465	Al ₂ O ₃ (AD995)
Density (g/cm ³)	3.9	3.9
Stiffness (GPa)	280	370
Hardness (GPa)	11	14.1
Flexural Strength (MPa)	925	375
Fracture Toughness (MPa m ^{1/2})	7.4	4 – 5
Nano-Hardness (GPa)	8 ± 2 (titanium aluminide)	23 ± 11
	22 ± 8 (alumina)	

3. Experimental Setup

3.1. Scanning electron microscopy and energy-dispersive x-ray spectroscopy

Scanning electron micrographs were taken of the polished surface (sub-micron) of the material by using a Zeiss Sigma FESEM machine equipped with an energy-dispersive x-ray spectroscopy setup. The machine is equipped with a field emission electron gun. No coating was needed for the specimen since conductivity was an inherent property of the intermetallic phase in the composite. The electron high tension (EHT)/accelerating voltage was set at 20.00 kV, and the working distance (WD) was at 8.5 mm. An In-Lens detector (ILD) coupled with a back-scattered detector (BSD) was used in this study to reveal the phase distribution within the material. EDX data was examined using the AZtec software from Oxford Instruments.

3.2. Transmission electron microscopy

Transmission electron microscopy was conducted using a JEOL JEM-ARM200CF S/TEM tool. The tool was operated at 200 kV, and the data was analyzed using the Gatan Digital Micrograph software. An energy-dispersive x-ray spectroscopy detector was coupled with TEM to examine

the nanoscale composition of the cermet. Specimens for this investigation were cut to a cross section of 2.5 mm x 2.5 mm using a diamond wafer blade and mechanically grounded from the bulk specimens down to $\sim 50 \mu\text{m}$ in thickness with a 15 μm grid diamond paste. This was followed by mechanical dimpling to 30 μm , and ion milling (Ionfab 300 IBE) with a 4-inch diameter ion gun (8kV for 1 hr, 5kV for 45 mins, and 3kV for 40 mins) in an argon environment on a single wafer system to perforation.

3.3. X-ray diffraction

X-ray diffraction (XRD) analysis was carried out to assess the crystallinity and identify the phases. The tests were carried out on a Bruker D8-Discover machine using Cu $K\alpha$ beam source. The apparatus was operated at 50 kV and 1000 μA . A Vantec 500 detector was used to produce two-dimensional frames, which were then processed using the Bruker Eva software to produce θ -2 θ -equivalent spectra.

3.4. Quasi-static uniaxial compression

The quasi-static uniaxial compression tests were carried out on a standard MTS series 810 servo-hydraulic machine. Shown in Figure 3.1 is the schematic of the quasi-static test setup. The loading platens were made from M2-graded high-speed steel (HSS) with diameter of 1 inch, and these were used to compress the specimen. Ti-6Al-4V titanium alloy jacketed tungsten carbide (WC) platens were used between the specimen and the loading platens to provide stress re-distribution from the specimen to the loading platens, as well as to reduce indentation from the harder material to the loading platens. This follows the ASTM C1424-15 standard [3.26]. As required, extreme pressure grease was applied on the WC platen surfaces as lubricant to eliminate the frictional effect. The platens were pre-loaded without specimen to create a thin, uniform layer of lubricant. The specimens were then carefully placed at the middle of the platens. Proper alignment was ensured

by carefully bringing the platens and specimen in touch. The experiment was performed under a displacement control setting with a nominal strain rate of $1 \times 10^{-4} \text{ s}^{-1}$. The cross-head displacement was measured by a linear variable differential transformer (LVDT) displacement sensor with an accuracy of 0.001 mm. A 100 kN load cell with a background noise of approximately $\pm 1 \text{ N}$ was used to record the force history during the loading process. The acquisition rate of the MTS machine was set at 30 Hz. Coupled with the testing setup was a high-speed AOS PROMON U750 camera to provide visualization of macroscopic deformation features on the specimen surface. The specimen was positioned normal to the optical axis of the camera to eliminate out-of-plane displacement. This camera has a full resolution of 1280 x 1024 pixels and recorded at a frame rate of 100 frames per second. The experiment was stopped when catastrophic failure happened. The engineering stress was calculated by dividing the applied load by original specimen surface area. In total, ten experiments were presented in this study at the same loading condition to ensure repeatability.

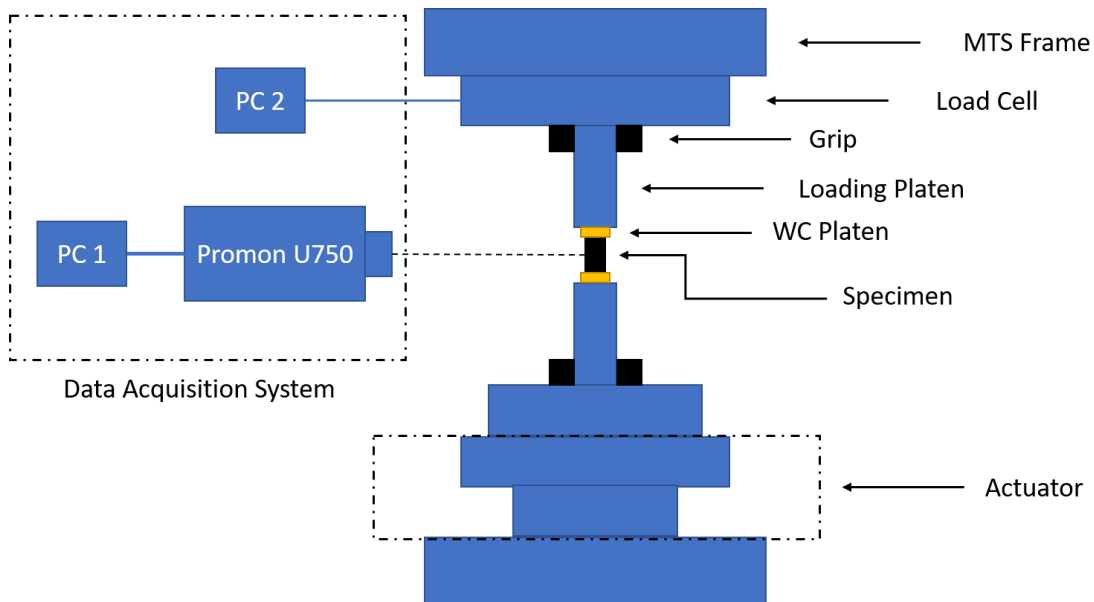


Figure 3.1: Schematic of the MTS machine experimental setup.

3.5. Dynamic uniaxial compression

The dynamic uniaxial compression tests were conducted on a modified version of a split Hopkinson pressure bar (SHPB). In a dynamic uniaxial compression test with conventional SHPB setup, the striker is launched from a pressurized gas gun and strikes the incident bar. An elastic stress wave is generated and travels through the incident bar towards the front end of the specimen. Due to the mismatch of impedance between the steel and the cermet, a reflected wave and a transmitted wave will be generated at the front and end faces of the specimen, respectively. The reflected wave travels back to the incident bar, and the transmitted wave travels through the transmitted bar. By capturing the pulse information with strain gauges, the stress, strain and strain rate can then be calculated.

In this paper, like some others for ceramics [3.27] [3.28], we plot the stress vs. time to understand the failure processes during loading. The nominal axial stress in the specimen is determined as,

$$\sigma(t) = E_0 \frac{A_0}{A_s} \varepsilon_t(t) \quad (1)$$

where A_s (m^2) is the cross-sectional area of the specimen, A_0 (m^2) is the cross-sectional area of the bar, and ε_t is the time-resolved transmitted strain. Note that the equation above assumes that the specimen is deformed homogeneously, and the bar deforms elastically during loading.

A modified version of the conventional setup needs to be adapted for testing brittle materials [3.29]. Shown in Figure 3.2 is the schematic of a modified version of the SHPB setup used in this study. The setup consisted of a gas gun, a striker, an incident bar, a transmitted bar, and an acquisition system. The acquisition system included amplifiers and a digital oscilloscope. The striker, incident bar, and transmitted bar were made from Maraging steel C-350. The stiffness of the material was 200 GPa with a yield strength of 2.36 GPa. The high stiffness and strength of the bars were required for testing stiff materials, such as ceramics and cermets. Similar materials have been used for

ceramics and cermets testing [3.14] [3.29]. The dimensions of the bars used in this study were 1016 mm and 914 mm in length for the incident and transmitted bar, respectively, with a common diameter of 12.7 mm. In this study, both the incident and reflected waves were captured by a strain gauge mounted on the incident bar, which has a distance of 662 mm to the front face of the specimen. The transmitted wave was captured by the strain gauge mounted on the transmitted bar, which has a distance of 310 mm to the end face of the specimen. The length of the bars and the position of strain gauges were chosen to avoid signal overlapping. Both strain gauges were $350\Omega \pm 0.3\%$ with a gage factor of $2.130 \pm 0.5\%$ (made from Micro 184 Measurements CEA-13-250UN-350). Two independent conditional amplifiers (Vishay InterTechnology 2310B) were used for both gauges. The gains were set at 10 times on both amplifiers. A Tektronix DPO2024B oscilloscope was used to capture the signal. The resolution of the oscilloscope was 12-bit recording at 500 MHz. A short striker (125 mm) was used based on the observation on the pulse duration in the trial tests.

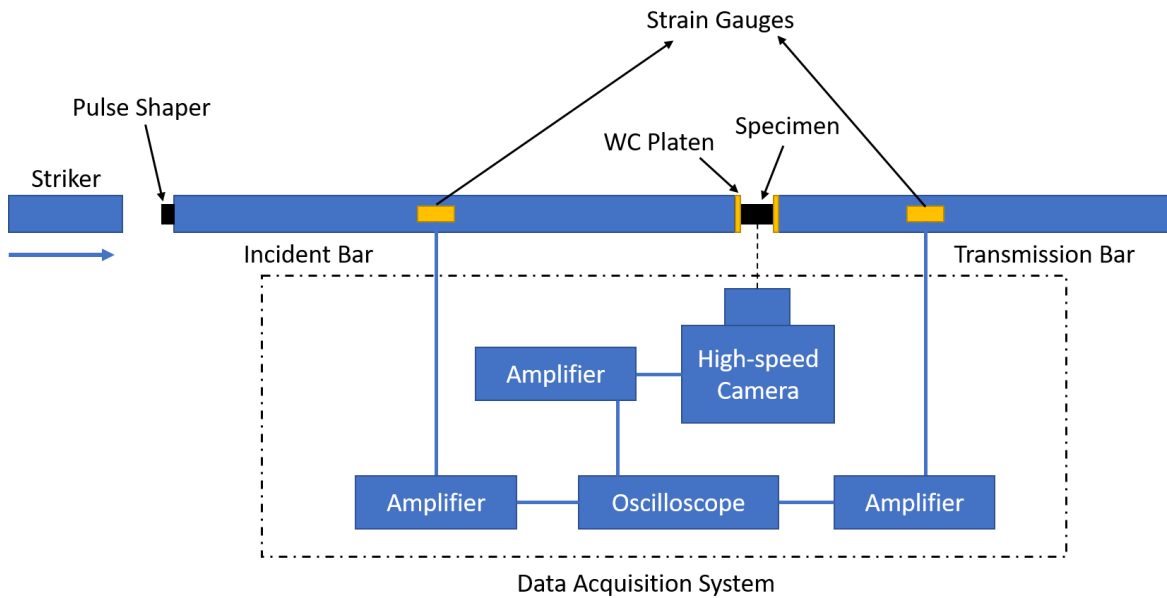


Figure 3.2: Schematic of the modified Split Hopkinson Pressure Bar (SHPB) experimental setup.

Two impedance matched Ti-6Al-4V titanium alloy jacketed tungsten carbide (WC) platens with the same diameter of the bars were attached to the end of the incident and transmitted bar for redistribution of loads. This has been reported by Chen and Ravichandran [3.29] for preventing indentation and reducing stress concentration on the specimen. The specimen was placed between the two platens. The end faces of the specimen were lubricated with extreme pressure grease to reduce the frictional effect and allow the specimen to expand freely in the radial direction during loading. This setup is well documented in the literature [3.30] [3.31].

A pulse shaper was placed at the impact end of the incident bar to create a favorable profile of the pulse for the specific material. Trial tests were performed by assuming a brittle nature of the cermet based on the knowledge of the phases present. Pulse shapers with different materials and thickness were tested, and elastic tests were conducted with these pulse shapers beforehand to determine an appropriate rise time and ramp time, as well as ensuring force balance and constant strain. In these experiments, a mild steel pulse shaper was selected, and this is consistent with the literature [3.57 – 3.59]. The mild steel pulse shaper used in this study had a thickness of 0.0635 mm, and this was selected to give the most reasonable rise time and ramp time, for which the natural responses of the material could be well captured.

An ultra-high-speed Shimadzu HPV-X2 camera was used to capture the failure process of the specimen during SPHB testing. Exposure times of 200 ns were obtained using ultra-bright LED light attached with fiber optical light guide with an outer diameter of 7.6 mm so that the light can be concentrated onto the specimen surface. The camera was triggered by a split signal from the incident strain gauge. A separate conditional amplifier was coupled with the oscilloscope for camera triggering. In all experiments, the camera operated at 2 million frames per second with a resolution of 400 x 250 pixels. At this rate, the camera was able to capture 128 frames in total. The

output pulse of the camera was used to correlate the times between images and strain gauge measurements. Five tests were performed under the same loading conditions to verify the repeatability of experiments.

4. Experimental Results

4.1. Material Microstructure and phase distribution

Shown in Figure 3.3 is a BSE-SEM image (Fig. 3.3-a) with EDS concentration mapping on the elements: Al (Fig. 3.3-b), O (Fig. 3.3-c), Ti (Fig. 3.3-d). Overall, this figure is used to present a representative phase distribution within the material. In the BSE-SEM image, the lighter regions correspond to the TiAl phase because of the higher atomic number value. Consequently, the darker regions corresponded to the Al₂O₃ (alumina) phase. The darkest spots in Fig. 3.3-a correspond to the micropores present in the material, which tend to cluster around or within the alumina phase. This has been confirmed with FESEM images taken at the same location. It is observed that most of the alumina particles cluster to form a network with very few individual particles distributed sparsely over the matrix. A “coral” network of alumina phase is proposed to describe this microstructural feature, and this is believed to be the result of the rapid sintering process. Similar “coral” network has been observed in TiAl/Ti₃Al/Al₂O₃ cermet by Huy et al. [3.20] using Combustion Sintering. Next, image processing in MATLAB is used to examine the areal percentage of each phase and porosity level. To do this, the BSE-SEM image is first converted to a binary image. Each pixel is discretized and assigned a number from 0 to 255 as a Unit8 type image. In this case, pure white corresponds to 255, and pure black is 0. Thresholds based on gray level are then manually selected to isolate the titanium aluminide and alumina phases, as well as the pores. As the outcome of the analysis, the porosity level is found to be between 1.2 % and 3% at 2000 times magnification, with the uncertainty associated with the range of threshold values

chosen. The area fraction of the alumina phase is estimated at $65 \pm 1\%$, using similar methodology. The 1% uncertainty is associated with a $\pm 20\%$ grayscale threshold determined manually to compensate for any human errors. By using the same procedure, the pore size is found to be between 0.03 and 1 μm with an average of $0.15 \pm 0.21 \mu\text{m}$. This range of pores includes the structural and sub-structural pores in the material. The size of individual alumina particles is between 0.5 and 1.5 μm with an average of $1.0 \pm 0.3 \mu\text{m}$. The size of the alumina clusters is between 3 and 9 μm . All information above has been confirmed with other BSE-SEM images taken at different locations with different magnifications. Five specimens are also used to ensure the microstructural variability is taken into account.

Next, we consider the concentrations of the elements in Fig. 3.3-b to d. A color bar is presented as a reference to concentration for visualization. In the images, a brighter color indicates higher concentration while a darker color indicates a lower concentration. In Fig. 3.3-b, it is confirmed that Al is present everywhere in the material, but it is highly concentrated in the alumina phase (darker phase in BSE-SEM image in Fig. 3.3-a). Comparing Al (Fig. 3.3-b) with Ti (Fig. 3.3-c), it is observed that regions of high concentrations of Al correspond to regions with low or little concentration of Ti. The dark regions in Fig. 3.3-c confirm that there is little to no Ti in the alumina phase. Similarly, regions with higher concentration of Al overlap with regions with higher concentrations of O, which are the alumina phase. However, it is clear that some O exists in the TiAl phase regions, which indicates a high possibility that a secondary phase is present in the material. For this cermet, this phase is a $\alpha_2\text{-Ti}_3\text{Al}$ or $(\gamma + \alpha_2)$ lamellar structure since it is easier for oxygen to precipitate in these two phases during the sintering process [3.17] (confirmed next in XRD scanning).

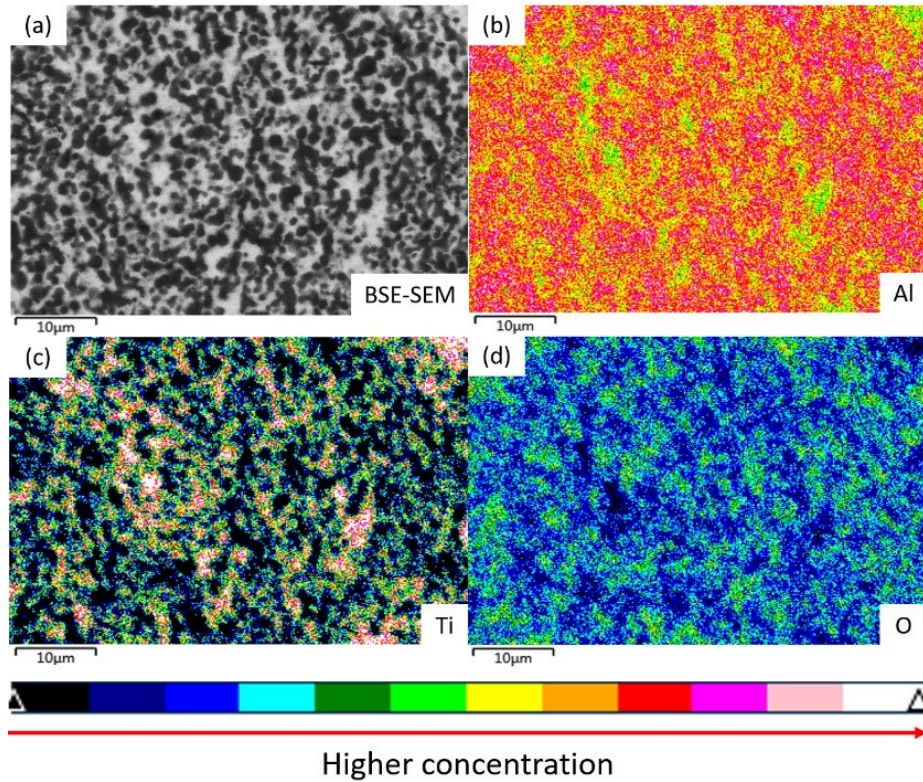


Figure 3.3: EDS concentration mapping with BSE-SEM image showing the distributions of selected elements. The concentration of the elements is ordered based on the color sequence in the visible light spectrum with a color bar shown below the maps. (a) FESEM image showing the phase distribution, where the black regions correspond to the alumina phase and the white regions correspond to the titanium aluminide phase; (b) Distribution and concentration of Al in the FESEM image; (c) Distribution and concentration of O in the FESEM image; (d) Distribution and concentration of Ti in the FESEM image.

To summarize the elemental analysis results, we show the weight and atomic percentage of the primary and secondary elements in Table 3.2. This is extracted from the EDS mapping presented above (see Fig. 3.3). Oxygen is the dominant element in both weight and atomic percentage, with 35.4% and 50.5%, respectively. This is followed by aluminum and titanium, which is expected since the alumina phase occupies 2/3 of the material in terms of volume. Carbon, zirconium, and potassium appeared in relatively low percentage in the material, with 4.5%, 0.9%, and 0.2% in weight percentage, respectively. It is believed that the trace of carbon is from the carbon adhesive

for attaching the specimen. The source of zirconium and potassium is likely impurities in the original mixing powders.

Table 3.2: The weight and the atomic percentage of the primary and secondary elements present in the EDS scan. Here carbon, zirconium, and potassium are considered as the secondary elements in the material.

Element	wt%	at%
O	35.4	50.5
Al	34.0	28.8
Ti	25.0	11.9
C	4.5	8.5
Zr	0.9	0.2
K	0.2	0.1

4.2. Material composition

Shown in Figure 3.4 is the diffraction spectrum from the x-ray diffraction analysis. The results presented here indicate that three phases are present in the specimen: 1. γ -TiAl, 2. alumina (Al_2O_3), and 3. α_2 -Ti₃Al. The α_2 -Ti₃Al phase is considered to be a by-product of the SHS process, during which the α_2 -phase is introduced into the material through chemical reactions. This has been documented in the literature for this type of cermet [3.17] [3.20]. A minor trace of oxygen is detected in the α_2 phase, where the element exists in the EDX mapping of the TiAl phase (Fig. 3.3-d) as well. It has been reported that the (γ + α_2) lamellar structure formed from the co-existence of individual γ - and α_2 -phases could have a positive effect on the material toughness and ductility, given higher oxygen solubility and oxide precipitation at the interface [3.17], although this is not the focus of the current study.

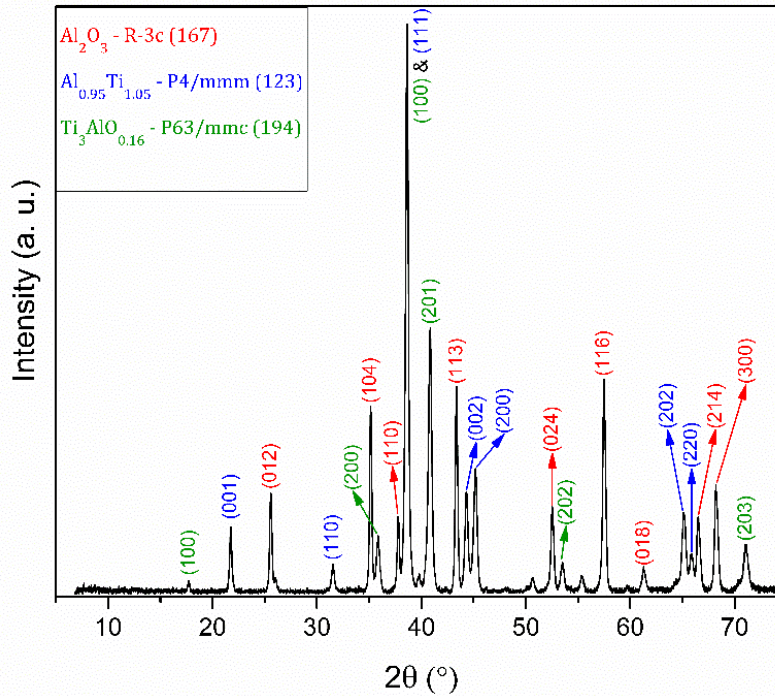


Figure 3.4: XRD spectrum of the cermet showing three distinct phases presented in the material. The legend shows the phases associated with each color, along with their corresponding space groups.

4.3. Nanoscale microstructural features

Shown in Figure 3.5 is a collection of transmission electron micrographs of the cermet. TEM was used to examine the detailed features of the phases and grains. At the sub-micron scale, individual alumina grains can be observed in Fig. 3.5-a (darker regions) and alumina particles packed with closely bounded interfaces are identified as the "coral" clusters in the material. This can be verified by the EDS mapping of Ti shown in Fig. 3.5-b. From the EDS map, the alumina particles are interconnected and non-uniformly distributed in the microstructure. Shown in Figure 3.5-c is the grain boundary of two titanium aluminide grains. Multiple locations are scanned, and minimal signs of plastic deformation, such as dislocations and twinning, is observed on these grains. Grain boundaries appear to be free of additives, and no microcracks are observed on the grains or along

the interface. Nano-precipitates (black dots) are observed throughout the material (including titanium aluminide and alumina phases) at higher magnification, and this feature is not resolvable by SEM or EDX on the bulk specimen.

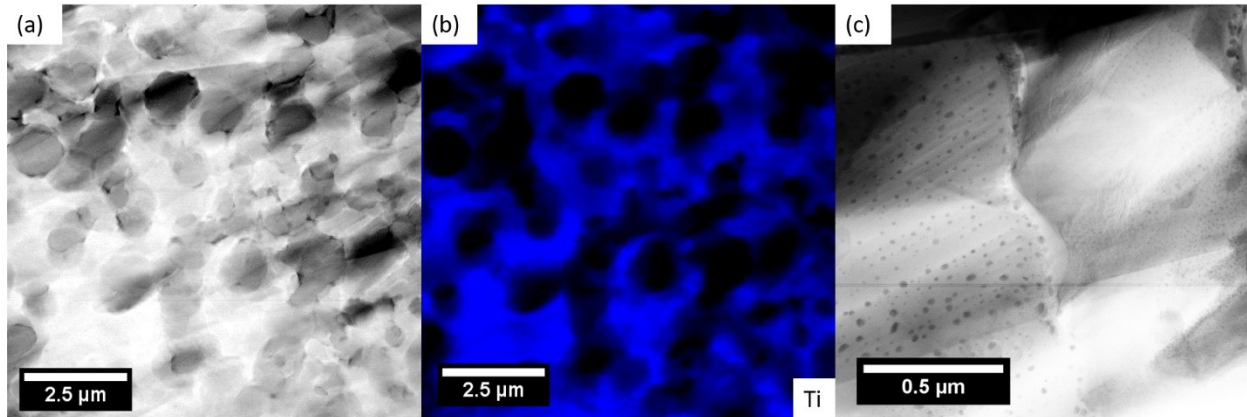


Figure 3.5: Transmission electron micrographs showing: (a) Individual alumina particles (darker) and the “coral” network formed by connected alumina particles under bright field mode, (b) corresponding EDS map of titanium further proves the composition of particles and highlights the alumina network, and (c) the grain boundary between two titanium aluminide grains.

Next, EDS is performed on the TEM images to determine the compositions and distributions of these nano-precipitates. Shown in Figure 3.6-a is the TEM micrograph taken of a single titanium aluminide grain. The nano-precipitates are dispersed over the entire grain, with sizes between 10 and 40 nm and an average of 17 ± 6 nm. To further investigate the composition of the nano-precipitates, EDS mapping was performed at the same location, and the results are shown in Figure 3.6-b and c. From the images, iron and nickel elements are present in these nano-precipitates. The bright dots in Figure 3.6-a correspond to high concentrations of iron and nickel in Figure 3.6-b and c. Multiple locations are examined to confirm the universality of this observation. As an outcome, these nano-precipitates disperse uniformly throughout the entire material, including in the alumina phase. It is suspected that these nano-precipitates are in the form of a metallic or oxide phase of the two elements under high temperature and high pressure sintering conditions. According to the phase diagram of the Al-Ni-Ti system [3.32] and Al-Fe-Ti system [3.33], the nano-precipitates are

likely to appear in a metallic form in the titanium aluminide phase. By consulting the phase diagram of the NiO-Al₂O₃ system [3.34] and Al₂O₃-Fe₂O₃-FeO system [3.35], the nano-precipitates are likely to appear as their oxide form in the alumina phase. It is believed that their existence stems from the impurities in the original aluminum powder used for sintering or from the equipment used to transport the powders.

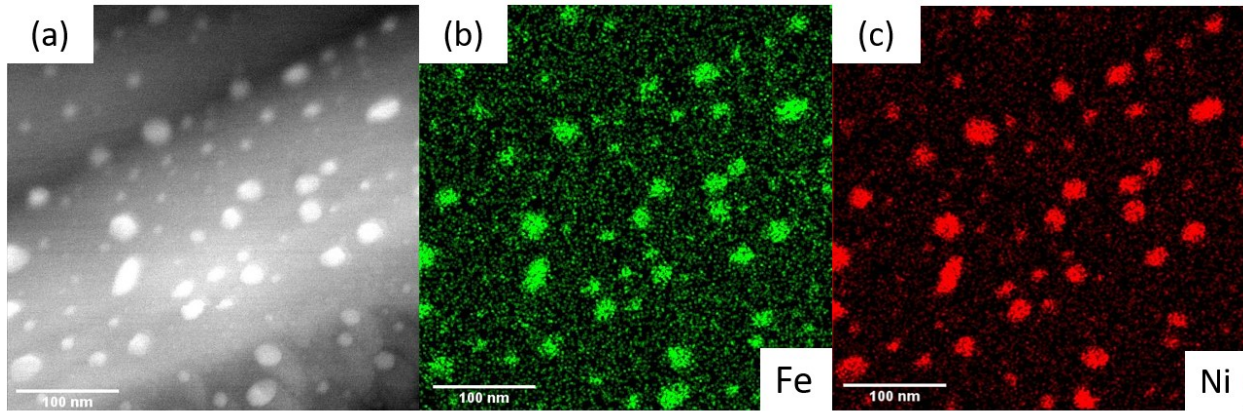


Figure 3.6: EDX mapping of a TEM micrograph on the TiAl grain showing compositions and distributions of the nano-precipitates on the grain. (a) TEM micrograph of a TiAl grain showing white “dots” distributed throughout, (b) Distribution of the iron element on the grain where “green” indicates the presence of iron, and (c) Distribution of nickel element on the grain where “red” indicates the presence of nickel.

4.4. Quasi-static uniaxial compression

Shown in Figure 3.7 is a typical stress-time plot of the cermet obtained from the MTS test. The material is loaded uniaxially in the vertical direction. In total, ten experiments are performed to verify repeatability. The nominal strain rate is approximately 10^{-4} s^{-1} in all experiments. This is obtained from calculating the strain by tracking the edge displacements of the specimen among a sequence of images and then dividing by the corresponding time. A brittle-like stress history with constant slope is observed in all experiments (see stress-time in Figure 3.7 on left). The peak stress in this case, which is often referred as the “quasi-static compressive strength”, is measured at 2563

MPa. Over all ten quasi-static experiments, the strength of the TiAl/Ti₃Al/Al₂O₃ cermet is measured at 2403 ± 120 MPa.

Next, we examine time-resolved images of the failure process during quasi-static compression on the right of Figure 3.7. A total of 6 images are shown with times corresponding to those labeled in the stress-history on the left. In the images, no surface cracks are observed during loading (frames 1 to 5), and the material remains intact under the compressive load. At image 5, the failure strain is measured between 1.1% to 1.7%, with an average of $1.4 \pm 0.2\%$ among all ten experiments. This is calculated by tracking the edge displacements for the first and last image. The drawback from the edge tracking technique is that it introduces errors based on the image resolution. In this case, the accuracy of the measurement in each test could be deviated up to $\sim 0.08\%$ (based on a resolution of 1280×1024 and taking half of a pixel width from each side of the edges). Frame six demonstrates a typical failure path of the specimen, taken just after the peak load. At time #6, the material fails catastrophically, and large structural fragments are observed in the corresponding image. An angled major crack passes through the entire specimen, which is believed to be intergranular fracture along the “coral” alumina network. From all quasi-static experiments, the angles of the fractures are 54 ± 3 degrees (measured from the top edge), and these typically form from 4 to 8 larger recoverable fragments.

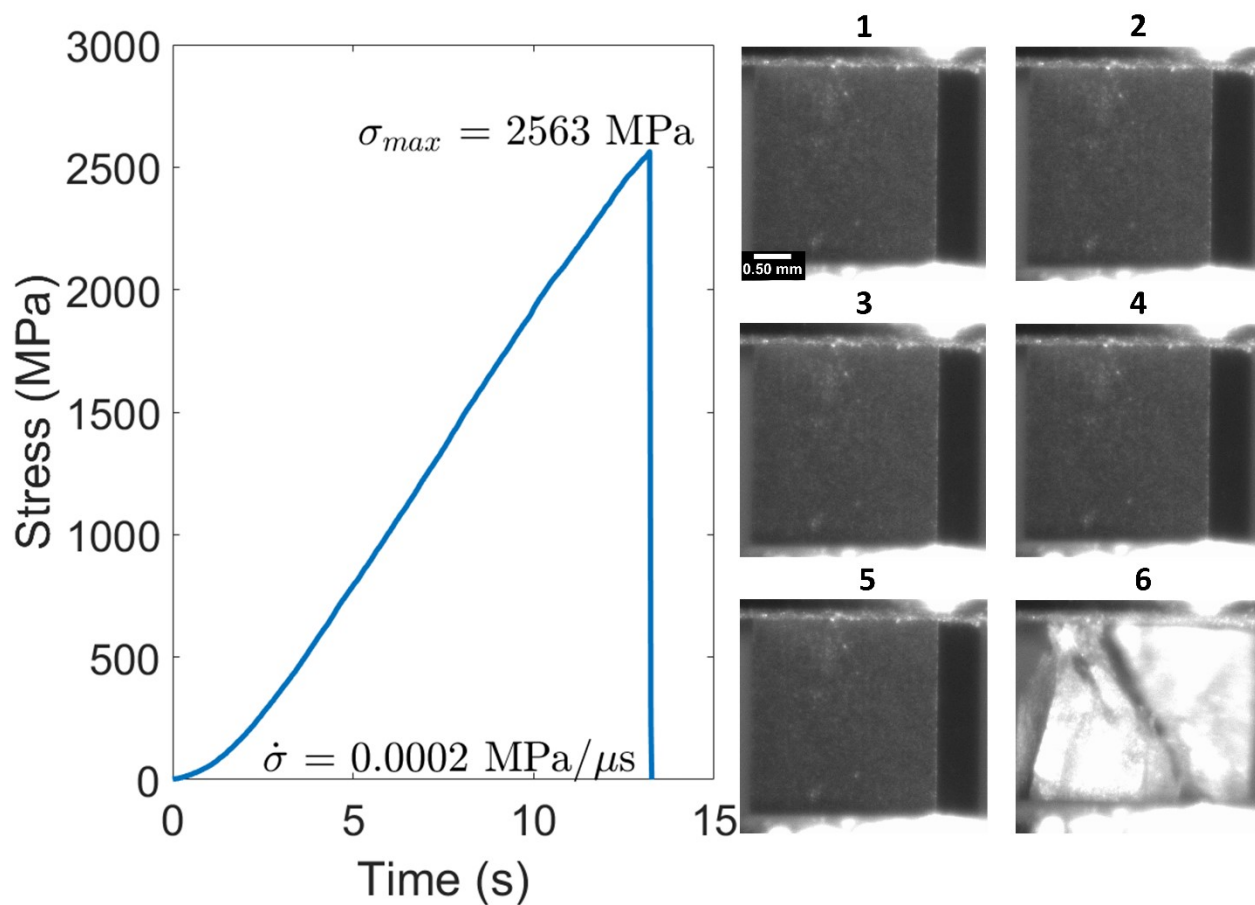


Figure 3.7: Stress history in quasi-static uniaxial compression with corresponding images at six different times showing the failure process of the material.

4.5. Dynamic uniaxial compression

Shown in Figure 3.8 is a typical stress history plot of the cermet from the dynamic test. The material is dynamically loaded in the horizontal direction. In Figure 3.8, the images on the right are re-oriented so that loading is in the vertical directions and the bar is impacting from the bottom towards the top for better visual comparison with the quasi-static case. In total, five experiments are performed to verify the repeatability. For dynamic loading, a different stress history profile is observed than under the quasi-static loading condition. The stress rate, in this case, is 208 MPa/ μ s, and this is estimated by taking the slope of the linear portion before the stress reaches its first peak. Consequently, the strain rate could be estimated by taking the stress rate and dividing by the intact

elastic modulus of the material. In this case, the strain rate is around 740 s^{-1} . This method of estimation had been used in literature for brittle materials [3.36]. In all five experiments, the strain rates are in the range of 700 s^{-1} to 1600 s^{-1} . The variability in the strain rate comes from the differences in the projectile speed under the same pressure, as well as the response of the material to the loading. It is observed that the signal peaks appear to ramp up, where the final peak indicates the highest stress reached. The “dynamic compressive strength” is taken as the highest peak stress value, and this is 2903 MPa. Across all experiments, the peak strength was measured as $3370 \pm 450 \text{ MPa}$.

Next, we explore time-resolved images depicting dynamic failure in Figure 3.8. Again, there are six images shown with times corresponding to those labeled in the stress-history on the left. In frame 1, no cracking is observed on the surface. Frame 2 corresponds to the first peak on the curve, where texturing (indicated by cycles in dash line in the current and subsequent frames) is observed on the surface from frame 2 to frame 4. No specific orientation of the texture can be determined. As a consequence of the texturing, relaxation allows the stress to drop from frame 2 to 3. In frame 3, a primary crack (red arrow) is observed at the bottom right corner, this is followed by further texturing with increasing sizes (and hardening in the stress-time curve) from frame 3 to 4. While the stress rises from point 3 to 4, in frame 4, the primary crack propagates axially when the stress raises again to around 2.7 GPa. In frame 5, a secondary crack (blue arrow) branches out from the primary crack, and a second crack (blue arrow) starts to form at the top left corner. In frame 6, more secondary cracks (blue arrow) are formed and branch out, and this results in catastrophic failure. The primary cracks propagate in such a way that they tend to cross the specimen with an angle between 50 and 60 degrees (measured from top edge of the specimen), which coincides with the crack growing direction in the quasi-static case (see Fig. 3.7 frame 6). The failure strain under

dynamic loading is determined from the frames right before the first crack is observed, and it is measured to be between 3% and 3.3%, with an average of $3.1 \pm 0.1\%$ in all five experiments. This is approximately twice as much as the values reported in the quasi-static case. Similar to the quasi-static experiments, the error from the edge tracking method in each measurement could deviate up to $\sim 0.25\%$ (based on a resolution of 400×250 pixels and taking half of a pixel at each side). Improvements need to be made in the future to accurately measure the strains using, for instance, the digital image correlation (DIC) method in order to increase the accuracy of such measurements. Crack speeds in all five experiments are between 700 m/s and 1200 m/s by measuring the first three primary and secondary cracks observed in each video. The average crack speed is 960 ± 210 m/s. These are estimated by first determining the location of the crack tip in the first frame and then measuring the displacement of the crack tip in subsequent frames. The crack speed of a specific crack is averaged over multiple frames to improve accuracy.

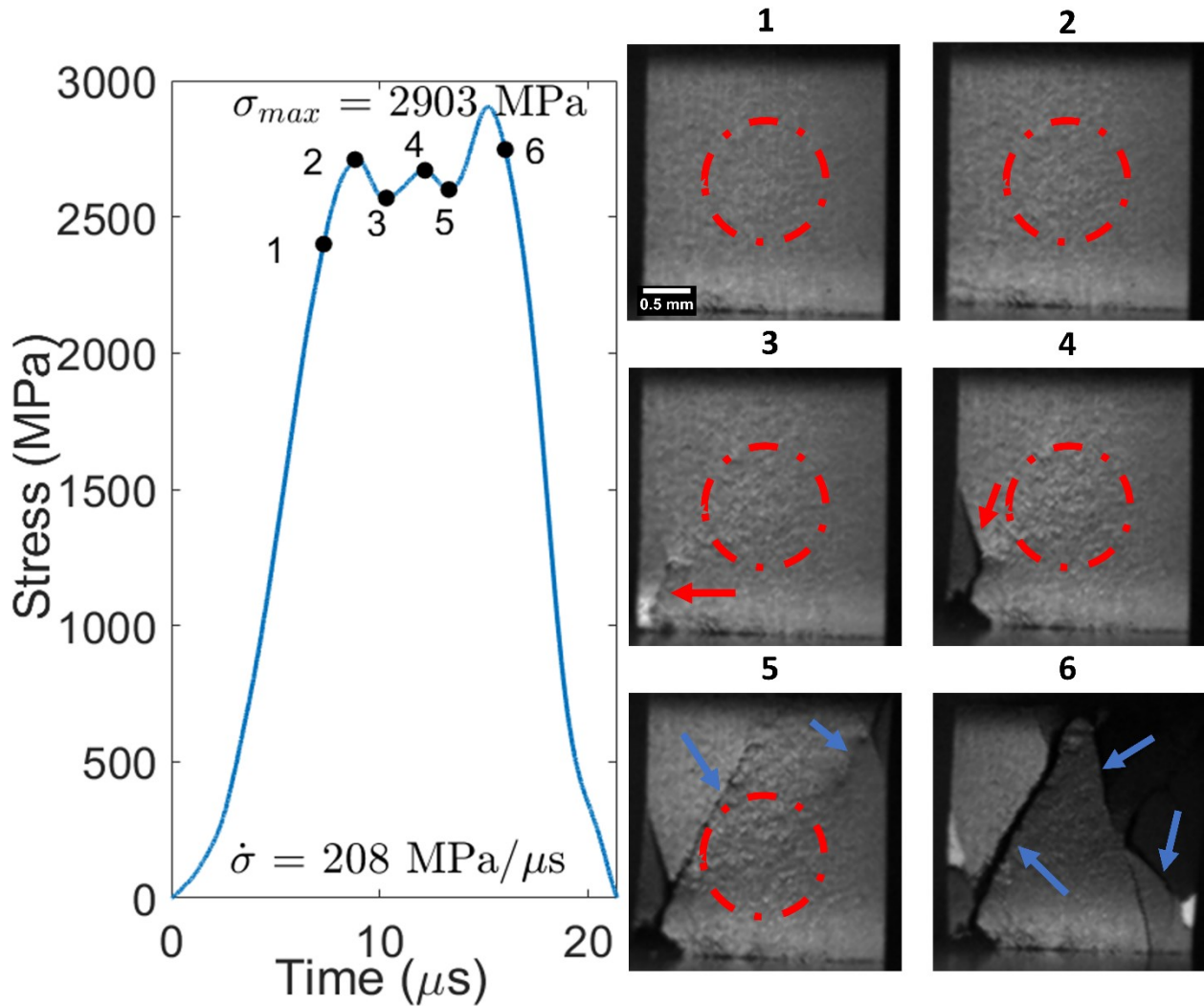


Figure 3.8: Stress history in dynamic (SHPB) uniaxial compression with corresponding images at six different times. The red arrow shows the formation of the primary crack, the blue arrows shows the formation of the secondary cracks, and the dashed circle indicates the formation of the texturing.

4.6. Summary of the rate-dependent compressive strengths

Shown in Figure 3.9 is a summary of the compressive strength against strain rate for the TiAl/Ti₃Al/Al₂O₃ cermet. All experiments, including ten quasi-static and five dynamic tests, are plotted against the log scale of the strain rate. For the quasi-static experiments, the rates are approximately 10^{-4} s^{-1} . For the dynamic experiments, the strain rates are 700 s^{-1} to 1600 s^{-1} . It is observed that the dynamic compressive strengths are higher than those in the quasi-static cases.

The quasi-static compressive strength has an average of 2400 ± 120 MPa, and the dynamic compressive strength has an average of 3370 ± 450 MPa. On average, this results in a 1.5 times increase in strength between the strain rate of 10^{-4} s^{-1} to $\sim 10^3 \text{ s}^{-1}$. It is also observed that the strain rate dependency has a more profound effect on the compressive strength in the dynamic regime ($> 10^2 \text{ s}^{-1}$).

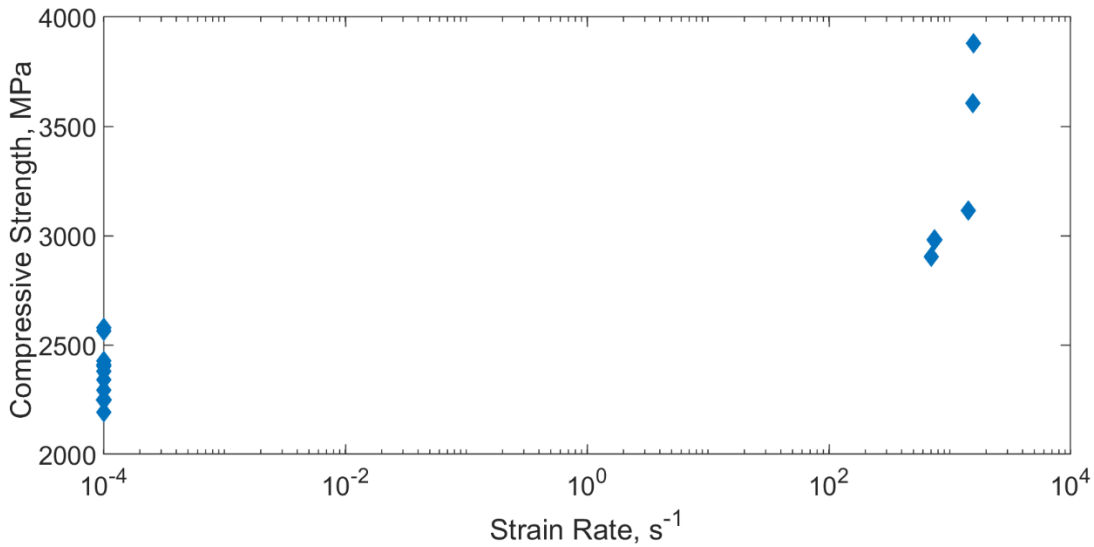


Figure 3.9: Semi-log plot of the compressive strength of the cermet with respect to the strain rates under uniaxial loading.

5. Discussion

This paper presents results on the characterization and mechanical testing of a SHS manufactured TiAl/Ti₃Al/Al₂O₃ cermet. Material composition, phase distribution, microstructure, and nanostructure were characterized using various microscopic diagnoses. The rate dependency on the compressive strength and failure mechanism were explored using quasi-static and dynamic uniaxial compression experiments. In the first part of the discussion section, each part of the characterization works will be bridged with previous studies on similar materials to understand the cermet microstructure further and apply this knowledge to material design. In the second part of

the discussion section, the mechanical and failure properties of the cermet will be contrasted with alumina AD995, and implications will be discussed.

5.1. Characterization on the micro/nanostructure and composition of the TiAl/Ti₃Al/Al₂O₃ cermet

Many studies on the TiAl/Ti₃Al/Al₂O₃ cermet have been focused on processing and sintering. For example, Huy et al. [3.20] investigated the microstructure, hardness and fracture toughness of the Ti₃Al/Al₂O₃ cermet manufactured under an in-situ combustion process. In other studies, Zhu et al. [3.22] discussed the transitional reaction process in reaction sintering of the TiAl/Al₂O₃ cermet. Shen et al. [3.17] investigated the electronic structure of the titanium aluminides-alumina cermet from an in-situ SHS process. The summary to date of this material points to the need to develop a detailed report on the micro/nanoscale features. The microstructure of the material needs to be examined in all aspects in order to establish the relationship between microscopic features and mechanical properties. The current paper presents a more detailed characterization work to better summarize the microscopic features of the material.

In the present study, we initially examined the microscale features of the cermet by using SEM, EDS, and XRD. It was found that a heterogeneous microstructure can be achieved by the SHS process, and the alumina phase contributed $65 \pm 1\%$ in composition. A “coral” network was defined to describe the connected alumina particle clusters within our TiAl/Ti₃Al/Al₂O₃ cermet. In EDS mapping, it was confirmed that oxygen existed in regions with high concentrations of titanium, and this provided the proof of the existence of α_2 -phase that was shown in the XRD results. By consulting the ternary phase diagram of the Al-Ti-O system [3.37], the current cermet with an oxygen-rich α_2 -phase of titanium aluminide falls inside the predicted area in which the three phases (γ -TiAl, α_2 -Ti₃Al, and Al₂O₃) co-exist based on the overall atomic composition gathered from EDS (see Table. 3.2). In other studies, Shen et al. [3.17] and Zhang et al. [3.38]

have discovered a two-phase ($\gamma + \alpha_2$) lamellar structure to have appeared in the TiAl/Ti₃Al/Al₂O₃ cermet, as a result of the co-existence of individual γ and α_2 -phases. They concluded that the ($\gamma + \alpha_2$) structure would have a positive effect on the toughness of the cermet, due to the increased oxygen precipitation at the interface. Forouzanmehr et al. [3.40] fabricated the TiAl/ α -Al₂O₃ by mechanical alloying, where no additional α_2 -phase and its corresponding lamellar structure was identified in the material. Numerous SEM studies have also been conducted on similar cermets fabricated by different methods. Fine microstructures of the TiAl/Ti₃Al/Al₂O₃ cermet have been produced by Shen et al. [3.17] using SHS, Zhu et al. [3.22] using Reaction Synthesis (RS), and Travitzky et al. [3.39] using Pressure-assisted Thermal Explosion. However, the microstructure looked much coarser when fabricated using mechanical alloying [3.40]. Huy et al. [3.20] discovered a similar alumina “coral” network as the current cermet under 1173 K with Combustion Sintering (CS). It is believed that the SHS process can be one of the best manufacturing techniques for generating such cermets in significantly short sintering times, where the existence of the α_2 -phase is guaranteed. This information is valuable in material design and manufacturing, where the microstructure and composition of the material can be tied back to the fabrication methods. To further elaborate, the existence of the α_2 -phase, homogeneity, fineness of the microstructure, and state of the alumina phase could all have positive effects on the material performance.

Next, we investigated the nanoscale microstructural features of the cermet. The individual alumina particle sizes were found to be in the sub-micron range with an average of $1.0 \pm 0.3 \mu\text{m}$. Grain boundaries were found to be free of additives with no microcracks or plastic deformation, while the “coral” network of alumina particles was further examined using EDS. Additionally, TEM analysis on individual grains showed iron-nickel nano-precipitates distributed uniformly throughout the entire material. The nano-precipitates were most likely in the form of metallic and

oxide of iron and nickel [3.32 – 3.35]. In the literature, Kamali et al. [3.21] have shown the capability of controlling the grain size of the TiAl/Al₂O₃ cermet by adding KClO₄ to the mixture of the starting powders (TiO₂/Al). In other cermets, the effects of nano-precipitates on the mechanical properties of cermets have been studied. For example, Zhang et al. [3.41] discovered that the addition of nano-Si₃N₄ particles had shown improvements on the hardness and transverse rupture strength of the Ti (C, N)-based cermet by 1.3% and 25.2%, respectively. Other studies have shown abilities in improving Rockwell hardness, fracture toughness, and flexural strength by tailoring microstructure with nano-powders in TiC-based and TiAl-based cermets [3.19] [3.42] [3.43]. The effect of iron/nickel nano-precipitates on the behavior of the current cermet is yet to be determined. Overall, these findings encourage material design, which could give various enhancements based on industrial needs, including controlling the grain size by changing the phase compositions or adding nano-precipitates, where the mechanical properties of the final product could be tailored as well.

5.2. Rate-dependent failure mechanisms

In this section, the rate-dependent failure mechanisms of the cermet are discussed in terms of the stress-time responses and cracking behavior. In the present study, clear differences can be seen from the stress-history curve under the different loading rates. The quasi-static stress response exhibited similar behavior to that of the elastically deformed ceramics, where a linear increase in the stress-time profile was observed. The peak stress was reached without observing any surface deformation or cracking. In contrast for dynamic loading, the material exhibited plastic deformation, where several rises and drops of the stress were observed in the stress-time history curve. This is believed to be the result of the alternating thermal softening and strain hardening phenomena in the TiAl/Ti₃Al matrix (confirmed through imaging which is discussed next). This

has been observed previously by Wu et al. [3.44] during adiabatic shear banding in 7003-T4 aluminum alloy under high strain rate impact. It is believed that the heat accumulates locally in the specimen during high rate loading, which results in thermal softening of the titanium aluminide phase and contributes to local crack initiation. However, this can be overcome by strain or strain rate hardening, where texturing was observed in our TiAl/Ti₃Al/Al₂O₃ cermet before crack initiation and catastrophic failure. In other ceramic studies, the stress-history behavior of the ceramic under dynamic loading was significantly different, where a linear elastic triangular pulse was observed [3.45 – 3.47]. This gives further proof for the hypothesis that additional deformation mechanisms other than brittle fracture occur in the current cermet during dynamic loading. However, texturing coupled with thermal softening can be a potential disadvantage in ballistic performance since the material will be softened for a certain amount of time (in terms of microseconds) during loading, and this will significantly decrease the duration of the dwelling phase. As a result, more energy will be transferred to the deeper layer of armor without enough destruction of the projectile [3.48] [3.49]. Future improvement on the material design perspective should be directed towards minimizing this effect.

Next, high-speed imaging revealed strain-rate dependent failure mechanisms. Quasi-statically, cracking always followed a path with the fracture angle of 54 ± 3 degrees (measured from the top edge) (see Fig. 3.7 image 6) across the whole specimen upon failure, and no crack branching was observed. It is believed that the cermet fails majorly through intergranular fracture at low strain rates. Crack propagation will likely follow along with the “coral” alumina network and alumina grain boundaries in the material, and the onset of failure could be from interfacial flaws or micropores. In contrast, texturing was observed on the material surface in dynamic loading before and during cracking (see Fig. 3.8 image 1-4). In addition, several primary and secondary crack

branches were observed (see Fig. 3.8 image 3-6). In all experiments, the primary cracks propagate with an angle between 50 and 60 degrees towards the center of the specimen, while random branching occurred during further loading. It is believed that the material fails through a combination of intergranular and transgranular cracking along and through the alumina phase. This is because more kinetic energy is introduced into the material during impact, which allows cracks to propagate through the much harder alumina grains with a much smaller time scale. The crack speeds of the cermet were measured at 700 m/s to 1200 m/s under dynamic loading with an average of 960 ± 210 m/s. Note that only crack speeds for the dynamic loading case are considered here because the quasi-static cracking could not be measured with the current setup. Similar mechanisms have been identified in the TiC/Steel cermet with the aid of TEM by Kaplan et al. [3.11]. It was found that transgranular fracture was the dominant failure mechanism under dynamic loading, and micro-crack toughening was found to be another mechanism, which extensively contributes to dynamic failure. When compared to advanced ceramics, Acharya et al. [3.50] studied the failure mechanism of AD995 under high strain rate loading and reported that plasticity, such as dislocation array and transgranular microcracking could occur, resulting in failure. These mechanisms may also be activated in the nano-grained alumina in our cermet, as well as other plastic deformation mechanisms in the titanium aluminide phase (e.g., twinning and dislocation) [3.62 – 3.65]. In addition, the fragmentation behavior of the cermet is vastly different from what is observed in some typical advanced ceramics. For the cermet, less cracking and larger structural fragments were found after failure. When compared with ceramics such as shown in Hu et al. [3.28] for aluminum nitride and Hogan et al. [3.51] for silicon carbide, much denser cracks were observed at the onset of failure, and the material seemed to powder and explode upon catastrophic failure.

This particular feature of the cermet can, perhaps, be beneficial in multi-hit capacity for body armor if proper confinement is established.

5.3. Comparison of the rate-dependent mechanical properties with alumina AD995

In this section, the compressive strength of the cermet is discussed in the context of comparison with alumina AD995 (refer as AD995 later in the text) manufactured by Coorstek Inc., which is a typical advanced ceramic being used as insert in body armors that has a similar density as the TiAl/Ti₃Al/Al₂O₃ cermet ($\sim 3.9 \text{ g/cm}^3$). To do this, we show the strength-strain rate plot of AD995 and the TiAl/Ti₃Al/Al₂O₃ cermet in Figure 3.10. The AD995 data have been gathered from both experiments conducted in the lab by using the same experimental setup and as well as data results collected from the literature [3.45] [3.50] [3.52]. In the cermet experiments, the quasi-static compressive strength of the cermet has an average of $2400 \pm 120 \text{ MPa}$, while the dynamic compressive strength has an average of $3370 \pm 450 \text{ MPa}$. This gives approximately 1.5 times increase in strength with a seven order increase in strain rate. For the rate-dependency on compressive strength of other cermets, Mandel et al. [3.12] and Marchi et al. [3.61] found an approximately 1.5 times increase in strength in the WC-Co system (from 4370 MPa to 6660 MPa with 10^{-4} s^{-1} to 10^3 s^{-1} strain rate) and 55 vol% Al₂O₃/Al cermet (from $\sim 400 \text{ MPa}$ to $\sim 600 \text{ MPa}$ with 10^{-4} s^{-1} to 10^3 s^{-1} strain rate), respectively. Guden and Hall [3.13] and Zhu et al. [3.60] also found an approximately 1.3 times increase in the 35 vol% Al₂O₃/Al (from $\sim 260 \text{ MPa}$ to $\sim 340 \text{ MPa}$ with 10^{-3} s^{-1} to 10^3 s^{-1} strain rate) and TiB₂/Al (From $\sim 900 \text{ MPa}$ to $\sim 1200 \text{ MPa}$ with 10^{-4} s^{-1} to 10^3 s^{-1} strain rate) cermets, respectively. Similarly, the quasi-static compressive strength of AD995 has an average of $2444 \pm 247 \text{ MPa}$, while the dynamic compressive strength has an average of $3590 \pm 493 \text{ MPa}$. This gives approximately 1.5 times increase as well. The order of increase in the compressive strength of these materials is comparable. In conclusion, clear rate-dependency

on compressive strength can be observed in both TiAl/Ti₃Al/Al₂O₃ cermet and AD995, and the current cermet has comparable strength with AD995 under both loading conditions. This is important to note because compressive strength has been identified to be important by some in ballistic protection applications [3.53].

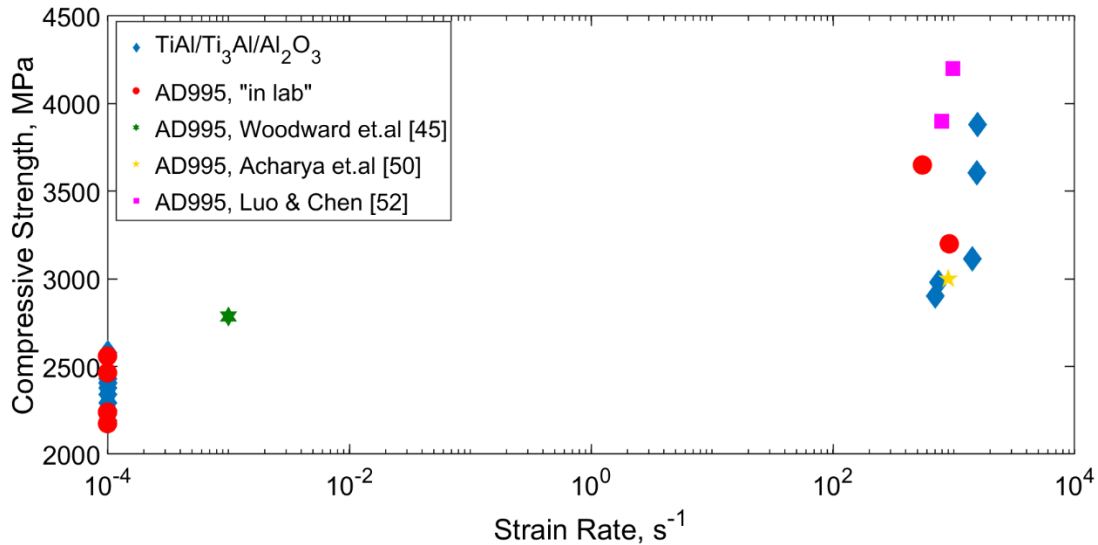


Figure 3.10: Summary of the compressive strength of the cermet with respect to strain rate under uniaxial compression with comparison to alumina AD995 manufactured by Coorstek. The alumina data was gathered from both experiments conducted in the author’s lab and data reported in literature.

Lastly, the failure strain was measured under both loading rates. The average failure strains of the cermet are $1.4 \pm 0.2\%$ and $3.1 \pm 0.1\%$ under quasi-static and dynamic uniaxial loading, respectively. For other cermets, such as WC/Co, TiC/Ni, Al₂O₃/Cr, and B₄C/Al, the failure strains were between 0.3% and 2.0% quasi-statically depending on the composition [3.54 – 3.56]. Failure strain of the TiAl/Ti₃Al/Al₂O₃ cermet falls at the higher end of this range, which points to some positive aspects of this materials. Lankford [3.46], Luo and Chen [3.52], and Krell and Strassburger [3.53] have conducted SHPB experiments on AD995 to assess the dynamic behavior. In those studies, the dynamic failure strain was between 1.0% to 1.5%, whereas the quasi-static failure strain was measured between 0.5% to 0.8% from the tests presented in Figure 3.10. The failure strain of the

TiAl/Ti₃Al/Al₂O₃ cermet is more than twice higher than AD995 under both loading conditions. One drawback of advanced ceramics like AD995 is that the brittleness of the material limits its ballistic performance, where catastrophic failure after the dwelling phase does not provide significant energy dissipation, and a thick metallic backing plate is usually needed [3.4]. With cermets being developed, ductility is introduced into the material to potentially overcome this limitation [3.4] [3.5]. For our TiAl/Ti₃Al/Al₂O₃ cermet, the fracture toughness of the material has been significantly improved over alumina based on the data provided by the manufacturer (see Table 3.1), while texturing has been observed under dynamic loading (see Fig. 3.8). It needs to be noted that the occurrence of plasticity and increase in toughness of the cermet should be examined in a more systematic way with fractography (SEM/TEM) and the stress-strain curves. The conclusion presented above is based on published data and observations on surface deformation. In summary, since damage tolerance capacity and hardness are both critical factors in determining the efficiency of energy dissipation and mass defecation during perforation, there is a need to identify the best trade-off between hardness and fracture toughness to further improve the ballistic efficiency of body armors.

6. Concluding remarks

In this study, the behavior of the TiAl/Ti₃Al/Al₂O₃ cermet was investigated using microscopic characterization and mechanical testing. Detailed characterization, including scanning electron microscopy and transmission electron microscopy, revealed the microstructural and nanostructural features, where a “coral” network of alumina particles was identified. Energy-dispersive X-ray spectroscopy and x-ray diffraction identified the phase composition and elemental concentration of the cermet, where it was found to contain γ -TiAl, Al₂O₃, and an additional α_2 -Ti₃Al phase was found as a by-product in the SHS process. Iron and nickel-based nano-precipitates were also found

throughout the material. The rate-dependent stress-strain response, compressive strength, and failure mechanisms were investigated by quasi-static and dynamic uniaxial compression coupling with high-speed imaging, where alumina AD995 was used as a reference for comparison. Comparable compressive strengths, higher failure strains, and larger structural fragments were identified for the TiAl/Ti₃Al/Al₂O₃ cermet, when compared to AD995. In addition, texturing was clearly observed under dynamic loading, and a hypothesis was proposed on the occurrence of plastic deformation taking place in the cermet during failure. The data generated in this study provides guidelines for future material improvement, manufacturing, and simulation.

Chapter 4: On the Rate-Dependency of Mechanical Properties and Failure Mechanisms of a ($\gamma + \alpha_2$) - TiAl/Ti₃Al- Al₂O₃ Cermet²

This chapter is adapted from the second paper written by the author and sent for review in *Composite Part B: Engineering* at the date of submitting this thesis. The texts, tables and figures including their numbering, and references are kept as they appeared in the article. In addition to the previous chapter, high-speed imaging coupled with digital image correlation are used to explore the rate-dependent stress-strain behavior, surface deformation, and fragmentation. Detail characterization is conducted to probe rate-dependent failure mechanisms. Both micro and nano-scale failure mechanisms are characterized in detail and compared with other cermet systems, for which some of these mechanisms has been incorporated into the unit cell micromechanical model [64].

² Information in this chapter is under review in *Composite Part B: Engineering*.

On the Rate-dependency of Mechanical Properties and Failure Mechanisms of a $(\gamma + \alpha_2)$ - TiAl/Ti₃Al-Al₂O₃ Cermet

Haoyang Li^{a,*}, Pouyan Motamedi^{a,b}, James David Hogan^a

^a *Department of Mechanical Engineering, The University of Alberta, Edmonton, AB T6G 2R3, Canada*

^b *Nanotechnology Research Centre, National Research Council Canada, 11421 Saskatchewan Dr., Edmonton, AB T6G 2R3, Canada*

Abstract

This study investigated the rate-dependent mechanical properties and failure of a self-propagating high-temperature synthesized TiAl/Ti₃Al-Al₂O₃ cermet using mechanical testing and advanced microscopy. Quasi-static and dynamic uniaxial compression tests coupled with high-speed imaging and digital image correlation were used to determine the rate-dependency of stress-strain behavior, compressive strength, and failure strain. The stress-strain curves in the dynamic experiments exhibited a series of alternating stress relaxation and strain hardening cycles, where a 1.3 times increase in compressive strength from 2780 ± 60 MPa to 3410 ± 247 MPa, and a 1.4 times increase in failure strain from 0.0166 ± 0.0017 to 0.0264 ± 0.0032 were determined with a seven order increase in strain rates from $\sim 10^{-4}$ s⁻¹ to $\sim 10^3$ s⁻¹. It was also found that the cermet exhibits macroscopic surface texturing by examining the high-speed imaging of deformation during testing. Advanced microscopy, including scanning electron microscopy, high-resolution transmission electron microscopy, and two-dimensional x-ray diffraction were used to map out the failure mechanisms activated under the different loading rates. Globally distributed dislocations and twinning were observed as a consequence of dynamic loading, and extensive cleavage in the titanium aluminide phase, void growth, transgranular cracking, and particle fracture were identified as the dominant failure mechanisms activated under the high strain rate loading.

Crystalline texturing with profound microstructural evolution in the titanium aluminide phase was also found under dynamic loading, and this was correlated with the macroscopic surface texturing observed using high-speed imaging and the cyclical stress relaxation and strain hardening behavior in the stress-strain curves. This study presents a thorough understanding of the rate-dependency of the TiAl/Ti₃Al-Al₂O₃ cermet and provides insights in cermet material micromechanical modeling and improvement.

Keywords: cermet; two phase titanium aluminide; quasi-static and dynamic uniaxial compression tests; rate-dependency; compressive strength; stress-strain response; failure mechanisms; crystalline texturing; microstructural evolution; digital image correlation

1. Introduction

The mechanical properties of metal matrix composites (MMCs) and their performance under various loadings have been extensively studied (e.g., indentation [4.1], compression [4.2], tension [4.3], ballistic [4.4], and shock [4.5]). After the term “hardmetal” was introduced by Schwarzkopf and Kieffer in 1953 [4.6], research on how to combine ceramics and metallic alloys in order to improve their performance over their constituents has been occurring ever since. The term “cermet” was introduced in the 1960s to designate a material made of the combination of ceramics and metallic alloys, including “hardmetal”. The main motivation behind research on cermets has been to add the ductility of metals while preserving ceramic-like properties, such as high hardness and stiffness [4.4]. Early studies on cermets focused on manufacturing cutting tools by incorporating metallic alloys into systems like titanium carbide (TiC), tungsten carbide (WC), and titanium carbonitride (TiCN) [4.7, 4.8]. Mechanical properties of various cermet systems, including the SiC-Al system [4.9], TiC-Ni system [4.10], and WC-Co system [4.11], have been emphasized for

applications such as body armors [4.12], turbine blades [4.13], and coating for cutting blades [4.13], where the first two require high strength-to-weight ratio and the third requires high hardness.

Much of the published literature on cermets is dedicated to the characterization of quasi-static mechanical properties and their relation to composition and microstructure [4.14 – 4.16]. Recently, other forms of cermets have gained interest for applications in extreme environments, such as high temperature and high loading rates. For example, Rittel et al. [4.17] investigated the high-rate mechanical behavior of a TiC-1080 steel cermet, and Ramesh and Ravichandran [4.18] studied the dynamic behavior of B₄C-Al cermet. However, little information is available on the rate-dependent behavior and fracture mechanisms of oxide cermets even though they have gained interests for defense and wear applications [4.8]. This is likely a consequence of the poor wettability between oxide-type ceramics (e.g., Al₂O₃ and ZrO₂) and metals using conventional fabrication methods. This accompany with challenges in manufacturing and, thus, studying them dynamically. The poor wettability of oxide cermets leads to a reduction in toughening effects by the metallic phase [4.8], a counterproductive effect in cermet development. The dynamic behavior of the oxide-based cermets is nevertheless of primary importance since the mechanical and fracture responses are essential for understanding the material, as well as improving their usage in impact or other high-pressure applications [4.19].

Among promising oxide-based cermets for protection applications is the TiAl/Ti₃Al-Al₂O₃ cermet. The two phase titanium aluminide alloys, including the γ -TiAl and α_2 -Ti₃Al phases, have attracted attention in recent decades because of their low density (3.7 – 4.7 g/cm³), high melting temperature (~ 1500 °C), and good combination of stiffness (~ 180 GPa), specific strength (100 – 150 MPa/gcm⁻³), and toughness (11 – 20 MPa√m) [4.20 – 4.23]. In addition, alumina (Al₂O₃) with its adequately low density (~ 3.9 g/cm³) and moderate strength in the family of advanced ceramics

(e.g., stiffness of 370 GPa and compressive strength of 2600 MPa for alumina AD995 reported by Coorstek. Inc. [4.24]), is still one of the preferred candidates for some protection applications in defense due to its low cost and availability [4.25]. With the advancement in manufacturing techniques such as reaction synthesis (RS) and spark plasma sintering (SPS), combining the titanium aluminide alloys with alumina to form a cermet seems promising due to their comparable densities ($\sim 3.9 \text{ g/cm}^3$) and coefficients of thermal expansion ($\sim 8.2 \times 10^{-6} / ^\circ\text{C}$ for alumina [4.24] and $\sim 8.5 \times 10^{-6} / ^\circ\text{C}$ for titanium aluminide [4.26] at room temperature). One such fabrication method includes the self-propagation high-temperature sintering technique used in the present study to fabricate the TiAl/Ti₃Al-Al₂O₃ cermet, which has been noted by Levashov et al. [4.27] to yield better interface bonding between the matrix and the particles by direct phase forming from chemical reactions. To date, literature published on the TiAl/Ti₃Al-Al₂O₃ cermet has focused primarily on novel manufacturing processes and powder mixture formulations, with limited experimentation studies on their rate-dependent mechanical properties and fracture mechanisms [4.28 – 4.32]. For example, Shen et al. [4.33] reported the quasi-static fracture toughness of a TiAl/Ti₃Al-Al₂O₃ cermet as a complementary part to discuss the quality of fabrication, while Lapin et al. [4.34] discussed the effect of the size and volume percentage of the alumina particles on the Vickers hardness and room-temperature quasi-static compression properties of a directionally-solidified titanium aluminide alloy. The limited information on high-rate properties of TiAl/Ti₃Al-Al₂O₃ cermets will need to be addressed before the material can be further utilized for commercial applications in, for example, body armors and turbine blades, where high velocity impacts are prevalent.

To address the gap in evaluation and understanding of the rate-dependent material properties and failure behavior, the current study explores the stress-strain responses of a self-propagating high-

temperature synthesized TiAl/Ti₃Al-Al₂O₃ cermet under quasi-static and dynamic compressive loading rates. Novel digital image correlation (DIC) techniques coupled with high speed imaging is used to extract the strain field during testing. The rate-dependency of mechanical properties and fracture mechanisms are observed and discussed further by using mechanical testing and microscopic diagnostic. Scanning electron microscopy (SEM) and high-resolution (scanning) transmission electron microscopy (HR-TEM/STEM) are used to probe the micro and nano-scale deformation mechanisms activated under the quasi-static and dynamic loading rates. Possible phase transformation and crystalline texturing are also investigated through the use of two-dimensional x-ray diffraction (2D-XRD). In the discussion, length scale-dependent failure mechanism observed using high speed imaging and advanced microscopy are linked with rate-dependent stress-strain behavior (i.e., stiffness, the stress relaxation and strain hardening phenomena, peak stresses, and failure strains). From there, we compare these behaviors with those observed in other advanced ceramics and cermet systems. Lastly, this study concludes with discussion of implications for ballistic applications in the context of the new understanding on rate-dependent properties and mechanisms in this cermet system.

2. Material microstructure and preparation

2.1 As-received material microstructure

Multiple approaches can be used to fabricate the TiAl/Ti₃Al-Al₂O₃ cermet, including mechanical alloying [4.32] and reaction sintering [4.35]. Different fabrication methods produce vastly different microstructures [4.36, 4.37], where these microstructures have effects on the material performance. For example, Travitzky et al. [4.37] produced an interpenetrating phase morphology of a TiAl/Al₂O₃ cermet synthesized by thermal explosion with a continuous alumina network (grain size ~ 3 μm). In the Travitzky et al. [4.37] study, the material had a fracture toughness of

7.1 MPa \sqrt{m} . In a separate approach, Forouzanmehr et al. [4.32] obtained a nanograined TiAl/ α -Al₂O₃ cermet (~ 58 nm grain size for TiAl and ~ 50 nm for Al₂O₃) via mechanical alloying. In the current study, the TiAl/Ti₃Al-Al₂O₃ cermet is manufactured by Luminant Corporation, British Columbia, and it is fabricated through the self-propagation high-temperature sintering (SHS), which is a highly exothermic reaction process under high pressures and temperatures. Figure 4.1-a presents a backscattered FESEM micrograph of the polished surface of the as-received material in this study. The micrograph is obtained using a Zeiss Sigma FESEM machine. An ultrafine but heterogeneous microstructure is formed in the cermet, and the alumina phase (darker regions) appears as a cluster network in the material, as was the case in Huy et al. [4.133]. The grain size for an individual alumina particle is between 0.5 μ m and 1.5 μ m with an average of 1.0 ± 0.3 μ m, and the areal fraction of the alumina phase is estimated at $65 \pm 1\%$. The areal fraction of the voids constitutes $\sim 2\%$ of the image, and this correlates well with the results reported in a previous study by the authors [4.37]. This information is averaged over five locations for each surface investigated. As a result of the high content of ceramic phases and the relatively low ductility of intermetallic titanium aluminide phase, the cermet behaves in a brittle manner. Figure 4.1-b shows a FESEM image of a cleaned fracture surface of the as-received material. This surface was obtained from the as-received plate, where a piece was sectioned out to investigate the internal microstructure. Both equiaxed and columnar grain structures of the titanium aluminide phases are observed in the material, which correspond to the γ and α_2 titanium aluminide grains and $(\gamma + \alpha_2)$ -TiAl/Ti₃Al lamellar structure (indicated by blue arrows), respectively. The red arrows in Figure 4.1-b point to the individual alumina grains which appear brighter than the gray titanium aluminide grains. All phases are identified through EDS analysis by comparing the relative elemental concentrations of aluminum, titanium and oxygen.

Figure 4.1-c demonstrates a representative bright field TEM image of the individual grains and the grain boundaries before experiments, showing clean and closely bonded alumina-alumina and titanium aluminide-alumina interfaces. This micrograph is obtained using a FEI Tecnai TF-20 FEG/TEM machine. The alumina grains and titanium aluminide grains are separated by dashed lines and marked on the micrograph. The empty spaces at the boundary of some alumina grains are the pores present in the material, and this confirms the observation of pore sites in the previous study by the authors [4.37]. In the micrograph in Figure 4.1-c, an alumina cluster is observed at the top right corner, which verifies the presence of alumina networks observed in the BSE-SEM image (see Fig. 4.1-a). Residual stress is also observed in alumina, as manifested in the darker contour lines connecting the boundaries of alumina grains (alumina composition confirmed with EDS). This is likely the result of rapid forming explosive SHS process used to fabricate the material, as well as the mismatch in thermal expansion coefficient between alumina and titanium aluminide. In the alumina grain at the top left corner of Figure 4.1-c, dislocations (indicated by white arrows) are observed and they appear to bisect from the residual stress contour lines. This suggests some plastic deformation exists in the as-made material because of the highly energetic fabrication process. It is also observed that a microcrack (indicated by a red arrow) initiates from the tip of a dislocation and propagates through the alumina grain, but it is arrested by the titanium aluminide matrix. In the titanium aluminide phase, a duplex microstructure is observed, with some clean γ -grains (e.g., bottom left) and γ -grains with randomly orientated ($\gamma + \alpha_2$) lamellae (e.g., bottom right) (titanium aluminide phase compositions confirmed by EDS). Some dislocations are observed in between the lamellar structure, but most of the titanium aluminide grain surfaces are clean and free of plastic deformation.

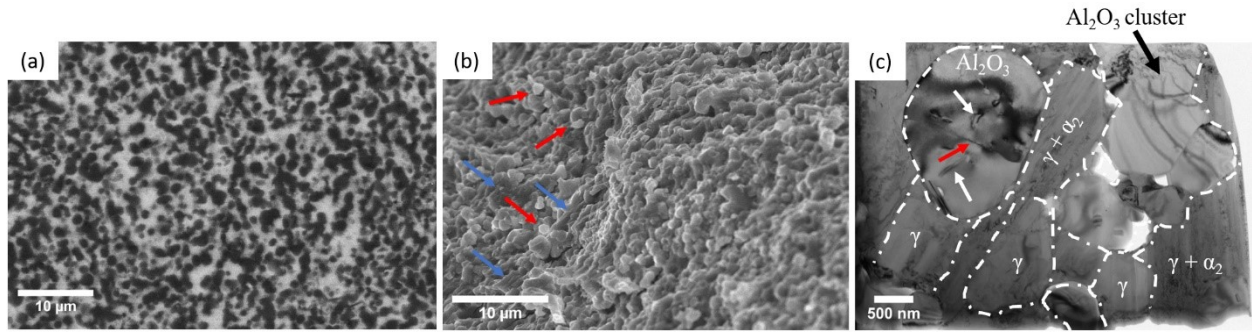


Figure 4.1: SEM and TEM micrographs examining the microstructural features of the as-received material. (a) BSE-SEM image on the polished surface showing the phase distribution and alumina clusters; the black regions correspond to the alumina phase and the white regions correspond to the titanium aluminide phases; (b) FESEM image on cleaned fracture surface showing shapes and sizes of alumina and titanium aluminide grains; the red arrows indicate the individual alumina grains, and the blue arrows point to the $(\gamma + \alpha_2) - \text{TiAl/Ti}_3\text{Al}$ lamellae. The titanium aluminide phase appears grayer in the image than the brighter alumina grains; (c) Bright field TEM image showing grain surfaces and grain boundaries. Residual stresses are present on most of the alumina grains, where dislocations (white arrows) and microcrack (red arrow) are observed on the alumina grain at the top left corner. Duplex microstructure of titanium aluminide phase, including clean γ grains and $(\gamma + \alpha_2)$ lamellae on γ grains are obtained. No specific orientation of the lamellar structure is found in the as-received material.

2.2 Sample preparation for mechanical testing

Once materials were characterized, mechanical testing was performed. The material was provided as circular tiles (93 mm in diameter and 6.5 mm thick), from which cuboid specimens were machined via electrical discharge (EDM) for rate-dependent compression experiments. The cut specimens were post-polished down to a 0.1 microns surface finish to reduce effects by surface roughness and defects. Parallelism of the specimen surface (in terms of length along the loading direction) was carefully examined to be less than 1° on all surfaces. The uniaxial compression specimens (both quasi-static and dynamic) had dimensions of 2.3 mm x 2.7 mm x 3.5 mm. Loading was always carried out along the thicker (3.5 mm) side of the specimens, and this was in a direction that was parallel to the thickness direction of the as-received tile. The specimen dimensions were reduced by a factor of 1.5 following Farbaniec et al. [4.39], and they were chosen to compensate for both quasi-static and dynamic setups, as well as providing a sufficient surface area needed for good quality DIC analysis.

For postmortem analysis, fragments were recovered from the quasi-static and dynamic experiments, and they are used for microscopic diagnosis on both their surface and through investigation of internal damage. Parts of the fragments were investigated using SEM and TEM in their as-deformed state. Some fragments were cold mounted into epoxy resin and systematically polished for further study via SEM, TEM, and XRD. The mounted disks were polished down at least 500 μm from the surface to reveal the sub-surface damage, and the final surface finish was set at 0.1 μm finish.

3. Experimental setup

3.1 Microscopic diagnoses

3.1.1 Scanning electron microscopy

Scanning electron microscopy (SEM) analysis was carried out on both fractured and polished fracture surfaces to evaluate the microscale failure mechanisms under both quasi-static and dynamic loadings. The micrographs were taken using a Zeiss Sigma FESEM machine equipped with an energy-dispersive x-ray spectroscopy (EDS) setup. The machine was operated with the acceleration voltage set at 20 kV and a working distance of ~ 3.8 mm. An In-Lens detector was used to image the fracture features, including crack path, particle debonding, and plastic deformation mechanisms. The EDS probe was used to verify the compositions of the microstructural features presented in the corresponding field of view. No coating was needed for the specimen since conductivity was an inherent property of the intermetallic phase in the composite. The EDS data was analyzed using the AZtec software from Oxford Instruments. On average, at least two fragments per test were scanned to confirm the universality of the observed mechanisms, and micrographs revealing the representative fracture mechanisms were presented.

3.3.2 Transmission electron microscopy

High-resolution transmission electron microscopy (HR-TEM) was conducted on the material before and after testing to investigate the nanoscale deformation mechanisms, such as microstructural evolution, dislocation, and twinning. The TEM sample preparation and imaging were carried out at Eurofins EAG Laboratory located in California, USA [4.40]. The TEM samples were prepared from the same polished epoxy disks used for SEM analysis, and they were further prepared to be TEM-ready using the in-situ focus ion beam (FIB) lift out technique on a FEI Strata 400 Dual Beam FIB/SEM system. With in-situ SEM identification, an approximately $4.5 \mu\text{m} \times 4.5 \mu\text{m}$ area of interest was extracted using FIB in the vicinity of a microcrack, where most deformation mechanisms are expected to be seen. Once the area of interest was defined, the samples were capped with sputtered Ir and e-Pt/I-Pt before sending for ion milling. Through ion milling, the final TEM lamella thickness was reduced to $\sim 100 \text{ nm}$. After preparation, the samples were imaged with a FEI Tecnai TF-20 FEG/TEM operated at 200kV in bright-field (BF) TEM mode, high-resolution (HR) TEM mode, and high-angle annular dark-field (HAADF) STEM mode with a 0.2 nm nominal diameter STEM probe. Energy-dispersive x-ray spectroscopy (TEM-EDS) analysis was performed to identify the phase compositions, and the spectra were acquired in STEM mode using the FEI Osiris 4SDD system. Special care was taken to eliminate the artificial EDS peaks (i.e., C, Cu, and Ga), which could come from sample preparation. Selected area electron diffraction (SAED) patterns were analyzed at different locations within the titanium aluminide and alumina phases to investigate the symmetry of the crystallographic structures.

3.3.3 X-ray diffraction

Two-dimensional x-ray diffraction (2D-XRD) analysis was carried out to assess the crystallinity and identify the phases of the as-received material and fragments obtained after testing. The tests

were carried out on a Bruker D8-Discover machine using Cu $K\alpha$ beam source. The apparatus was operated at 50 kV and 1000 μ A. A Vantec 500 detector was used to produce two-dimensional frames, which were then processed using the Bruker Eva software to produce θ - 2θ -equivalent spectra. A schematic of the test setup and the associated parameters is shown in Figure 4.2-a. This setup has been explained in more detail in the authors' previous publications [4.41, 4.42]. Figure 4.2-b shows a representative 2D frame. In any given frame, 2θ increases from right to the left, and Ψ values change along the denoted arcs. The distribution of intensity along Ψ signifies the randomness of the crystal orientations. In this representation, the solid arcs represent a completely random angle distribution, and the dashed arcs represent preferred orientation arising from the crystalline texture or large crystallites (see Fig. 4.2-b).

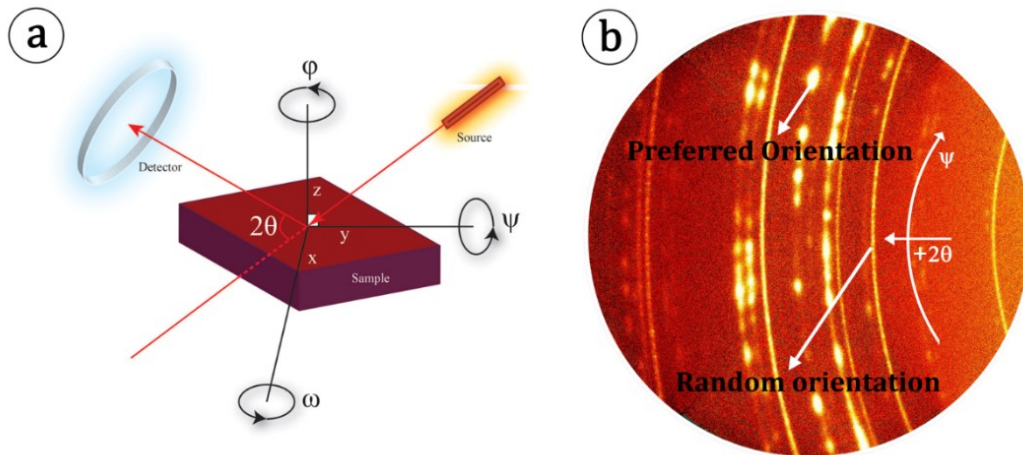


Figure 4.2: (a) Schematic of the 2D-XRD test setup and scan parameters; (b) A representative 2D frame showing typical arcs indicating a random orientation and a preferred orientation. The directions of integration (θ and Ψ) are from right to left and from bottom to top, respectively.

3.2 Mechanical testing

3.2.1 Quasi-static uniaxial compression testing

Quasi-static uniaxial compression tests were carried out on an MTS series 810 servo-hydraulic machine under displacement control with a nominal strain rate of $2 \times 10^{-4} \text{ s}^{-1}$. Ti-6Al-4V titanium alloy jacketed tungsten carbide (WC) platens were used to reduce indentation from the specimen

to the loading platens. Extreme pressure grease was applied between specimen and the WC platens to reduce the frictional effect and allow free lateral expansion. A 100 kN load cell and linear variable differential transformer were used to measure the force history and crosshead displacement, respectively. An AOS PROMON U750 high speed camera with a full resolution of 1280 x 1024 pixels was used to visualize the macroscopic surface deformation. High intensity LEDs coupled with optical light guides were used to obtain the high brightness and contrast in order to enhance the DIC strain field measurements. For data analysis, engineering stress and strain were extracted from the MTS force data and DIC measurements, respectively. A matching of the peak stress and strain before failure was performed to obtain the stress-strain curves. In addition, both the frame rate of the camera and sampling rate of the MTS machine were set at 100 FPS and 100 Hz to minimize delay and matching errors. Detailed schematics and descriptions of the experimental setup can be found in the previous study by Li et al. [4.37]. In total, five representative curves for the quasi-static strain rate were acquired to demonstrate variability.

3.2.2 Dynamic uniaxial compression testing

The dynamic uniaxial compression tests were carried out on a modified version of a split Hopkinson pressure bar (SHPB). This technique was developed by Kolsky [4.43] initially for testing metals and modified later to compensate for brittle materials, such as ceramics and cermets [4.44 – 4.47]. One well-documented setup of the modified SHPB can be found in Hu et al. [4.48] on testing the dynamic failure of aluminum nitride. Detailed information on the setup used in the current study can be found in the previous study by Li et al. [4.38], and only the critical and updated components are mentioned here for completeness. In the current study, bars (including the striker, incident and transmitted bars) were made from Maraging steel C-350 with a common diameter of 12.7 mm. The specimens were placed between two impedance-matched Ti-6Al-4V titanium alloy

jacketed tungsten carbide platens that were fixed to the opposite ends of the incident and transmitted bars, where the interfaces were lubricated with extreme pressure grease to reduce friction and allow the specimen to expand freely in the lateral dimension. A mild steel pulse shaper with a thickness of 0.0635mm was placed in front of the incident bar (against the striker) to create a ramped signal profile, while reducing the signal-to-noise level. This specific pulse shaper provided a proper rise time (8 to 10 μs) and ramp time for which the material could reach equilibrium under a single pass of the compressive loading wave, and the natural response of the material can be captured. In this case, the total time of the event was within 20 μs . In addition, the air tank pressure was set to 50 psi in all tests, and the nominal strain rate was between $1 \times 10^3 \text{ s}^{-1}$ to $2 \times 10^3 \text{ s}^{-1}$, depending on the response of material, variability in projectile speed, and uncertainty in strain measurements. For data acquisition, an HBM Gen3i High-Speed Recorder was used to capture the voltage signals at a sampling rate of 25 MHz. The transmitted signal was used to compute the stress-time profile.

An ultra-high-speed Shimadzu HPV-X2 camera was used to capture the failure process of the specimen during SHPB testing filming at 2 million frames per second with an exposure time of 200 ns, where 128 frames can be captured at the specified frame rate with a full resolution of 400 x 250 pixels. In this setup, a ring light from REL. Inc equipped with 32 high-power LED emitters with a focal point of approximately 13 inches was placed concentric to the camera lens to provide sufficient lighting to the specimen. This ring light would enhance the brightness and contrast, as well as providing an overexposure condition for the DIC analysis. Similar to quasi-static tests, DIC was used to obtain the global strain field in the dynamic tests. In this case, a K2 DistaMax lens from Infinity Photo-Optical Inc. was used to achieve a field of view, where the spatial resolution of the DIC analysis could be maximized. Stress and strain were matched in time by considering a

common trigger point in the system. In total, five representative curves were acquired for comparison with the quasi-static tests, as well as demonstrating the variabilities in mechanical responses.

3.3 Digital image correlation technique and setup

Digital image correlation was performed to obtain the global strain field from the specimen surface in both quasi-static and dynamic tests. A brief summary on the theory behind DIC analysis is provided here because of the novelty of the technique to cermets and brittle materials in general. In DIC analysis, an area of interest (AOI) is first defined, and displacements of the small subsets defined within the AOI are tracked as the specimen translates and deforms during loading [4.49]. The subsets in the deformed images are transformed to “match” the pattern in the reference image, and this “match” is performed as the total difference in gray scale intensity level at each interpolation point [4.49]. In each subset, a correlation peak is defined by interpolating the grayscale level at or between pixels, where the position of the peak provides a local displacement [4.50]. Therefore, the subset size is rather important in determining spatial resolution, and it is related to the specimen dimensions. However, there is no specific guidelines or published standards for determining the optimal subset size [4.51]. It is up to the user to decide an appropriate subset size which will output the necessary information as required. The selection of the subset size is discussed next.

In this study, VIC-2D 6 [4.52] software was used to map out the global strain fields in both quasi-static and dynamic tests. One advantage of the mentioned software is that the built-in algorithm provides a “suggested subset size” and noise level with the minimum estimated error based on the quality of speckle pattern and light intensity level using the reference frame. The software has been proven to be reliable by Sutton et al. [4.53] through calibration and error assessments. Considering

the size of the specimen, applying a good speckle pattern on the specimen surface was one of the biggest challenges in the analysis process. A non-repetitive, isotropic, and highly contrasted speckle pattern is crucial in DIC analysis. Conventional speckle pattern kits, or other methods, such as regular spray paint, are not applicable on specimens with such small size. Coarse speckle pattern will force the subset size to be large enough to contain at least two distinct speckles while losing too much spatial resolution. From Giacomo and Luca [4.54], the minimum speckle size should exceed the image pixel size by a factor of 3 to 5, and speckles smaller than this will result in aliasing. Shown in Figure 4.3-a and b are the typical speckle patterns obtained in the quasi-static and dynamic tests, respectively. Figure 4.3-a has a full resolution of 1280 x 1024 pixels (obtained with an AOS PROMON U750 high speed camera), and Figure 4.3-b has a full resolution of 400 x 250 pixels (obtained with a Shimadzu HPV-X2 ultra-high speed camera). The optimal speckle size has been chosen to be between 20 μm and 30 μm in both quasi-static and dynamic tests determined from their corresponding image pixel sizes. Isotropic and highly contrasted speckle patterns were able to be generated for both tests using a fine-point airbrush as is recommended in most DIC applications [4.53]. In this study, an ultra-fine point Harder and Steenbeck Infinity airbrush with a 0.15 mm diameter needle and nozzle was used to spray specialized metallic paint with particle sizes down to 0.1 micron onto the specimen surface. Output pressure from the compressor was set to 15 psi to ensure sufficient atomization of the paint. In addition, Jerabek et al. [4.55] indicated that a fine speckle pattern and light intensity gives a better result when it is under the condition of overexposure.

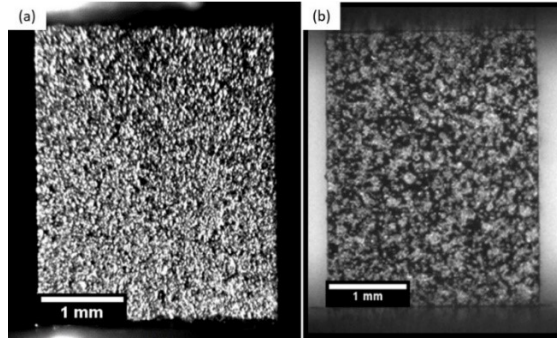


Figure 4.3: (a) A typical speckle pattern produced for DIC analysis for the quasi-static test. The compressive loading direction is vertical. (b) A typical speckle pattern produced for DIC analysis for the dynamic test. The compressive loading direction is vertical. Metallic paint was used for both cases in (a) and (b). The painted surfaces are always the biggest surface (2.7 mm x 3.5 mm) of the specimens. Isotropic and highly contrasted speckle patterns are obtained in both (a) and (b).

In the VIC 2D software, the “suggested subset size” for both quasi-static and dynamic tests were between 17 x 17 pixels and 25 x 25 pixels, which suggested a good quality of the speckle pattern. The “correlation step size” was manually tuned between 2 and 7 in each AOI to obtain smoother strain profiles. During the analysis, the zero-normalized squared sum of squared difference (ZNSSD) method was chosen to perform the correlation as it was proven to be one of the more robust algorithms that would not be affected by the offset in light intensity and linear scale in the illumination lighting [4.50]. A Gaussian low pass filter was selected to eliminate the high-frequency signals and pre-smooth both reference (the first frame showing an undeformed state of the specimen) and deformed images (all the subsequent frames). This pre-smoothing will increase the accuracy of the measurement because it filters out the bias signals, according to Pan [4.56]. The “Optimized 8-tap” interpolation scheme in the software was selected which incorporated the highest order of the spline scheme. In post-processing, the average rigid body motion was removed to compensate for any vibration caused during testing and possible interferences with the cameras. Equations for the algorithm used and settings in the software are documented in Table 4.1 for readers’ reference. The ZNSSD method (Eq. (1)) is an enhancement over the traditional sum of squared difference (SSD) first proposed as a correlation criteria by incorporating the mean

intensity functions (Eq. (2) and (3)) and root sum of squared differences (Eq. (4) and (5)) regarding each reference and deformed frames. This will reduce the systematic errors, even if a linear transformation of the target subset gray intensity is made [4.49].

Table 4.1: Equations for the algorithm and software settings used for DIC analysis in both quasi-static and dynamic tests

Criterion: ZNSSD [4.49]	$C_{ZNSSD} = \sum_{i=-M}^M \sum_{j=-M}^M \left[\frac{f(x_i, y_j) - f_m}{\Delta f} - \frac{g(x'_i, y'_j) - g_m}{\Delta g} \right]^2 \quad (1)$
	$f_m = \frac{1}{(2M+1)^2} \sum_{i=-M}^M \sum_{j=-M}^M f(x_i, y_j) \quad (2)$
	$g_m = \frac{1}{(2M+1)^2} \sum_{i=-M}^M \sum_{j=-M}^M g(x'_i, y'_j) \quad (3)$
	$\Delta f = \sqrt{\sum_{i=-M}^M \sum_{j=-M}^M [f(x_i, y_j) - f_m]^2} \quad (4)$
	$\Delta g = \sqrt{\sum_{i=-M}^M \sum_{j=-M}^M [g(x'_i, y'_j) - g_m]^2} \quad (5)$
Subset size	Between 17 x 17 pixels and 25 x 25 pixels
Step size	Between 2 and 7
Subset weights	Gaussian weights
Interpolation	Optimized 8-tap
Pre-filter	Low pass filter images
Consistency threshold (max margin) [pixels]	0.02
Confidence threshold (max margin) [pixels]	0.050
Matchability threshold (max margin) [pixels]	0.10

In Table 4.1: (x_i, y_i) and (x'_i, y'_i) are the coordinates of interpolation points in the reference (undeformed) and deformed frames, respectively; f and g refer to the intensity functions; $f(x_i, y_j)$ refers to the intensity function based on the displacement field in the reference frame; $g(x'_i, y'_i)$ refers to the intensity function in the deformed frames; and $(2M + 1)$ indicates the dimensions of the subset is are always odd.

4. Results

In this section, the results will be presented in the following order: 1. Stress-strain responses and macroscopic failure behavior; 2. Summary of compressive strengths at different strain rates; 3. Microscopy investigations on failure mechanisms; 4. Two-dimension x-ray diffraction exploring crystalline texturing. The results will be shown for both quasi-static and dynamic experiments.

4.1 Stress-strain responses and failure behavior

Shown in Figure 4.4 is the stress-strain responses obtained from five tests under quasi-static loading on the TiAl/Ti₃Al-Al₂O₃ cermet, named QS sp1 to QS sp5. The material is loaded uniaxially in the vertical direction in the inserts in Figure 4.4-b. Again, the stress is obtained from the MTS machine and the strain data is extracted by using DIC. The nominal strain rate in the quasi-static experiments is approximately $2 \times 10^{-4} \text{ s}^{-1}$ in all tests. This is estimated and confirmed by both taking the slope of the strain-time profile obtained from DIC analysis and tracking the edge displacements of the specimen among a sequence of images and then dividing by the corresponding time.

Shown in Figure 4.4-a are the quasi-static stress-strain behavior of the TiAl/Ti₃Al-Al₂O₃ cermet. Concaved stress-strain curves are observed for all tests with an initial linearly portion extended to approximately 0.002 strain. In this case, softening behavior on the instantaneous stiffness together with strain hardening of the TiAl/Ti₃Al-Al₂O₃ cermet is readily seen after a few microstrains. The stiffness of the cermet is measured at 0.001 strain by taking the slope of the stress-strain curves, which is measured between 230 GPa and 300 GPa, with an average of $267 \pm 28 \text{ GPa}$. This method has been documented elsewhere in literature for measuring the stiffness of several types of cermets [4.15, 4.16]; the 0.001 strain point is chosen by fitting a second order polynomial to the stress-strain curve, where a near-constant region within 3% difference in slope is selected by taking the

first derivative of the fitted polynomial. As a result, the 0.001 strain point is best suited for all five experiments, which also compensates the insensitivity in computing nanostrains at the beginning of the tests. The peak stress, which is often referred to as “quasi-static compressive strength,” for the quasi-static experiments is between 2700 MPa to 2900 MPa, with an average of 2780 ± 60 MPa. The failure strain, which is taken as the maximum strain value of the stress-strain curves, is between 0.013 to 0.018 for the quasi-static experiments, with an average of 0.0166 ± 0.0017 .

Next, the post-peak failure and fracture behavior of the cermet is shown in Figure 4.4-b for quasi-static case in the form of high-speed camera images. Two still images are selected from two of the five tests for a representation of the representative shape and size of the structural fragments that remain after the experiments. The two data points shown on the x-axis of the stress-strain curves at higher strains indicate the strains where images are extracted (right after the peak load), and the colors are matching to the same color in the stress-strain curves. Large structural fragments are observed after failure, with column-like shapes and height (taken horizontally) between 1 mm and 2 mm in size. Lamellar tearing (indicated by red arrows) along the loading direction shown as bands can be seen on the fragmented surface. The axially-orientated splitting is believed to be one of the deformation mechanisms activated in the titanium aluminide matrix under compression. Small amounts of crack branching are observed along with these major cracks at the macroscopic scale, indicating that the failure is likely caused by a single or several dominant cracks. These fragments will be examined later in Figure 4.7 using SEM for identification of the fracture mechanisms and damage accumulation at the micro/nanoscale.

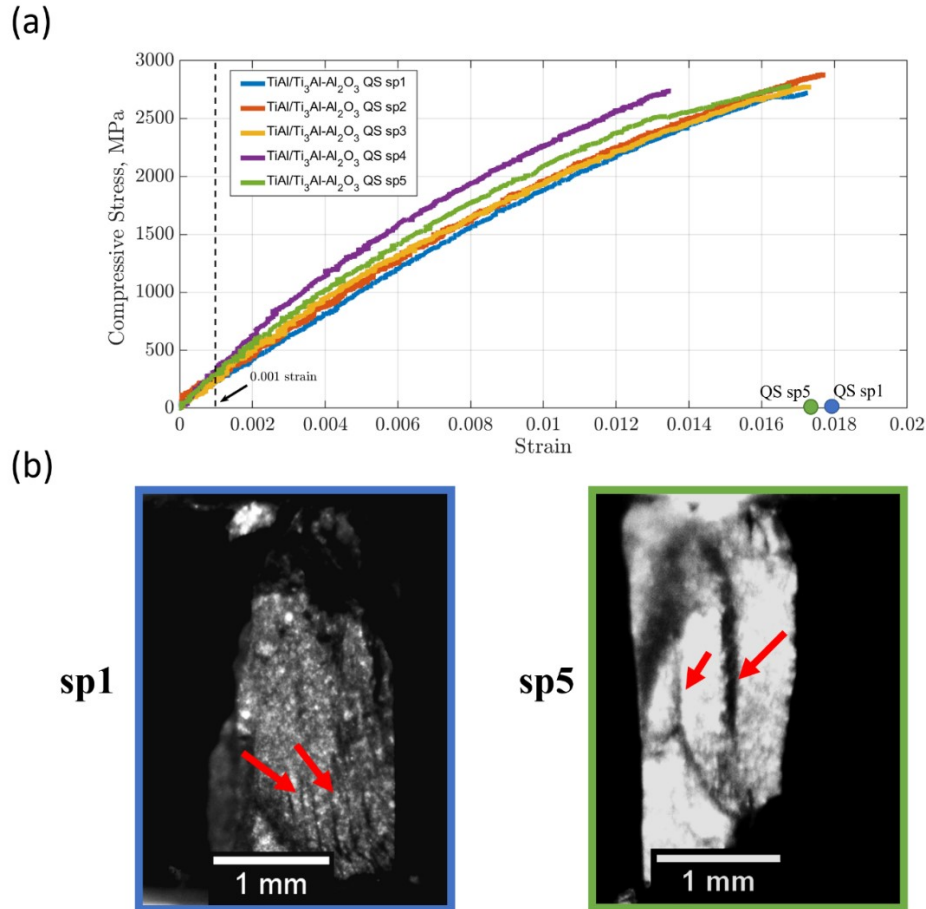


Figure 4.4: (a) Stress-strain curves of the TiAl/Ti₃Al-Al₂O₃ cermet under quasi-static uniaxial compression. The $x = 0.001$ strain line indicates where the stiffnesses are computed; (b) Still images showing typical post-peak structural fragments corresponding to two of the tests (QS sp1 & QS sp5) in (a). The data points on the x-axis in (a) are indications of when the images are extracted. The arrows shown in the fragment images are evidence of lamellar tearing along the loading direction, as one of the fracture modes under quasi-static loading.

Shown in Figure 4.5 is the material responses of the TiAl/Ti₃Al-Al₂O₃ cermet under high-rate loading, including stress-strain response (see Fig. 4.5-a) and ultra-high-speed camera still images showing fracture and fragmentation behavior (see Fig. 4.5-b). The material is uniaxially loaded in the vertical direction in the inserts in Figure 4.5-b. In total, five experimental results are plotted to demonstrate the representative stress-strain behavior, assess the variability in the material, and provide an adequate comparison with the quasi-static case. The strain rates in the dynamic experiments are between 1100 s^{-1} and 2000 s^{-1} . This is estimated by taking the average slope of

the upper bound and lower bound of the strain-time profile obtained through DIC analysis. From the figure, it is observed that the stress-strain curve increases linearly up to a certain yield point, where strain hardening starts to occur and a first peak is reached. After that, the second peak of the stress-strain curve is reached as a result of stress relaxation from the previous peak following by further strain hardening. The “alternating stress relaxation and strain hardening” behavior between two subsequent peaks is observed for the later peaks among all curves. The material is considered to be in unloading after the last peak in the stress-strain curve, and the post-peak stress-strain response is captured before fragmentation. In this case, a convex-shaped stress-strain behavior is observed, indicating that the material is continuously softening. Afterwards, the correlation is lost for even higher strains, and this is why the stress-strain curves do not return to zero stress in the figure. In all tests, at least two peaks are observed in each stress-strain curve, in which case a general trend of strength degradation in terms of peak stress values is observed with the first peak being the highest.

The highest peak, which is considered as the “dynamic compressive strength,” is between 3000 MPa and 3500 MPa across the five curves, with an average of 3133 ± 265 MPa. It is observed that the compressive strength is approximately 1.3 times greater than their counterparts in quasi-static loading. The stiffness, taken at 0.001 strain given the same reason as the quasi-static case, is between 240 GPa and 270 GPa, with an average of 255 ± 11 GPa. The stiffness of the cermet remains in a good agreement in both loading conditions. The failure strain, extracted from the stress-strain curves right before the first primary crack appears, is between 0.020 to 0.030, with an average of 0.026 ± 0.0032 . The failure strain is around 1.4 times the values obtained from the quasi-static case, with a seven order increase in strain rate from $\sim 10^{-4} \text{ s}^{-1}$ to $\sim 10^3 \text{ s}^{-1}$. It is observed that large variations in compressive strength and failure strain can be found in the material under

dynamic loading, corresponding to the high variability in mechanical response of the material. It is believed that the material microstructural variabilities and complexity of the fracture mechanisms under dynamic loading are responsible for the variability in the macroscale stress-strain responses, which is explored in subsequent sections.

Next, the in-situ failure and fracture behavior of the cermet under dynamic loading is examined by showing a series of ultra-high-speed camera images taken right before the onset of fragmentation (see Fig. 4.5-b). The loading is in the vertical direction. The corresponding experiment (DYN sp2) and strain (time) on the stress-strain curve is shown in Figure 4.5-a, where the dot represents the starting point of where the images are extracted. Images 1 and 2 constitute the last two frames of the stress-strain curve (see DYN sp2 in Fig. 4.5-a). The strain in the rest of the frames cannot be captured because of the loss in correlation in the DIC software. In image 1, the specimen is still mostly intact, where a horizontal crack is initiated at the middle of the specimen. In image 2, a splitting crack is also activated, and this propagates from the top edge of the specimen. It is deviated from the loading direction to the left at a $\sim 45^\circ$ angle towards the bottom left corner (indicated by red arrow). Simultaneously, a crack branch is formed at the center of the initial splitting crack and towards the bottom right corner (indicated by blue arrow). In image 3, the splitting crack and its corresponding crack branch have reached the bottom left and right corner of the specimen, respectively. Microcracks are activated at the top and bottom edges of the specimen at later times, and more crack branches are formed on the specimen surface. The specimen is at the onset of fragmentation at $\sim 18 \mu\text{s}$ (outside the DIC capture zoom). In image 4, the specimen starts to shatter, and more crack branches are observed on the surface. The cracks begin to interact and coalesce to form bigger crack networks at $\sim 20 \mu\text{s}$.

Image 5 shows the fragmentation behavior of the TiAl/Ti₃Al-Al₂O₃ cermet under dynamic loading. Much smaller structural fragments are observed in the dynamic experiments than in the quasi-static case, where the specimen fractured into irregular pieces after coalescence of the cracks. The crack speed in the dynamic experiments are between 2200 m/s to 3100 m/s, with an average of 2550 ± 480 m/s. This is estimated by considering the first two or three cracks in all of the videos. The speed is measured by tracking the position of the crack tip and length of the crack and taking the average over a few subsequent frames. Note that the crack speed in the MTS tests is inaccessible for the current setup; therefore it is omitted in this study.

Lastly, we show a sequence of representative still images taken from a dynamic experiment using the unpainted specimen (see Fig. 4.5-c) to illustrate a texturing phenomenon that is not as evidently seen with the painted surface. Image 1 is taken at the very beginning of the test where the specimen is still intact. In image 2, surface texturing (circled) starts to occur with higher concentrations at the middle region of the specimen, with no specific orientation determined. This image is taken near the first peak in stress of its corresponding curve (~ 0.01 strain). In images 3 and 4, the size of the textures continues to grow, where splitting crack and crack branches are observed on the surface. Image 4 shows the onset of the fragmentation, where a crack network is formed from crack growth and coalescence. These images are taken around the same timeframe (or ~ 0.03 strain) as image 3 in (b), where the splitting crack has propagated through the whole specimen, and the fragmentation has begun. It is believed that the surface texturing phenomenon observed under dynamic loading (not in quasi-static loading) is responsible for or the consequence of some observed rate-dependency and hardening/softening behavior in the stress-strain curve. We further investigate the associated dynamic failure mechanisms using XRD, SEM, and TEM in a later section.

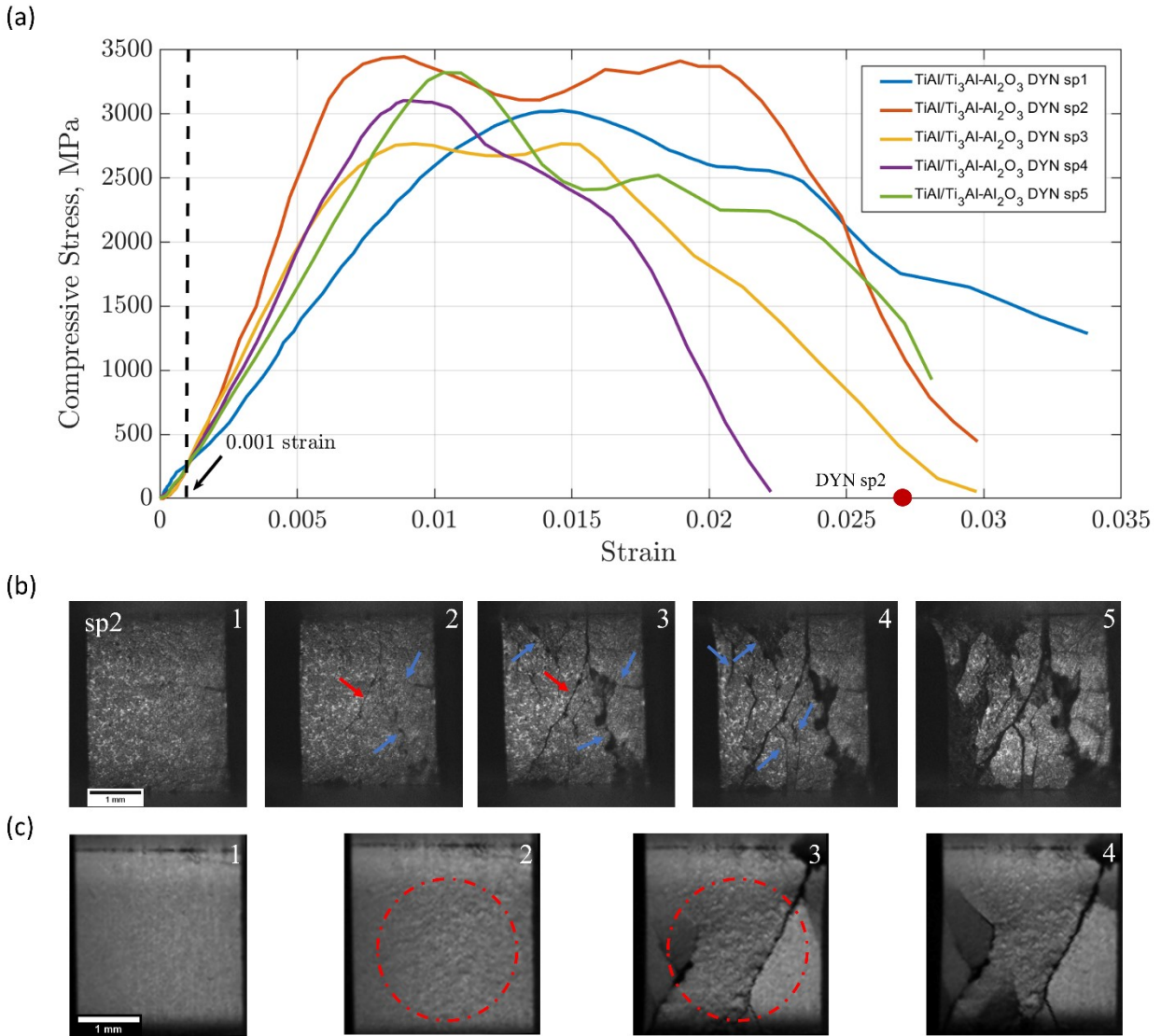


Figure 4.5: (a) Stress-strain curves for dynamic uniaxial compression tests. The $x = 0.1\%$ strain line indicates where the stiffnesses are computed for each curve; (b) A sequence of still images of sample DYN sp2 showing typical post-peak fracture paths of the cermet under dynamic loading. The red dot shown on the x-axis in (a) indicates the starting point of when the images are extracted. The red arrows in the images in (b) show a primary split crack along the loading direction, and the blue arrows show crack branching from the primary cracks, as well as cracks activated during further loading; (c) A sequence of representative still images taken from the tests using unpainted specimen to reveal the surface deformation features. The red circle highlights where the texturing is observed on the specimen surface. Splitting and branching cracks are also identified that are similar to (b).

4.2 Summary of the compressive strength at different strain rates

Shown in Figure 4.6 is the summary of the compressive strength (taken as the peak stresses) plotted against strain rate for the TiAl/Ti₃Al-Al₂O₃ cermet. As mentioned, the quasi-static compressive

strength has an average of 2780 ± 60 MPa at an average strain rate of $2 \times 10^{-4} \text{ s}^{-1}$. In all eight dynamic experiments (including the five experiments plotted in Figure 4.5 and three unplotted), the compressive strength is between 3000 MPa and 3800 MPa with an average of 3410 ± 247 MPa, with strain rates between $1 \times 10^3 \text{ s}^{-1}$ and $2 \times 10^3 \text{ s}^{-1}$. On average, the compressive strength increases approximately 1.3 times as the strain rates increases from $\sim 10^{-4} \text{ s}^{-1}$ to $\sim 10^3 \text{ s}^{-1}$. Notable is the increase in variability of the strengths for the higher strain rate, and the apparent high rate sensitivity at the higher strain rates.

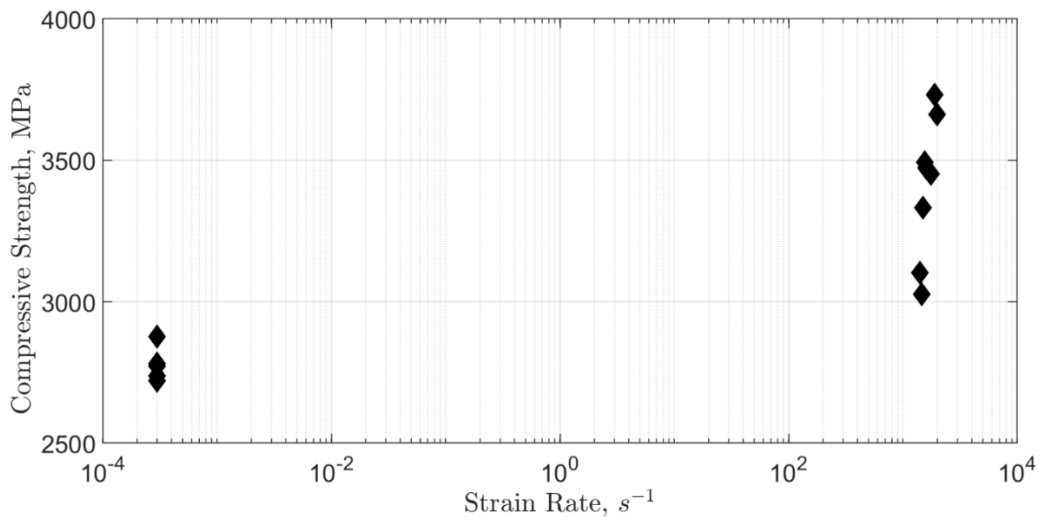


Figure 4.6: Semi-log plot of the uniaxial compressive strength of the TiAl/Ti₃Al-Al₂O₃ cermet as a function of the strain rate. The dynamic compressive strength is approximately 1.3 times the quasi-static compressive strength with an seven order increase in strain rate (from $\sim 10^{-4} \text{ s}^{-1}$ to $\sim 10^3 \text{ s}^{-1}$). In addition, the material appears to be more rate sensitive at high strain rates.

4.3 Microscopic diagnosis

4.3.1 Micro/nanoscale failure mechanisms under quasi-static uniaxial compression

Fractography studies have been carried out on the fragments retrieved from both loading conditions using SEM and TEM to determine the rate-dependent failure mechanisms of the TiAl/Ti₃Al-Al₂O₃ cermet. Shown in Figure 4.7a – c is a set of representative micrographs taken of the fractured surfaces recovered from the quasi-static tests. Shown in Figure 4.7-a is the global

FESEM image of a fracture surface showing a microcrack developed in the vicinity of the primary axial crack, where the yellow arrows indicate the direction of compressive loading. It is observed that the crack propagates through the darker phase (titanium aluminide) and passes along the boundary of the brighter particles (alumina, indicated by blue arrows). This is referred to as intergranular fracture in some of the literature on the fracture mechanisms of cermets (e.g., Kaplan et al. [4.57]), where cracking happens in the binding matrix (titanium aluminide in this study). Small amounts of cleavages are observed near the cracks on the darker phase (indicated by blue arrows), which is an additional proof of brittle fracture in the material. It is observed that there is a minimal amount of transgranular fracture (cracking through the alumina particles) under quasi-static compressive loading, and this has been validated by investigating eight locations in five typical fragments recovered from the quasi-static tests. Figure 4.7-b shows a magnified view of a fracture surface which demonstrates interfacial fracture, particle debonding, and dimpling being activated during quasi-static loading (indicated by white arrows). The red arrows indicate some typical post-deforming features that are created by these mechanisms. It is observed that grain boundary delamination and particle pull-out are two major phenomena appearing on the quasi-static fracture surface, and these have been seen at a significant scale on all fragments. Distinct cleavage facets (indicated by a white arrow in Fig. 4.7-b) are observed inside the holes where the particles are being pulled out. These cleavage facets are believed to be formed mainly via interfacial debonding. These cleavages can be differentiated from the lamellar-shaped pattern appearing in the matrix by the wave pattern that is formed inside the craters. Ductile dimples are also observed inside the darker phase, but not in a significant amount. Additionally, the grain boundaries between particles seem to remain intact, and minimal delamination at the particle boundaries are observed throughout all the fragments. Figure 4.7-c demonstrates a triple junction

region (indicated by a red arrow) formed by branched cracks, and similar mechanisms such as grain boundary delamination and particle pull-out are observed in the vicinity of the cracks. It is also observed that the cracks propagate by tracing the particle boundaries along the crack path, where no particle-particle interfaces are interrupted by the cracking.

Due to the uneven nature of the fracture surface in Figure 4.7-c, contrast is not enough to identify cracking from either the alumina phase or the equiaxed gamma titanium aluminide phase. In order to verify the observation of intergranular cracking, EDS is applied to identify the relevant phases from elemental mapping. Figures 7-d to f show the corresponding elemental maps of Figure 4.7-c, where the major elements Al, O, and Ti are mapped to investigate the phases along the cracks and at the triple junctions. The brighter intensities correspond to higher relative concentrations. Shown in Figure 4.7-d is the EDS map of aluminum. This element appears in all TiAl, Ti₃Al, and Al₂O₃ in the cermet being investigated, with higher concentration in the alumina phase. A clear crack path in the Al map corresponding to the SEM image can be identified in Figure 4.7-d (indicated by a yellow arrow), with higher concentrations reflected on the particles along the path, which indicates a high possibility of an alumina phase. The region at the triple junction (indicated by a blue arrow) exhibits a lower amount of Al, which may correlate to either the TiAl or Ti₃Al phase. This can be further clarified with the O map shown in Figure 4.7-e. It is observed that the particles that have a higher concentration of Al correspond to regions with a higher concentration of O, and these are likely the ($\gamma + \alpha_2$) titanium aluminide lamellae. The regions at the triple junction contain no detectable oxygen, and these are likely the γ -TiAl phase. The Ti map shown in Figure 4.7-f does not reveal the crack path clearly because of the high electron absorption rate of titanium. By superimposing the crack position with the map, the regions with high concentrations of Al and O correspond to regions with no concentration of Ti, and the regions at the triple junction contain

a high concentration of the Ti element. In addition, a trace amount of oxygen is detected at the regions where titanium exists, and this is the ($\gamma + \alpha_2$) lamellar structure due to the higher oxygen precipitation at the interfaces [4.33]. Combining these observations, we conclude that the intergranular fracture happens within the titanium aluminide phase (possibly in both γ -TiAl and α_2 -Ti₃Al), and the region at the triple junction is covered with equiaxed γ -TiAl grains.

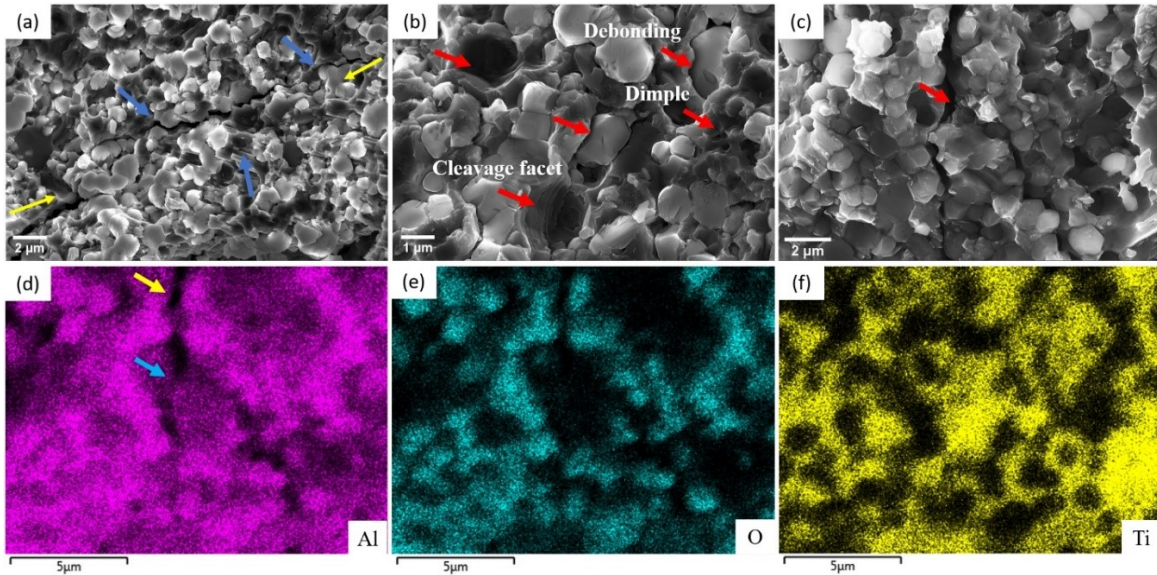


Figure 4.7: Micrographs taken on the fracture surface showing the fractography of the TiAl/Ti₃Al-Al₂O₃ cermet under quasi-static uniaxial compression. (a) A global view of the crack propagation, where the yellow arrows indicate the compressive loading direction, and the blue arrows indicate the intergranular fracture in the titanium aluminide matrix and cleavage in the titanium aluminide lamellar planes; (b) A magnified view in the vicinity of the crack in (a) showing typical deformation mechanisms, including grain boundary delamination, particle pull-out, and dimpling; (c – f) FESEM image with the corresponding EDS maps showing the phases where the intergranular fracture happens. (c) FESEM micrograph showing an intergranular crack passing through the field of view, where a triple junction is formed; (d) Distribution of the Al element in the FESEM image; (e) Distribution of the O element in the FESEM image; (f) Distribution of the Ti element in the FESEM image. In each EDS map, a brighter color indicates a higher concentration of such element.

4.3.2 Micro/nanoscale failure mechanisms under dynamic uniaxial compression

In this section, fractography studies are conducted on the TiAl/Ti₃Al-Al₂O₃ cermet fragments recovered from the dynamic experiments. Both fracture surfaces and polished fracture surfaces are investigated to determine failure mechanisms and compare with the quasi-static test results. Shown in Figure 4.8a – b is a set of FESEM micrographs taken of polished fracture surfaces that are used

to probe the sub-surface damage mechanisms. In Figure 4.8-a, a microcrack propagates through the field of view from the top to the bottom of the image (pointed out by a white arrow), with the darker phase being alumina. It is observed that the crack passes both along and through the alumina phase, where a combination of intergranular and transgranular cracking are observed to occur simultaneously under dynamic loading. Voids are also observed in the crack path, and it appears as though there are some void growth and coalescence ahead of the crack tip. In addition, extensive particle fracture and particle-particle interface fracture are observed around the microcrack (indicated by red arrows). Some of the fractures occurring within a cluster of alumina particles remain in the particles and do not propagate further into the matrix. Different from what is observed in the quasi-static case, it is believed that transgranular cracking is one of the dominant failure mechanisms under dynamic loading. Figure 4.8-b investigates the density of the void growth (shown as dark color) under dynamic loading by using a larger scale field of view. The areal fraction of the voids constitutes $\sim 4\%$ of the image, for which void growth is observed across all polished fragment surfaces being investigated with a heterogeneous distribution. The areal fraction of voids is approximately twice as much as that are computed in the as-received material (see Fig. 4.1-a). It is also noted that the voids tend to grow within or surrounding the alumina phase. This extensive void growth and particle cracking are not observed on the polished fracture surface under quasi-static loading, and so is believed to be unique for the dynamic experiments.

Figure 4.8-c and d show FESEM micrographs taken on the fracture surfaces of the dynamic fragments. Shown in Figure 4.8-c is a typical fracture plane observed under dynamic compressive loading. Extensive cleavages are identified in the titanium aluminide phase compared to the quasi-static case (see Fig. 4.7-a), which is believed to correspond to the lamellar tearing in the $(\gamma + \alpha_2)$ lamellar plane. In addition, a significant amount of ductile dimpling is observed on the fracture

plane. In Figure 4.8-d, a magnified view is used to probe different fracture mechanisms activated under dynamic loading. It is observed that three types of the fracture mechanisms can exist concurrently in a single microcrack: 1. intergranular fracture; 2. matrix fracture; and 3. particle fracture. This supports the extensive particle fractures and inter/transgranular cracking observed in Figure 4.8-a on the polished fragment surface.

Shown in Figure 4.8-e is an image of a microcrack that propagates through the field of view from left to right with the corresponding aluminum elemental map (Fig. 4.8-f). Pointed out by the red arrow is a site where high concentrations of Al are present on the upper side of the crack, while lower concentrations of Al are present on the lower side of the crack. It is suggested that intergranular cracking occurs along an alumina particle (upper side) and through the titanium aluminide matrix (lower side). No evidence of transgranular cracking can be found on fracture planes like this, and this is expected because typically lower energy is needed for a particle to delaminate from the matrix rather than for it to fracture. In addition, a hole formed from particle pull-out (see Fig. 4.8-e) is identified within the fractured titanium aluminide plane to supplement the observation.

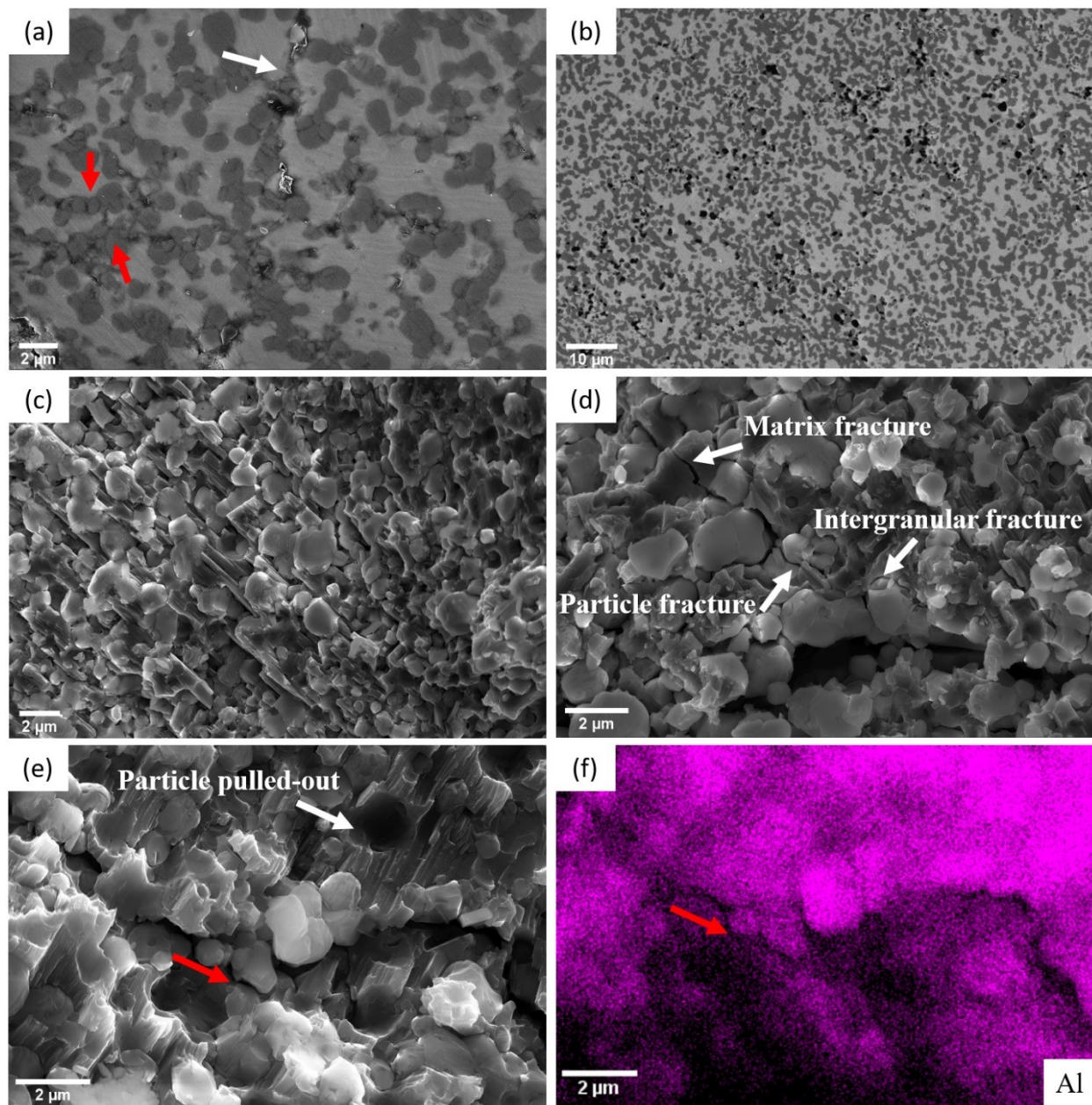


Figure 4.8: Micrographs showing the fractography of the TiAl/Ti₃Al-Al₂O₃ cermet under dynamic uniaxial compression. (a – b) FESEM images taken on the polished fracture surface revealing the sub-surface damage of the cermet. (a) Extensive particle fracture and particle interface fracture are observed in the alumina phase (phase with darker color), and a crack (indicated by a white arrow) propagates along and through the alumina particles with void growth identified on the crack path; (b) A global view of the sub-surface damage on the polished fracture surface showing the density of the void growth (shown as dark color) under dynamic compressive loading. (c – e) FESEM images taken on the fracture surface showing different deformation mechanisms activated in the material. (c) A typical fracture plane under dynamic loading showing extensive amounts of cleavage in the titanium aluminide matrix; (d) A magnified view on three of the major fracture sites in the material, including particle fracture, matrix fracture, and intergranular fracture; (e) A microcrack propagates through the field of view horizontally with (f) the corresponding Al element map to identify the phases along the crack. Particle pull-out is also observed on the fracture surface in (e).

Next, the microstructural evolution of the TiAl/Ti₃Al-Al₂O₃ cermet under dynamic uniaxial compressive loads are probed by using TEM coupled with SAED and EDS. Shown in Figure 4.9-a is a bright field TEM micrograph showing a global view of the postmortem microstructure. The brighter regions in the micrograph are the alumina clusters, and the darker regions surrounding the clusters are the titanium aluminide phases. The empty spaces represent the pores already existing in the as-received material or voids induced by grain boundary delamination from loading (note the void growth observed in Fig. 4.8-b). It is observed that the titanium aluminide phase exhibits a globally lamellar structure, with an orientation approximately 30° with respect to the horizontal plane (indicated by the red arrow). The difference in grayscale color between the lamellar structures suggests the activation of different deformation mechanisms, which will be discussed in Figure 4.10. Figure 4.9-b shows the corresponding SAED pattern taken at the circled location in Figure 4.9-a, and the crystalline planes are indexed from the diffracting patterns taken at that location. Two phases are identified from the SAED analysis, termed the γ -TiAl and α_2 -Ti₃Al phases, and they appear as alternating γ and α_2 titanium aluminide lamellae (denoted as γ/α_2 lamellae). This alternating pattern is confirmed by the lines (orientation specified) formed from the diffracting “dots” with alternating sizes in Figure 4.9-b.

Figure 4.9-c to Figure 4.9-e confirm the observation in Figure 4.9-b by providing a magnified view of the γ/α_2 lamellae with corresponding EDS maps showing the compositions of the individual lamella. Figure 4.9-c is a bright field TEM micrograph focused at the alumina-titanium aluminide phase boundary, where the phase boundary is outlined by dashed lines in the figure. The alumina phase appears as black on the right hand side, whereas the γ/α_2 lamellar structure appears as white or gray on the left. It is observed from the Al elemental map (see Fig. 4.9-d) that higher concentrations of Al element correspond to the gray lamellae in Figure 4.9-c, and lower

concentrations of Al element correspond to the white lamellae in Figure 4.9-c. In addition, higher concentrations of the Ti element in Figure 4.9-e corresponds to the white lamellae in Figure 4.9-c, and lower concentrations of Ti in Figure 4.9-e corresponds to the gray lamellae in Figure 4.9-c. Taken together, all of the evidence suggests that the white lamellae in Figure 4.9-c are the α_2 -Ti₃Al phase, where higher relative concentration of Ti and lower relative concentration of Al are shown. Consequently, the gray lamellae in Figure 4.9-c are the γ -TiAl phase, where lower relative concentration of Ti and higher relative concentration of Al are revealed. Large variations of the lamella width are observed. The γ lamella width is between 10 nm to 80 nm with an average of 35 ± 19 nm, and the α_2 lamella width are between 5 nm to 60 nm with an average of 31 ± 21 nm. Lamella width is defined by drawing a line perpendicular to the lamella boundaries (indicated by the double arrow in Fig. 4.9-c), and these measurements are averaged over at least 15 locations for each phase. Shown in Figure 4.9-f is a high-resolution TEM image demonstrating the lattice structure of an adjacent pair of γ/α_2 lamellae. The lamellar boundary is indicated by the dashed red lines. The γ lattice exhibits a structure similar to an elongated rectangle, whereas the α_2 lattice shows a structure surface similar to a square. This is justified from studying the crystalline structure of the γ -TiAl and α_2 -Ti₃Al, for which they have an ordered face-centered tetragonal L1₀ structure and an ordered hexagonal DO₁₉ structure, respectively [4.58]. Thus, it is concluded that the microstructure of the titanium aluminide phase of the current cermet has evolved from a duplex structure (see Fig. 4.1-c) to a fully lamellar structure with alternating γ/α_2 lamellae under dynamic compressive loading.

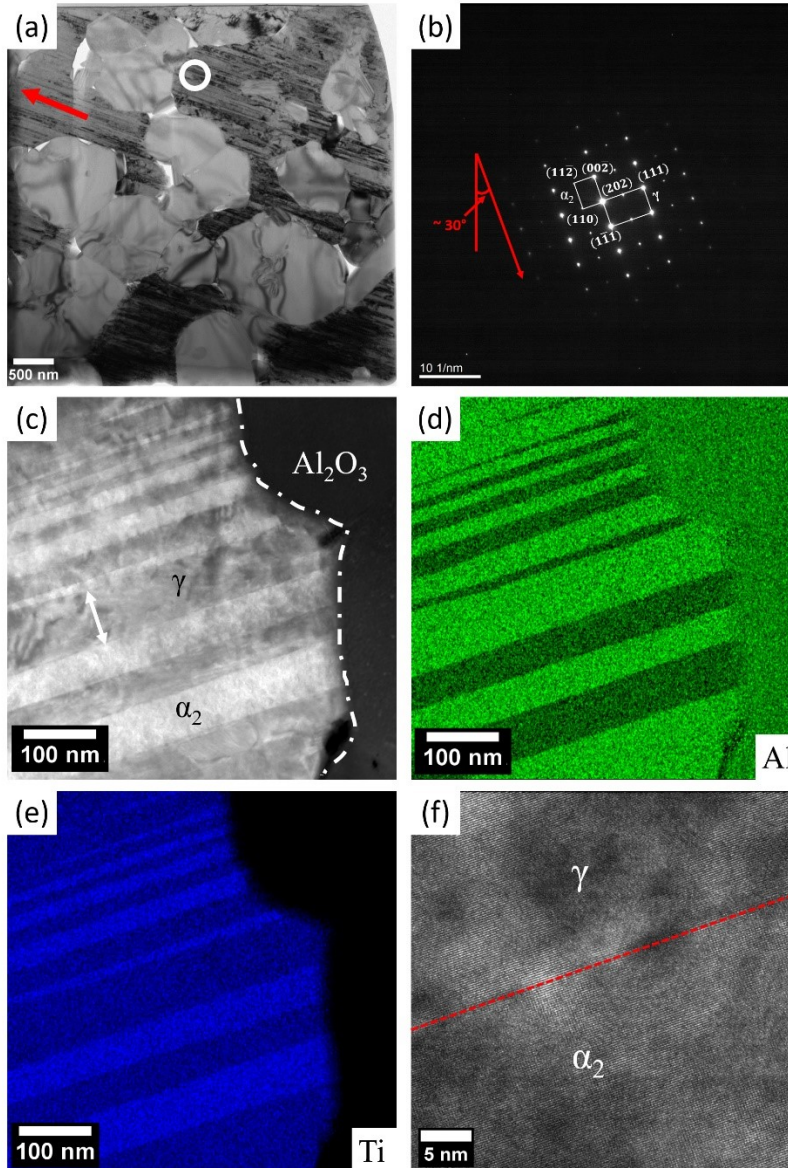


Figure 4.9: TEM micrographs showing microstructure evolution under dynamic uniaxial compressive loads. (a) A global view of the TEM lamella showing the alumina clusters (lighter regions) and the titanium aluminide lamellae (darker regions). The orientation of the titanium aluminide lamellae (red arrow) is approximately 30° with respect to the horizontal plane. (b) SAED pattern corresponding to the circled region in (a) identifying the presence of γ and α_2 lamellae. The orientation is specified in the figure, and it corresponds to the lamellar orientation in (a). (c – e) Bright field TEM on the alumina-titanium aluminide boundary and the corresponding EDS maps showing the lamellae compositions. The alumina-titanium aluminide boundary is identified by dashed lines in (c). In each EDS map, a brighter color indicates a higher concentration of the corresponding element. (f) High-resolution TEM showing crystalline lattice structure of an adjacent γ/α_2 lamellae. The grain boundary is indicated by a dashed red line.

Finally, the nanoscale deformation mechanisms of the TiAl/Ti₃Al-Al₂O₃ cermet under dynamic uniaxial compressive loads are investigated. Shown in Figure 4.10 are the bright field and high-

resolution TEM micrographs that demonstrate different deformation mechanisms activated in the alumina phase, at the alumina-titanium aluminide phase boundary, and between the γ/α_2 lamellae. In Figure 4.10-a, residual stress is observed across all alumina clusters, and they are manifested as the dark contour lines connecting the grain boundaries. This residual stress could be the consequence of manufacturing process (also seen in the as-received material in Fig. 4.1-c) or high pressure loading. Dislocations (indicated by white arrows) are observed on the alumina grains, and they appear to be initiated either from the grain boundary or from the residual stress contour lines. It is observed that these dislocations are often localized features, where they do not pileup and distribute evenly across the alumina clusters. A microcrack (indicated by a red arrow) is observed to initiate at the tip of a dislocation and propagate through the alumina grain, and it is arrested at the alumina-titanium aluminide boundary. No twinning is observed on any part of the investigated alumina phase, and most of the grains are free of plastic deformation. In Figure 4.10-b, nano-twins (indicated by yellow arrows) are observed at the lamellar boundaries in the titanium aluminide phase. The twinning is identified by the periodic pattern of the structure as well as their orientation reference to the γ/α_2 lamellae. The twin boundary structures and their corresponding planes are omitted here because of the difficulties in determining the orientation of the fragments with respect to the deformation axis, which are recovered after an explosive failure under dynamic loading. These nano-twins appear to be connected at the lamellar boundaries and formed curved surfaces that extend into the adjacent lamellae. In addition, alumina-titanium aluminide grain boundary delamination is observed, where a microcrack is formed and propagates along the boundary. Shown in Figure 4.10-c is a bright field TEM image focused on the dislocations in between the γ/α_2 lamellae. Three dislocation phenomena are observed and indicated in the figure: 1. Dislocation tangling, which usually occurs in the middle of the lamella (in this case in the γ phase), appears as

a dark cloud of randomly-orientated dislocations [4.59]; 2. Dislocation network that also occurs in between the lamella. The dislocations are crossing and interconnected with each other to form a meshed structure [4.60]; 3. Dislocation wall that appears as black dots accumulated together and occurs at the boundary of the lamella [4.59]. Unlike the localized dislocation regions in the alumina grains, these dislocation features are shown as global plastic deformation in the titanium aluminide phase (see Fig. 4.9-a). In addition, twin boundaries (indicated by yellow dashed lines) are pointed out in one of the γ lamella. Lastly, shown in Figure 4.10-d is a high-resolution TEM micrograph looking at the alumina-titanium aluminide boundary. Phases are identified in the figure. Dislocation pileups are observed at the location, which have characteristics similar to the dislocation wall. After careful examinations, it is concluded that most of the nanoscale plastic deformation mechanisms take place in the titanium aluminide phase under uniaxial compression for strain rates between 1000 s^{-1} and 2000 s^{-1} .

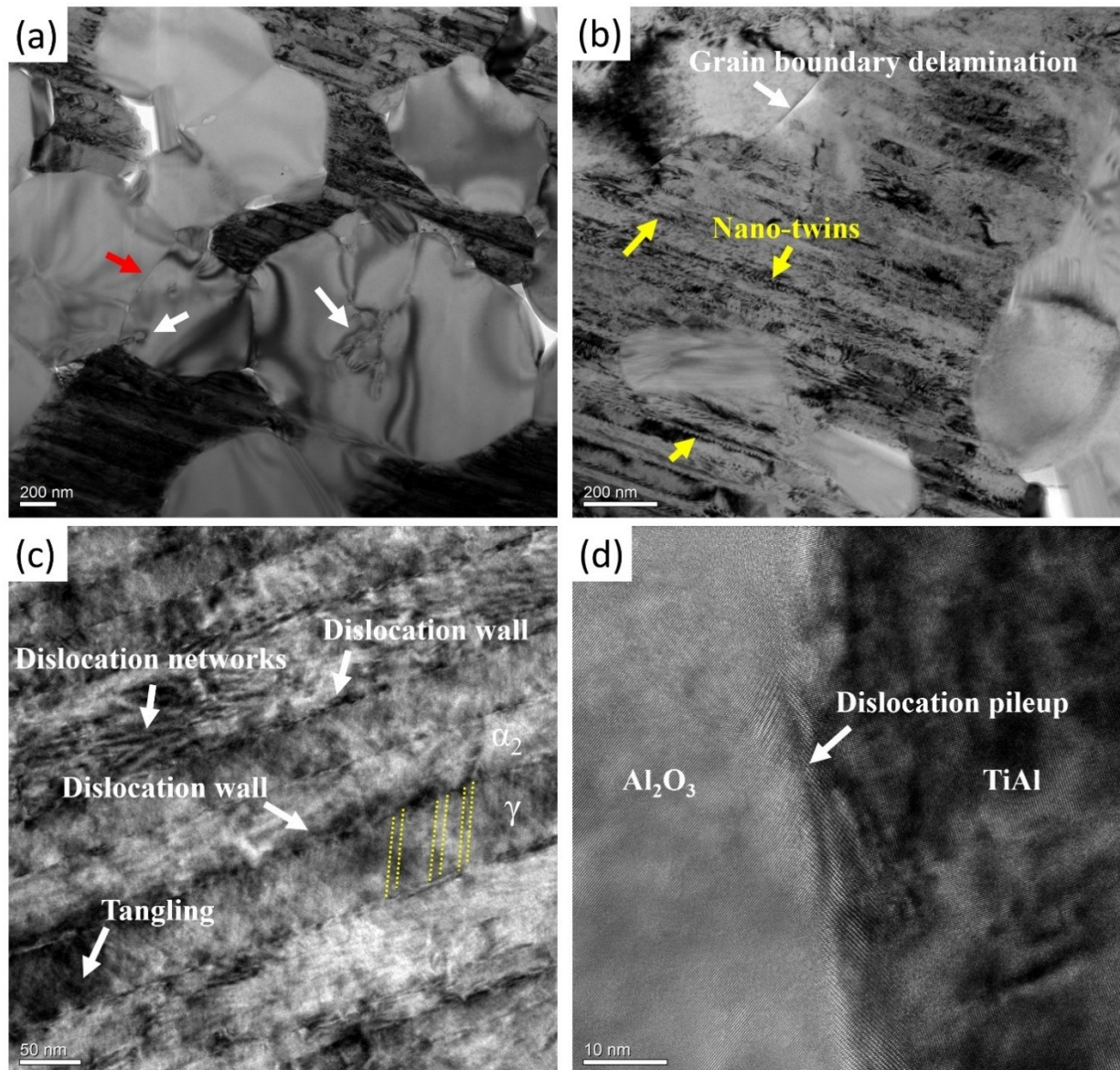


Figure 4.10: Bright field TEM micrograph showing the deformation mechanisms activated under dynamic uniaxial compressive loads. (a) Residual stress (appeared as dark contour lines) and dislocations (indicated by white arrows) are observed on the alumina grains. A microcrack (indicated by a red arrow) is initiated from the dislocation tip and propagate through the alumina grain. (b) Delamination occurs at the alumina-titanium aluminide grain boundary. Nano-twins (indicated by yellow arrows) are observed crossing the titanium aluminide lamellar boundaries and forming periodic curved structures. (c) Different types of dislocation activities, including dislocation walls, networks, and tangling are observed within titanium aluminide lamellae and at the lamellar boundaries. (d) High-resolution TEM micrograph showing dislocation pileup at the alumina-titanium aluminide grain boundary.

4.4 X-ray diffraction

Two-dimensional x-ray diffraction is applied as a way to examine possible phase changes and crystalline texturing evolution in the TiAl/Ti₃Al-Al₂O₃ cermet before and after experimentation. Shown in Figure 4.11-a is the $\theta - 2\theta$ equivalent spectrum plot for the as-received material, and of fragments taken after quasi-static and dynamic experiments. In this case, the spectrum plot of the as-received material is used as a reference to compare with the spectrums of both post-deformation frames from the quasi-static and dynamic tests. The major peaks corresponding to the three phases (i.e., γ -TiAl, α_2 -Ti₃Al, and Al₂O₃) are identified on the spectrum, and the corresponding plane related to each peak is labeled adjacent to the peak. On the spectrum of the quasi-static fragment, no additional peak is observed, and no phase change occurs under quasi-static loading. An amorphous peak is observed between 10° and 20° in the spectrum of the dynamic fragment, and it is superimposed with the first α_2 -Ti₃Al peak in the pristine material at around 17°. No such phenomenon is observed under quasi-static loading, and no additional phase changes occur (in terms of additional or vanishing peaks) in the material under dynamic loading. Note that amorphization occurs in other materials under specific conditions, usually under decompression from an extremely high pressure (e.g., B4C under shock wave loading [4.61]). In this case, even though amorphization did occur in the TiAl alloys under high pressure torsion [4.62], we do not believe the stress level in our experiments is sufficient for a pressure-induced type of amorphization to occur. The specific reason for the amorphous behavior needs to be further examined in future studies. Lastly, the absence of phase change is confirmed by checking the phase ratio of each phase (i.e., γ -TiAl, α_2 -Ti₃Al, and Al₂O₃), for which all peak intensities corresponding to each phase are normalized by the highest peak of that phase. In total, two sets of samples are scanned to ensure the repeatability of the results.

Next, shown in Figure 4.11-b is the two-dimensional diffraction frames revealing the crystalline texturing evolution of the: as-received materials (top), and of a polished fracture surface taken from a quasi-static test (middle), and a dynamic test (bottom). In the frame of the as-received material (top frame), all arcs are mostly solid, which indicates all γ -TiAl, α_2 -Ti₃Al, and Al₂O₃ phases are in a randomly-orientated polycrystalline form (no preferred crystallographic orientation). The brightest contour line, which corresponds to the highest peak in Figure 4.11-a, is a superimposed peak consisting of both γ -TiAl and α_2 -Ti₃Al. It is observed that this superimposed titanium aluminide phase is in its randomly orientated state in the as-received material. In the frame of the quasi-static fragment, some degrees of crystalline texturing occur, and this is manifested as changes from solid arcs to mildly dashed arcs in the middle figure. In the quasi-static fragment, it is observed that all arcs corresponding to both γ -TiAl and α_2 -Ti₃Al phases transform from their random polycrystalline structure to a crystalline textured structure (as indicated by the dashed arcs), whereas the alumina phase remains in its randomly orientated form (as indicated by the solid arcs). Similarly, the crystalline texturing of the titanium aluminide phase keeps evolving and becomes more textured (and less random) in the dynamic fragment (see Fig. 4.11-c). Less preferred crystallographic planes are observed, and this is shown as the decreasing number of the dashed arcs in the 2D frame. For the dynamic experiment, the alumina phase remains in its randomly orientated polycrystalline structure under dynamic loading.

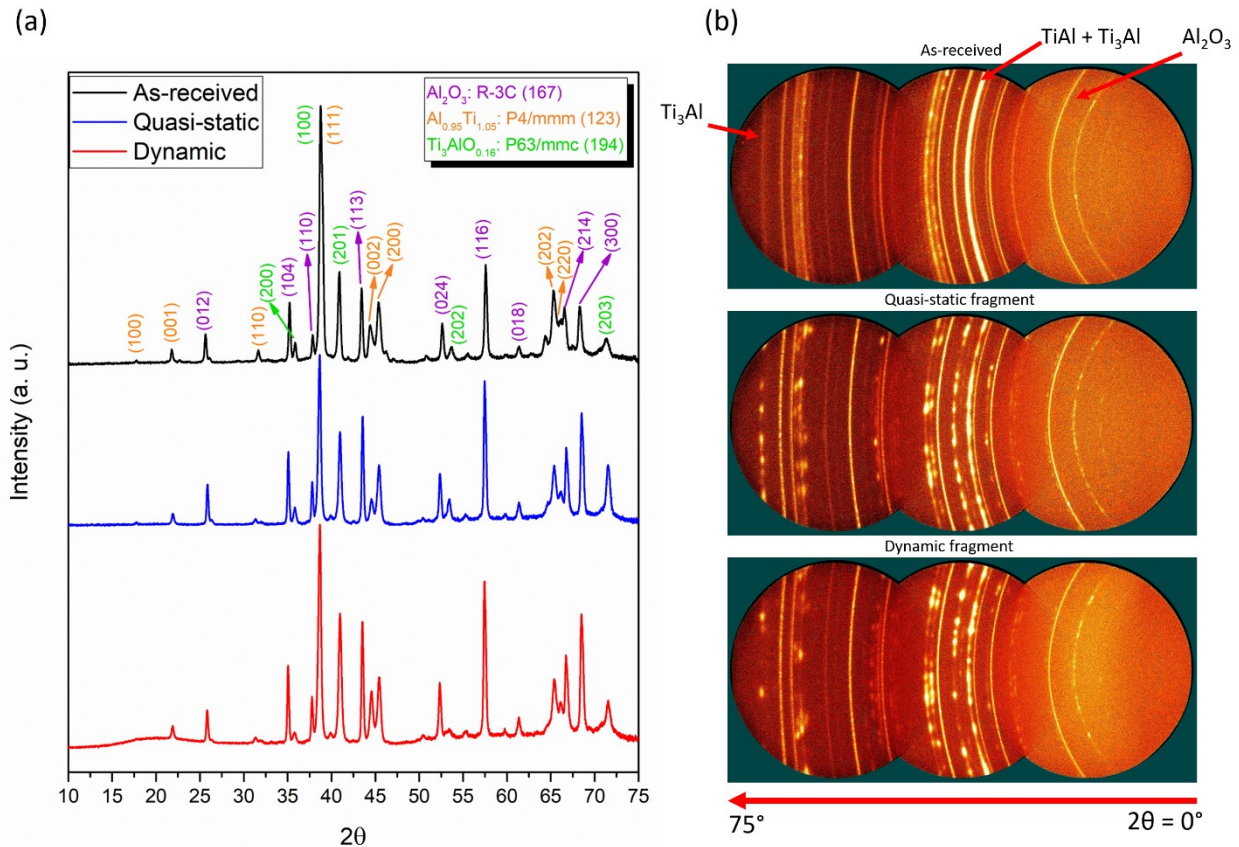


Figure 4.11: X-ray diffraction analysis of the as-received TiAl/Ti₃Al-Al₂O₃ cermet, and of a polished fracture surface taken from a quasi-static fragment and a dynamic fragment showing phases changes and crystallinity evolution during uniaxial compressive loading at different strain rates. (a) $\theta - 2\theta$ equivalent spectrum plots showing an amorphous peak occurs in the dynamic fragment, where no additional phase changes occur under both quasi-static and dynamic loading; (b) 2D diffraction frame revealing crystalline texturing evolves at different loading rates. The light intensity is integrated from right to left to obtain the 1-D spectrums. Typical peaks corresponding to the three phases are pointed out by red arrows to show the texturing evolution in different phases. Significant crystalline texturing is observed in the dynamic fragment on both γ -TiAl and α_2 -Ti₃Al phases, whereas alumina phase remains in its randomly orientated polycrystalline structure.

5. Discussion

This paper explores the rate-dependent stress-strain responses, material properties, failure mechanisms, and crystalline texture evolution of a SHS fabricated TiAl/Ti₃Al-Al₂O₃ cermet under both quasi-static and dynamic uniaxial compression. First, mechanical tests were performed using a conventional MTS machine and modified split Hopkinson pressure bar, and novel digital image correlation was used to extract the strain data to obtain the stress-strain curves. Next, microscopic

diagnosis using SEM with EDS and TEM, and 2D-XRD were used to investigate the failure mechanisms and crystalline texturing behavior of the material observed as a consequence of mechanical loading and associated deformation. The current work builds on the framework of former WC-Co, SiC-Ti, SiC-Al, B₄C-Al, TiB₂-Al, and TiC-Steel cermet systems [4.5, 4.9, 4.11, 4.17, 4.46, 4.64 – 4.67] by studying the rate-dependency of material responses of these materials, as well as extends to the TiAl/Ti₃Al-Al₂O₃ cermet oxide cermet where studies have mainly focus on fabrication methods [4.28 – 4.33]. In the first sub-section of the discussion, critical observations on the rate-dependency of material properties of our cermet will be highlighted, and these values will be compared with other cermet systems. In the second sub-section of the discussion, a rate-dependency exponent and a transition strain rate of the studied TiAl/Ti₃Al-Al₂O₃ cermet will be postulated based on the compressive strength results. In this sub-section, the rate sensitivity will also be discussed based on the flow stress. In the third sub-section of the discussion, rate-dependent micro/nanoscale failure mechanisms and crystalline texturing behavior will be assessed in the current material and compared with other cermet systems. In the last sub-section of the discussion, material implications on protection applications will be emphasized based on the relevant ballistic performance metrics currently used in impact testing.

5.1 Comparing stress-strain responses to those of other cermet systems

In this sub-section, the rate-dependent stress-strain responses of the TiAl/Ti₃Al-Al₂O₃ cermet will be discussed with respect to stiffness and failure strains, and these will be emphasized by comparing to other cermet systems (e.g., SiC-Al [4.47], TiC-steel [4.67]). The strength values will be compared in the next sub-section of the Discussion. At the low and high strain rate loading, the stress-strain curves exhibit an initial linear elastic portion. In the quasi-static case (see Fig. 4.4), the stress increases linearly to ~ 0.002 , whereas the stress increases linearly up to approximately

0.008 under dynamic loading. In the current cermet, the stiffness has an average of 267 ± 28 GPa and 255 ± 11 GPa under quasi-static and dynamic loading, respectively. First, it is observed that the offset of the linear elastic region of the dynamic stress-strain response increases from the quasi-static case by ~ 0.006 (from ~ 0.002 to ~ 0.008) in strain. In linear elastically behaving materials like ceramics, microcrack initiation, growth, and coalescence is considered the dominant failure mechanism [4.68]. This extended linear elastic regime of the TiAl/Ti₃Al-Al₂O₃ cermet under dynamic loading is attributed to the limited velocity of crack growth compared to the high strain rates [4.69]. In a linear elastic material with a certain stiffness, this essentially means an increase in strength and failure strain for higher strain rates when compared to quasi-static behavior [4.69, 4.70]. Second, no clear rate-dependency of the stiffness is observed in the present study. This agrees with most of the works being done on cermets, where stiffness was often reported as one of the rate insensitive properties of a material (e.g., ~ 78 GPa for a 40 vol% SiC_p-2024 Al cermet and ~ 135 GPa for a 50 vol% SiC_p-2024 Al cermet from quasi-static to 2500 s^{-1} strain rate [4.47], ~ 360 GPa for a group of TiC-steel cermets from quasi-static to plate impact tests [4.67], ~ 25 GPa for a 35 vol% Al₂O₃-Mg cermet from 10^{-4} s^{-1} to 1550 s^{-1} strain rate [4.71], and ~ 50 GPa for a B₄C-Al cermet from 10^{-3} s^{-1} to 2250 s^{-1} strain rate [4.72]). In contrast, the stress-strain curves reported by Zhu et al. [4.66] revealed a much higher stiffness (~ 13 GPa at 0.0007 s^{-1} strain rate and ~ 60 GPa at 1100 s^{-1} strain rate) in the TiB₂-Al cermet. The reasons behind possible rate-dependency on stiffness is not yet well understood. It is worth noting that some stiffness values measured in these literature are lower than their respective constituents, and this might be related to the challenges in measuring small strains under compression. We overcome this in this study by using high resolution cameras coupled to specialized DIC techniques.

After the initial linear portion, significant differences in the compressive stress-strain behavior of the TiAl/Ti₃Al-Al₂O₃ cermet are observed (see Fig. 4.4 and 4.5). In the quasi-static tests (Fig. 4.4), continuous concave-shaped stress-strain curves are obtained. Unlike the case for typical titanium aluminide alloys [4.73 – 4.75], no distinct yield point is observed in these curves. The concave shape indicates a continuous degradation of instantaneous stiffness during loading, and this can be attributed to the “softening” behavior and damage accumulation in the material [4.2]. Sudden catastrophic failure occurs after the peak stress is reached, and the material loses its load bearing capacity. Overall, the material behaves consistently under quasi-static compression in terms of strength deviation (with a standard deviation of 60 MPa), as well as trends in the curves. In the dynamic tests (Fig. 4.5), the material behaves in a much more complex manner compared to the quasi-static case. In general, each stress-strain curve consists of at least two peaks, where the first peak has the highest stress value among all tests. Between two subsequent peaks, stress relaxation (flow softening) followed by strain hardening is observed. Some literature on metallic alloys under high-rate loadings explain this alternating stress phenomenon as “alternating thermal softening and strain hardening” (e.g., 7003-T4 aluminum alloy under high strain rate impact [4.76]). However, it is challenging to claim thermal effects in the current study without in-situ measurements. The rate-dependency in stress-strain behavior under different loading rates have been probed in other cermet systems, emphasizing the stress behavior after the initial linear portion. For example, Guden et al. [4.71] investigated the rate-dependent stress-strain response of a Mg-Al₂O₃ cermet and found distinct differences in stress-strain responses before failure, where the “flow softening-hardening” phenomenon observed in our cermet was also observed under dynamic loading in their study. In addition, both Rittel et al. [4.17] and Zhu et al. [4.66] found the alternating strain hardening and softening phenomena under dynamic loading of a TiC-steel and a TiB₂-Al cermet,

respectively, where both of their materials behave in a near-linear elastic manner under quasi-static loading [4.67]. In their studies, the changes in the stress-strain responses were attributed to either changes in failure mechanisms or the activation of additional microstructural changes during high-rate impact [4.66, 4.67]. In the current study, the failure mechanisms and crystalline texture evolution are believed to be responsible for the changes in the stress-strain response of the TiAl/Ti₃Al-Al₂O₃ cermet, and these will be discussed in detail in sub-section 5.3.

Next, we compare the failure strains (as the final point on the stress-strain curves before the onset of cracking) of the current cermet to ceramics and other cermet systems. The failure strain of the TiAl/Ti₃Al-Al₂O₃ cermet measured in quasi-static tests has an average of 0.0166 ± 0.0017 , whereas the failure strain measured in dynamic tests has an average of 0.026 ± 0.0032 . An approximately 1.4 times increase is observed with a seven order increase in strain rate. The failure strains of the current cermet are much higher than most of the advanced ceramics under both loading rates (i.e., between 1.0% to 1.5% for Al₂O₃ [4.77 – 4.79] and reported as 1.29% for SiC and 0.62% for Si₃N₄ [4.80]). Furthermore, the failure strain of the TiAl/Ti₃Al-Al₂O₃ cermet is at the higher end among some cermet systems, such as WC-Co systems ($\sim 2\%$ quasi-statically for 85% WC [4.15]), TiC-Ni systems ($\sim 1.2\%$ quasi-statically for 70% TiC [4.16]), and B₄C-Al systems ($\sim 1.6\%$ at 0.005 s^{-1} and $\sim 3\%$ at 2000 s^{-1} for 65% B₄C [4.81]). Note that the volume percentage of the ceramic phases in these cermets are all sufficiently high ($> 60\%$). At the same time, some cermet systems with aluminum (e.g., 2024Al-TiB₂) and steel (e.g., 1080 steel-TiC) as the matrix material could reach failure strains of around 10% [4.17, 4.47, 4.66]. Altogether, this measurement of the rate-dependent failure strains may give us some knowledge on the improvement in dynamic fracture toughness, which could be an important parameter indicative of energy dissipation in protection applications [4.82].

5.2 Rate sensitivity of compressive strength and flow stress

In the current study, the quasi-static compressive strength of the TiAl/Ti₃Al-Al₂O₃ cermet has an average of 2780 ± 60 MPa, whereas the dynamic compressive strength has an average of 3410 ± 247 MPa, and this indicates an approximately 1.3 times increase in strength with a seven order increase in strain rate (from ~ 10⁻⁴ s⁻¹ to ~ 10³ s⁻¹). Most of the works done on other cermet systems investigated the rate-dependent compressive strength and reported similar orders of increase in strength under dynamic loading. For example, Mandel et al. [4.64] and Zhu et al. [4.66] reported increases in peak compressive strength between 1.3 and 1.5 times in strength in WC-Co system (from 4370 MPa to 6660 MPa with 10⁻⁴ s⁻¹ to 10³ s⁻¹ strain rate) and TiB₂-Al system (from 900 MPa to 1200 MPa with 0.0007 s⁻¹ to 1100 s⁻¹ strain rate), respectively. Some other cermet systems were reported to have lower rate-dependency on strength. For example, Li et al. [4.9] reported an increase in strength of 1.2 times in the A359 Al-20 vol% SiC_P cermet from 300 MPa to 360 MPa with 10⁻⁴ s⁻¹ to 2000 s⁻¹ strain rate. In another study, Behm et al. [4.83] reported almost no change in strength (850 – 900 MPa) in an Al 5038-B₄C cermet with 10⁻³ s⁻¹ to 4000 s⁻¹ strain rate increase. In contrast, Nawale et al. [4.84] and Hong and Gray [4.85] found over a two times increase in strength in A365 Al-Al₂O₃ (from 150 MPa to 350 MPa with 100 s⁻¹ to 1200 s⁻¹ strain rate) and 1060 Al-Al₂O₃ (from 130 MPa to 300 MPa with 0.001 s⁻¹ to 6000 s⁻¹ strain rate) cermet systems. Overall, the order of increase in compressive strength of the TiAl/Ti₃Al-Al₂O₃ cermet is comparable to other cermet systems, whereas the magnitude of the compressive strength is much higher than all the cermet systems, where aluminum is their matrix material. The rate sensitive and high compressive strength in the TiAl/Ti₃Al-Al₂O₃ cermet is likely a consequence of the relative high concentration of alumina (~ 65% volume percentage) and the ultrafine-grained structured of both phases in the current cermet [4.72]. This is important to note, as compressive strength has

been shown to be an important factor in the ballistic impact performance in some protection applications [4.25].

Next, we investigate the rate sensitivity of the TiAl/Ti₃Al-Al₂O₃ cermet. To do this, the compressive strength of the cermet is re-visited in Figure 4.12 for investigating the rate-sensitivity of the strength and its corresponding transition strain rate. A power law fit is performed on the data to populate the rate-dependency exponent and transition strain rate. The fit has the form:

$$\sigma_c = a * \dot{\epsilon}^n + \sigma_{QS_{avg}} \quad (6)$$

where σ_c (MPa) is the peak compressive strength, $\dot{\epsilon}$ (s⁻¹) is the corresponding strain rate, $\sigma_{QS_{avg}}$ (MPa) is the average compressive strength measured at quasi-static condition, n (unitless) is the rate-dependency exponent, and a (unitless) is the fitted coefficient which indicates the weight of the rate-dependency term. In this case, a rate-dependency exponent of approximately $n = 0.87$ is postulated by visualizing the goodness of fit, and the final results are plotted in the log scale to coincide with the literature. The y-interception value (“ $\sigma_{QS_{avg}}$ ” in the equation) is fixed to the average quasi-static compressive strength to represent the initial material strength. With an exponent of $n = 0.87$, the fitted coefficient “ a ” is nearly 1 with a R^2 value of 0.9, indicating the fit is good. In addition, a transitional strain rate between $8 \times 10^1 \text{ s}^{-1}$ and $5 \times 10^2 \text{ s}^{-1}$ is proposed based on the existing data. The proposed transitional strain rate region is indicated by a red box over the fitted curve in Figure 4.12.

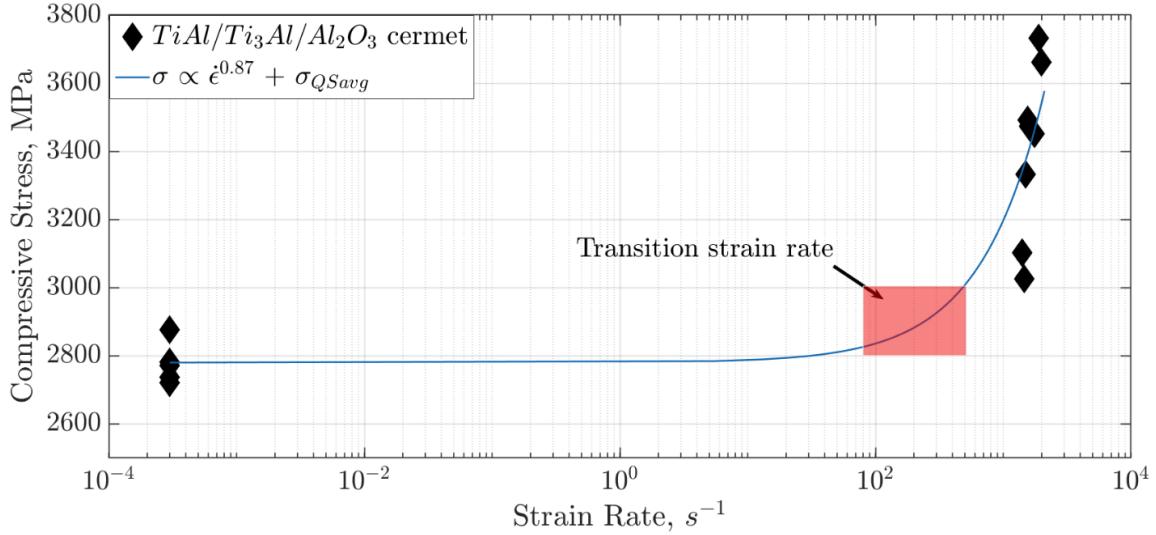


Figure 4.12: Summary of the compressive strength of the cermet at different strain rates (in log scale). A curve fit in the form of $\sigma_c = a * \dot{\epsilon}^n + \sigma_{QSavg}$ is used to determine the rate-dependency exponent, n , for compressive strength as well as the transitional strain rate. This is evaluated to be 80 to 500 s^{-1} . This method has been used widely in studying the rate dependency of brittle materials [4.89, 4.90]. The fitted coefficient, “ a ” is close to 1 with a R^2 value of 0.9, indicating a good fit.

In other literature investigations on the rate-dependency of particle-reinforced MMCs, Hong et al. [4.86], followed by Bao and Lin [4.87], proposed a framework based on the work of an Al-Zn-Mg-Cu alloy reinforced with SiC cermet and concluded that the rate sensitivity of the composite was highly dependent on the matrix material. The rate sensitivity, R_s , in Hong et al. [4.86] and Bao and Lin’s [4.87] work is expressed as:

$$R_s = \frac{\sigma_d - \sigma_s}{\sigma_s} \frac{1}{\ln\left(\frac{\dot{\epsilon}_d}{\dot{\epsilon}_s}\right)} \quad (7)$$

where σ_d (MPa) and σ_s (MPa) are the dynamic and quasi-static flow stresses at a constant plastic strain, respectively, and $\dot{\epsilon}_d$ (s^{-1}) and $\dot{\epsilon}_s$ (s^{-1}) are the corresponding strain rate. Instead of using the compressive strength (peak stress) as the reference point, flow stress at a constant plastic strain is used to determine the rate sensitivity of a material. By taking the flow stress at approximately 1.5% strain for all tests performed in the present study (after the first peak in dynamic tests), the rate sensitivity of the TiAl/Ti₃Al-Al₂O₃ cermet determined by using this method is between 0.025 to

0.030. This is higher than the rate sensitivity reported by Tan et al. [4.47] for a 50 vol.% SiC reinforced 2024 Al cermet ($R_s \sim 0.022$) and Guo et al. [4.88] for TiB₂-2024Al cermet ($R_s \sim 0$ at room temperature and $R_s \sim 0.01$ at 100 °C), suggesting that our material is quite rate sensitive.

The power law fitting method has been well established in the literature for investigating the rate-dependency exponent of brittle materials, and some well-known rate-dependency exponents have been proposed to model the rate sensitivity of compressive strength. For example, Lankford [4.89] used 1/3 as the exponent to describe the rate-dependency of the compressive strength for alumina. In another work, Kimberly [4.90] proposed another rate-dependency exponent as 2/3 to represent the group of brittle materials by considering crack-crack interactions under dynamic loading in a self-consistent framework. This was done under the assumption that the material would deform in the purely brittle manner (crack initiation, growth, and coalescence) with defined appropriate time scales and length scales for internal flaws and crack growth. For the TiAl/Ti₃Al-Al₂O₃ cermet in this study, it is believed that the rate-dependency exponent should not be bounded by these numbers because of the activation of the failure mechanisms in addition to cracking under dynamic loading. These extra energy-dissipation mechanisms, which are no longer observed in localized regions and small scales, are believed to manifest as the global “surface texturing” phenomenon under dynamic loading. The effects of extra failure mechanisms have also been noted by Lankford [4.91] that if the elastic expansion (kinetic) energy was no longer balanced by the pure fracture surface (potential) energy, the rate-dependency exponent could be much higher than the proposed 1/3. In a later work of Lankford [4.78], the rate sensitivities of a hot-pressed Si₃N₄ was found to be 0.87 at the strain rate of 10³ s⁻¹ and so values higher than 2/3 have been reported before. He concluded that this deviation from the formally proposed 1/3 rule was the consequence of localized plasticity and the suppression of local plastic flow by high loading rates. For material such as the

TiAl/Ti₃Al-Al₂O₃ cermet with a complicated nano-grained microstructure and combination of elastic and plastic deformation mechanisms, we found that the power law fit presented in this study (see Equation (6)) will provide a better postulate on the rate-dependency of the material. However, it is still recommended that investigations need to be done at the intermediate strain rates ($\sim 10^{-2}$ s⁻¹ to $\sim 10^2$ s⁻¹, such as a modified servo-hydraulic technique [4.134]) and higher strain rates ($> 10^4$ s⁻¹, such as plate impact experiments [4.135]) to probe a boarder range of material responses.

5.3 Rate-dependent failure mechanisms and crystalline texturing behavior

In this sub-section, the rate-dependency of the TiAl/Ti₃Al-Al₂O₃ cermet is explored in the context of the rate-dependent failure mechanisms (i.e., inter/transgranular cracking, particle fracture, dislocation and twinning), as well as the crystalline texturing phenomenon observed through XRD and high-speed imaging. First, the microscale mechanisms, such as inter/transgranular cracking and grain boundary delamination, are examined using SEM and EDS (see Fig. 4.7 and 4.8). In summary, a high density of intergranular cracking is observed under quasi-static loading, where minimal transgranular cracking is observed on both fracture and polished fracture surfaces. In addition, grain boundary delamination and particle pull-out constitute some of the major failure mechanisms under quasi-static compression, where small amounts of cleavage are observed in the titanium aluminide phase. Under dynamic loading, the material exhibits uneven fracture planes with much denser lamellar tearing occurring in the titanium aluminide matrix (see Fig. 4.8-c). A combination of intergranular *and* transgranular cracking are activated simultaneously during loading, and large amounts of particle cracking is observed on the polished fracture surface. In addition, void growth is observed on the polished fracture surface under dynamic loading, and they tend to grow along or within the alumina phase (see Fig. 4.8-a and b). With the voids acting as the sites for stress concentration, microcracks are likely to grow by connecting these voids, and these

eventually coalesce to form localized ductile crack networks. The different mechanisms observed under low and high strain rates can be interpreted using energy accumulated in different timescales. When the material is loaded at high strain rates, higher kinetic energy and stress introduced to the material at a smaller timescale results in particle fractures being prevalent [4.92]. At such small timescale, transgranular cracks could initiate in the matrix and propagate through the particles, when a much higher stress level is achieved within microseconds. This is different from intergranular cracking which requires less energy to exfoliate the interfaces and larger timescale for propagating along the particles [4.93]. Similarly, the apparent increase in void nucleation and growth can be the result of the higher level of strain energy generated under dynamic loading in the vicinity of the particle boundaries, and this is caused by stress concentration and localized tensile stress field at the matrix-particle interface from lateral expansion [4.93, 4.94]. This is likely why most of the voids are observed at the boundary of the alumina phase (see Fig. 4.8-b) in the current TiAl/Ti₃Al-Al₂O₃ cermet. In addition, void growth is usually connected with interface delamination and particle pull-out, which are major failure mechanisms observed in particle reinforced MMC studies [4.93, 4.95, 4.96]. To integrate particle pull-out in modeling work on particle-reinforced MMCs, Needleman [4.94, 4.97] used a cohesive zone model in his works to describe the process of void nucleation through interfacial debonding and concluded on the dynamic effect of stress redistribution around the matrix-particle interface. Eventually, this global increase in void growth indicates that the TiAl/Ti₃Al-Al₂O₃ cermet behaves in a more ductile manner under dynamic loading, and therefore leads to the greater area under the stress-strain curves (see Fig. 4.5).

Next, the cracking behavior of the TiAl/Ti₃Al-Al₂O₃ cermet is similar to what has been observed in the TiC-1080 steel by Kaplan et al. [4.57], who used TEM to probe the failure mechanisms

under both quasi-static and dynamic bending. They concluded interfacial cracking with crack propagation in the steel matrix being the major mechanism in the quasi-static case, and transgranular TiC particle cracking without extension to the steel matrix as the additional mechanisms activated under dynamic loading. In other cermet studies, particle fracture under dynamic loading was also observed extensively, whereas matrix fracture and particle debonding were found commonly in quasi-static tests [4.47, 4.66, 4.98]. In addition, Hao et al. [4.99] concluded that at room temperature, the γ -based TiAl alloy they tested under dynamic compression was in a brittle shear failure owing to the rapid propagation of micro-cracks along the lamella interface. In the current study, this may explain the significantly denser cleavage observed in the titanium aluminide matrix under dynamic loading of the TiAl/Ti₃Al-Al₂O₃ cermet. In some cermet systems with aluminum being the matrix, matrix melting by adiabatic heating within the shear bands under dynamic loading was observed (e.g., 2024 Al-SiC cermet [4.47] and 2024 Al-TiB₂ cermet [4.66]), but such phenomenon is not observed in any investigated sites in the current study on the TiAl/Ti₃Al-Al₂O₃ cermet. We believed that even though shear banding is one of the deformation mechanisms that could be activated in titanium aluminide under isothermal compression [4.100], it is not likely to be the cause of failure under room temperature dynamic compression at $\sim 10^3 \text{ s}^{-1}$ strain rates.

Next, TEM analysis (see Fig. 4.10) on the fragments from dynamic experiments revealed globally-distributed dislocations and twinning in the titanium aluminide phase, with localized dislocations observed in the alumina phase. Many studies have been focused on deformation dislocations and twins in γ -based TiAl alloys and their influences in material properties [4.101 – 4.104]. For example, Appel [4.105] investigated deformation twinning in a Ti-(45–49)Al + (0.3–10)X alloy (X being third elements) under different deformation conditions, such as strain rates, creep, and

fracture. Detailed crystallographic information has also been given on twin nucleation and propagation, boundary structures, and interactions between dislocations and twins. In another study, Maloy and Gray [4.73] explored the high strain rate compressive deformation mechanisms of a Ti-48Al-2Nb-2Cr alloy under strain rates between 0.001 s^{-1} and 2000 s^{-1} . They found extensive twinning and dislocations in between and across the γ/α_2 lamellae, and their amounts increased with increasing strain rate. Other recent studies (e.g., Beran et al. [4.106] and Guo et al. [4.107]) also observed similar nanoscale twinning and dislocation activities under different mechanical loadings and temperatures, with clear rate-dependencies on their extent. This confirms the observations in the current material that dislocation and twinning are universal in titanium aluminide under high-rate loading.

Finally, crystalline texturing of the TiAl/Ti₃Al-Al₂O₃ cermet is studied by 2D-XRD (see Fig. 4.11) and confirmed with high speed video images demonstrating deformation features on the surface of the specimen during dynamic compression experiments (see Fig. 4.5). The 2D diffraction results reveal extensive crystalline texturing occurring in titanium aluminide under dynamic loading, while the alumina phase remains in its randomly orientated polycrystalline structure. It is believed that this crystalline texturing behavior is the consequences of dynamic recrystallization and grain reorientation in the titanium aluminide phase [4.108, 4.109], and this eventually leads to a large scale surface texturing observed in the high speed videos in dynamic tests (see Fig. 4.5-c). The dynamic recrystallization and grain reorientation behavior often lead to extensive microstructural evolution, and this can be asserted by comparing the as-received (see Fig. 1-c) and deformed (see Fig. 4.9-a) states of the material. In the TiAl/Ti₃Al-Al₂O₃ cermet, the titanium aluminide phase undergoes global and extensive microstructural changes (from a combination of equiaxed and randomly orientated lamellar structures to uniformly orientated and alternating γ/α_2 lamellae), and

the alumina phase remains permanent for uniaxial compressive loading rates of at least up to $\sim 2 \times 10^3 \text{ s}^{-1}$ strain rate.

Microstructural evolution and crystalline texturing have been considerably studied in titanium aluminide, due to its capacity for forming complex microstructures and their significant effects on material performance. For example, Wang et al. [4.101] and Wu et al. [4.102] investigated the dynamic recrystallization behavior of TiAl alloys during high-rate compression and found severe microstructural and crystalline texture evolution, and they were found to be closely related to dislocation and twinning activities occurring during loading. Wu et al. [4.102] also pointed out that the degree of crystalline texturing and dynamic recrystallization is sensitive to strains. In the TiAl/Ti₃Al-Al₂O₃ cermet in this study, as the failure strain increases with increasing strain rate, the crystalline texturing becomes more dominant and this manifests macroscopically. It is known that material properties (i.e., strength) and deformation mechanisms (i.e., dislocation) can be highly dependent on the material texturing and its related changes in the microstructure [4.110, 4.111]. The activation of dislocations and twins in the titanium aluminide phase in the current cermet can be a consequence of crystalline texturing followed by profound microstructural changes [4.112]. The evolution of crystalline textures is also likely the driver for the “flow softening-hardening” behavior observed in the dynamic stress-strain curves (see Fig. 4.5-a), and subsequently, the large variabilities in the stress-strain behavior. Studies on other cermets (e.g., Al 5083-B₄C cermet [4.59] and TiB₂-2024 Al cermet [4.88]) also found significant dynamic recrystallization and microstructural changes in the matrix (aluminum in these two studies) under high-rate compression, and they were associated with dislocations or twinning. As a result, further insights on material rate sensitivity could be gained by the additional deformation mechanisms and their magnitude with increasing strain rates on top of the commonly accepted microcracking

mechanism. Therefore, it is important to study the crystalline texturing behavior in detail with specific tools (i.e., pole figures) and pinpoint its exact effects on the material behavior for this complex cermet.

5.4 Implication of the material in protection applications

In this final sub-section, implications of the experimental studies on the TiAl/Ti₃Al/ Al₂O₃ cermet for protection applications, such as body armor, will be evaluated by highlighting some major ballistic performance metrics. The importance of incorporating rate-dependent mechanical properties and material behaviors for better ballistic performance prediction will be emphasized. Material improvements on ballistic performance from the material science perspectives will be underscored as well.

The ballistic performance of an armor material is generally considered from the perspective of some commonly defined criteria, such as ballistic efficiency, ballistic limit (V50), and ballistic energy dissipation capacity (the *D*-criterion). The frequently used ballistic efficiency index-differential efficiency factor (DEF) is defined as [4.113]:

$$DEF = \frac{(P_0 - P_r) * \rho_0}{(t_c * \rho_c)} \quad (8)$$

where P_0 (m) and P_r (m) are the reference and residual penetration of projectile in backing rolled homogeneous armor (RHA), respectively; t_c (m) denotes the ceramic target thickness; and ρ_0 (kg/m³) and ρ_t (kg/m³) denote the density of RHA and ceramic target, respectively. This is one of the simplest criteria in evaluating ballistic performance, where only tile geometry and depth of penetration are often considered [4.114]. To evaluate the effectiveness of a material using this metric along for material improvement is tedious in that it requires significant amounts of expensive testing and does not provide any guidelines in the direction of material improvement.

Next, in the National Institute of Justice (NIJ) standard-0101.06 [4.115], the ballistic limit is defined as the velocity at which the projectile is expected to penetrate the armor at least 50% of the times for a given bullet type. Numerous empirical equations have been developed for specific materials or systems to better predict their ballistic limits. These expressions seek to tie critical mechanical properties to ballistic performance. For instance, Villanueva and Cantwell [4.116] developed the well-known expression for composite laminates:

$$V_{50_laminare} = \frac{\pi\Gamma\sqrt{\rho_t * \sigma_e}D^2T}{4m} \left[1 + \sqrt{1 + \frac{8m}{\pi\Gamma^2\rho_tD^2T}} \right] \quad (9)$$

where Γ (unitless) is the projectile constant; ρ_t (kg/m^3) is the density of the laminate target; σ_e (Pa) denotes the quasi-static compressive strength of the target; D (m) denotes the diameter of the projectile; T (m) is the thickness of the projectile and m (kg) is the mass of the projectile. In this case, the quasi-static compressive strength is considered by Villanueva and Cantwell [4.116] as the most important parameter in ballistic performance of one laminate tile. No specific expression on estimating the ballistic limit for ceramics or cermet systems has yet being developed. However, considering only the quasi-static compressive strength does not appear to be a good indication of the material capacity in stopping the projectile during an impact event given the clear rate-dependency observed on the compressive strength for most of the ceramics and cermets, in this study the TiAl/Ti₃Al-Al₂O₃ cermet. More attention is needed to incorporate the rate sensitivity of the material into the metric for more accurate prediction [4.82, 4.117]. In other works, for example, Lankford [4.78] emphasized the role of the dynamic mechanical properties for ceramic armor and deduced the relationship between the fragmentation behavior of the materials and strain rate dependent fracture mechanisms, as well as the inertial confinement generated under high-rate loading. In the current study for the TiAl/Ti₃Al-Al₂O₃ cermet, finding an appropriate way to

incorporate the rate-sensitive mechanical properties into some metrics, such as compressive strength and failure strain, will be critical in more accurately predicting the material performance under impact.

Next, Neshpor et al. [4.118] proposed the term ballistic energy dissipation ability (D -criterion) for ceramic armors:

$$D = \frac{0.36(HV * E * c)}{K_{1c}^2} \quad (10)$$

where HV (MPa) is the Vickers hardness; E (MPa) is the Young's modulus (stiffness); c (m/s) is the sound velocity in the material and can be approximated by $\sqrt{\frac{E}{\rho}}$; and K_{Ic} (MPa · m^{1/2}) is the fracture toughness. More fundamental material properties are incorporated into this metric for advanced ceramics, and this is shown to give a more accurate prediction on the ballistic performance based on the understanding of the dwell (hardness and stiffness dependent) and penetration phases (fracture toughness dependent) occur during a ballistic impact event [4.79]. Eq. (10) indicates that a trade-off must be made between the dwell and penetration properties (i.e., hardness and stiffness in the numerator and fracture toughness in the denominator). One of the limiting factors in using advanced ceramics in protection applications is their sacrifice in fracture toughness to achieve high hardness for projectile defeat [4.119 – 4.122]. Instead, one of the major goals in cermet research is to introduce certain amounts of ductility into ceramics by incorporating a metallic phase, an intermetallic phase in the case of the TiAl/Ti₃Al-Al₂O₃ cermet, so that this results in an increase on the capacity of energy dissipation during projectile penetration [4.4]. For the TiAl/Ti₃Al-Al₂O₃ studied in this work, the increase in failure strains when compared to other advanced ceramics indicates an increase in ductility and fracture toughness, while maintaining a comparable compressive strength with some of the advanced ceramics (e.g., alumina [4.38]). The

combination of higher failure strains and comparable compressive strength provides some knowledge on the increase in fracture toughness. In addition, the 1.4 times increase in failure strain and the 1.3 times increase in compressive strength under dynamic loading in the current cermet results in significantly higher dynamic fracture toughness than that of its quasi-static counterpart. Similar results have been shown in other cermet systems (e.g., ~ 3 times increase in fracture toughness in a TiC-1080 steel cermet from quasi-static to dynamic bending tests [4.17]). Unlike other cermet systems with aluminum or steel being the matrices, the intermetallic titanium aluminide in the current cermet system preserves a much higher strength and stiffness (i.e., < 1.2 GPa in compressive strength for Al-based cermets [4.72, 4.84, 4.123]), which are critical properties in ballistic performance.

Overall, metrics of ballistic performance are represented by either critical mechanical properties, such as density, stiffness, compressive strength, hardness, and fracture toughness, or armor system variables, such as tile thickness, tile geometry, and projectile information. From a material science perspective, more focus is dedicated to improving the mechanical properties of one material, essentially, finding the optimized microstructure (i.e., phase compositions, grain size and shape, secondary reinforcements) [4.30, 4.125 – 4.128]. For example, Landingham and Casey [4.129] provided proof of an optimal phase composition for a TiC-based (Ni, Mo) enhanced cermet in terms of ballistic limit performance. At about 10 vol% of (Ni, Mo) metallic phases, the ballistic limit (V50) could reach 3100 ft/s, which is 20% higher than pure TiC ceramic and 7% higher than the material containing 33 vol% of (Ni, Mo) metallic phases. In the case of the TiAl/Ti₃Al-Al₂O₃ cermet in this study, controlling the phase composition by tailoring the initial powders, adding alloying elements, and changing the microstructure by heat treatments is expected to result in notable changes in material properties. Specifically, tailoring the microstructure of the titanium

aluminide phase to reduce the effect of crystalline texturing is believed to alter the flow stress softening and, perhaps, deliver better performances under impact [4.58, 4.112, 4.130]. In addition, fragmentation behavior of the target material, which has an influence on projectile erosion [4.79], is worth studying in length. According to numerous studies, fragmentation will likely be affected by the microstructure, and hence the fracture mechanisms [4.78, 4.131, 4.132]. It is concluded that the cermet materials need to be systematically studied before they can ultimately replace the role of advanced ceramics, such as alumina in protection applications.

6. Conclusion

In this study, the rate-dependency of a SHS-synthesized TiAl/Ti₃Al-Al₂O₃ cermet was investigated using mechanical testing and advanced microscopy. Quasi-static and dynamic uniaxial compression tests coupled with high-speed imaging and DIC were performed to assess the rate-dependent mechanical responses, including stress-strain behavior, compressive strength, failure strain, and macroscopic failure, and these were compared with other advanced ceramics and cermet systems. The TiAl/Ti₃Al-Al₂O₃ cermet exhibited the “flow hardening-softening” phenomenon under dynamic loading with increased compressive strengths and failure strains when compared with the quasi-static counterpart. In addition, the current material had a much higher magnitude of compressive strength than most of the aluminum-based cermets while maintaining a comparable order of increase with increasing strain rates. A rate-dependency exponent of 0.87 was proposed to capture the rate sensitivity of the peak compressive strength. Advanced characterization, including SEM, HR-TEM, 2D-XRD were used to explore the rate-dependency in failure mechanisms of the current material, where globally distributed dislocations and twinning were observed under dynamic loading. Extensive cleavage in the TiAl phase, void growth, transgranular cracking, and particle fracture were identified as the main failure mechanisms under high strain

rates. Crystalline texturing behavior in the TiAl phase was identified by 2D-XRD, where extensive microstructural evolution with grain reorientation and dynamic recrystallization was observed under TEM. The post-deformed TiAl phase reveals a fully lamellar structure with alternating γ/α_2 lamellae. This microscopic texturing behavior eventually manifested as the macroscopic surface texturing observed under dynamic loading using high-speed imaging. Altogether, this study delivers a comprehensive understanding on the rate-dependent mechanical properties and failure mechanisms of the TiAl/Ti₃Al-Al₂O₃ cermet. Furthermore, the data generated in this study provides insights in cermet material micromechanical modeling and optimization.

Chapter 5: Concluding Remarks

5.1 Conclusion

The focus of this thesis has been to understand the TiAl/Ti₃Al-Al₂O₃ oxide cermet in the context of 1. As-received microstructures; 2. Rate-dependent mechanical properties; 3. Rate-dependent failure mechanisms; and 4. Material evaluation in ballistic performance and potential routes for material improvements. To assess the above information, advanced microscopy techniques, including high-resolution scanning electron microscopy, high-resolution (scanning) transmission electron microscopy, energy-dispersive x-ray spectroscopy for both SEM and TEM, and two-dimensional x-ray diffraction were used to investigate the microstructural features and crystallinity of the material before and after deformation. Mechanical testing, including quasi-static and dynamic uniaxial compression tests, were carried out on a standard servo-hydraulic MTS machine and split-Hopkinson pressure bar, respectively. State-of-the-art high-speed imaging coupled with digital image correlation technique was used to visualize surface deformation, relate microscopic failure mechanisms with macroscopic manifestation, and to establish stress-strain relationships.

This thesis achieves its objective of providing a comprehensive understanding of the TiAl/Ti₃Al-Al₂O₃ cermet in the form of two peer-reviewed papers (Chapter 3 and 4). The main results from the works are listed below for further emphasis:

- i. EDS investigation reveals three phases present in the as-received cermet: 1. γ -TiAl phase; 2. α_2 -Ti₃Al phase; and 3. Al₂O₃ phase. The α_2 -Ti₃Al phase is considered a byproduct from the SHS process. However, this phase has positive effects on the toughness of the cermet due to the increased oxygen precipitation at the ($\gamma + \alpha_2$) lamellar interface;

- ii. A “coral” network of alumina particles is identified in the as-received ultrafine-grained TiAl/Ti₃Al-Al₂O₃ cermet. This is a characteristic feature as an outcome of the SHS process, and the “coral” network could be beneficial for load transfer under stress;
- iii. A ~ 1.3 times increase in compressive strength from 2780 ± 60 MPa to 3410 ± 247 MPa and a ~ 1.4 times increase in failure strain from 0.0166 ± 0.0017 to 0.0264 ± 0.0032 are determined in the TiAl/Ti₃Al-Al₂O₃ cermet with a seven order increase in strain rates from ~ 10⁻⁴ s⁻¹ to ~ 10³ s⁻¹. The rate-sensitivity of the current cermet is significantly higher than other aluminum-based cermet systems;
- iv. The TiAl/Ti₃Al-Al₂O₃ cermet has a comparable compressive strength, higher failure strain, and larger structural fragments when compared to alumina AD995, suggesting a higher fracture toughness and its positive potentials in some structural applications (e.g., armor). The current cermet also retains much higher stiffness and strength than the aluminum-based cermet systems, and this is attributed to the intermetallic-based structure, high volume fraction of alumina particles, and ultrafine-grained structure of both phases;
- v. The stress-strain behavior of the TiAl/Ti₃Al-Al₂O₃ cermet exhibits a series of alternating stress relaxation and strain hardening cycles under dynamic compression, while continuous strain hardening is observed under quasi-static compression. This indicates a different failure process in the cermet at different loading rates;
- vi. The TiAl/Ti₃Al-Al₂O₃ cermet exhibits macroscopic surface texturing during dynamic testing, and this is correlated with the crystalline texturing behavior found

in the titanium aluminide phase and the cyclical stress relaxation and strain hardening behavior in the stress-strain curves;

- vii. Profound microstructural evolution as a result of dynamic recrystallization and grain reorientation are observed in the TiAl/Ti₃Al-Al₂O₃ cermet under dynamic loading. The dominant failure mechanisms include extensive cleavage in the titanium aluminide phase, void growth, transgranular cracking, and particle fracture. Globally distributed dislocations and twinning are also observed as a consequence of dynamic compressive loading.

4.2 Implication

In this thesis, we provided a thorough understanding of an SHS-fabricated TiAl/Ti₃Al-Al₂O₃ cermet with detailed characterization and mechanical testing at different strain rates. The cermet exhibited rate-dependency on both mechanical properties and failure mechanisms under uniaxial compression at different loading rates. Past literature on similar cermets was focused on the advanced manufacturing methods [51, 52, 54 – 56], where limited studies were published on the mechanical testing of the material. Exploring the material behaviors at different loading rates is nevertheless critical in assessing material performance in the impact-prevalent structural applications. The experimental and characterization data generated in this thesis will enrich the TiAl/Ti₃Al-Al₂O₃ cermet literature, as well as that of cermet material literature in general.

Altogether, this work makes the following contributions:

- i. Developing a comprehensive framework for studying brittle cermet materials by incorporating DIC, high-speed-imaging, and advanced characterization techniques. This work can be extended to the study of other brittle materials, such as ceramics;

- ii. Characterizing the microstructure of the as-received TiAl/Ti₃Al-Al₂O₃ cermet material, which serves as important inputs in constructing a unit cell material model that could be implemented into large-scale computational simulations. Co-authored paper titled “An experimental and numerical study of novel nano-grained ($\gamma + \alpha_2$)-TiAl/Al₂O₃ cermets” has been published in *Material Science and Engineering A* [64] and “The mechanical response of an α_2 (Ti₃Al) + γ (TiAl)-submicron grained Al₂O₃ cermet under dynamic compression: modeling and experiment” is undergoing minor revisions in *Acta Materialia*;
- iii. Understanding the novel SHS-fabricated TiAl/Ti₃Al-Al₂O₃ cermet through mechanical testing. Rate-dependency on mechanical properties and failure mechanisms are comprehensively investigated, for which the data sets are valuable for both evaluating material performance in protection applications and in implementing material features in micromechanical modeling;
- iv. Providing the first set of rate-dependent stress-strain curves, compressive strength, and failure strain data, which can be used as a reference for future studies of similar materials. This data is also valuable in material model validation;
- v. Delivering an inclusive comparison of the mechanical properties and failure mechanisms of the TiAl/Ti₃Al-Al₂O₃ cermet to other advanced ceramics and cermet systems. This data set may provide insights to the industries when the material is considered to be used in some of their applications (e.g., personnel protection, automotive, and aerospace).

4.3 Future Works and Recommendations

To the best of our knowledge, this work is the first report on the experimental mechanics of the TiAl/Ti₃Al-Al₂O₃ cermet at the date of submission. The lack of experimental works might be because of the novelty of the material, the difficulties in studying brittle materials experimentally, and the only recent developments in coupling high-speed imaging and DIC techniques. The data generated in this thesis could be the first-hand information for material modeling and model validation. To build upon the current work, the following future directions and recommendations are suggested:

- i. Tailor material microstructure through manufacturing (e.g., adding alloying elements) and heat treatments (e.g., modify titanium aluminide microstructure), and this will significantly change the mechanical properties and failure mechanisms of the cermet [65];
- ii. Design proper experimental setup for fragment collection, for which quantitative fragmentation analysis can be performed with the automated morphology microscope. Studying the fragmentation behavior of one material is proven to be crucial in structural applications [66] [67];
- iii. Conduct laboratory-scale confined compression experiments to assess material damage and fragmentation behavior for different stress states, and study the effect of pressure on rate sensitivity of fracture strength;
- iv. Modify the SHPB system (e.g., pulse shaper) to access moderate strain rate so that the gap between low strain rate (i.e., $\sim 10^{-4} \text{ s}^{-1}$) and relative high strain rate (i.e., $\sim 10^3 \text{ s}^{-1}$) can be explored;

- v. Develop new laboratory-scale (e.g., edge-on-impact, high-speed tension) and full scale (e.g., ballistic impact, shock) experiments, for which data generated will be valuable in modeling (e.g., material damage, tensile behavior) and validation (e.g., damage pattern visualization, ballistic limit);
- vi. Collaborate with facilities, such as nanoFAB and Canadian Light Source synchrotron, to perform in-situ testing (e.g., in-situ high-temperature SEM, TEM, and XRD, in-situ computed tomography with compression and tension at different loading rates, etc.) and obtain information on instantaneous response (e.g., damage accumulation, microstructure changes) of material;
- vii. Explore suitable analytical and phenomenological models that could be used in large-scale simulations (e.g., the Johnson-Holmquist-2 model for shock and impact simulations) for cermet materials, and obtain and validate a set of model parameters through the design of experiments (e.g., indentation, bending);
- viii. In addition to point vi, one can modify the existing analytical and phenomenological models by adding terms (i.e., stiffness damage/softening) or changing the term representation functions base on experimental results.

Bibliography

- [1] Clyne, T. W., and P. J. Withers. *An introduction to metal matrix composites*. Cambridge university press, 1995.
- [2] E. Schmidt (1924) German Patents Nos 425451, 425452 and 427370.
- [3] Zweben, Carl, et al., eds. *Comprehensive composite materials*. Elsevier Science, 2000.
- [4] Chawla, Krishan K. "Metal matrix composites." *Materials Science and Technology* (2006).
- [5] Liu, D. M., and W. H. Tuan. "Microstructure and thermal conduction properties of Al₂O₃-Ag composites." *Acta materialia* 44.2 (1996): 813-818.
- [6] Compton, B. G., and F. W. Zok. "Impact resistance of TiC-based cermets." *International Journal of Impact Engineering* 62 (2013): 75-87.
- [7] Tinklepaugh, James Root, and William B. Crandall, eds. *Cermets*. Reinhold Publishing Corporation, 1960.
- [8] Goetzel, Glaus G. "Metals HandBook." *Powder Metallurgy* 7.551 (1984): 566.
- [9] Ettmayer, Peter. "Hardmetals and cermets." *Annual Review of Materials Science* 19.1 (1989): 145-164.
- [10] Mari, Daniele. "Cermets and hardmetals." (2011).
- [11] J. Chevalier, L. Gremillard, Ceramics for medical applications: A picture for the next 20 years, *Journal of the European Ceramic Society* 29 (7) (2009) 1245 – 1255.
- [12] Wilkins, M. L., C. F. Cline, and C. A. Honodel. *FOURTH PROGRESS REPORT OF LIGHT ARMOR PROGRAM*. No. UCRL-50694. California Univ., Livermore. Lawrence Radiation Lab., 1969.

- [13] Landingham, R. L., and A. W. Casey. *Final report of the light armor materials program*. No. UCRL--51269. California Univ., 1972.
- [14] Strassburger, E., et al. "Behaviour of Al₂O₃-Al ceramic metal composites under projectile impact." *Le Journal de Physique IV* 10.PR9 (2000): Pr9-605.
- [15] Ischenko, A. N., et al. "Investigation of impact resistance of protective barriers made from cermets." *Russian Physics Journal* 58.9 (2016): 1347-1352.
- [16] Loiseau, J., et al. "Ballistic Response of Chromium/Chromium-Sulfide Cermets." *Journal of Dynamic Behavior of Materials* 1.3 (2015): 347-358.
- [17] Madheswaran, K., S. Sugumar, and B. Elamvazhudi. "Mechanical characterization of Aluminium–Boron carbide composites with influence of Calcium carbide particles." *International Journal of Emerging Technology and Advanced Engineering* 5.7 (2015): 492-496.
- [18] Kurzawa, Adam, et al. "Analysis of ballistic resistance of composites based on EN AC-44200 aluminum alloy reinforced with Al₂O₃ particles." *Composite Structures* 201 (2018): 834-844.
- [19] Guo, Q., et al. "Residual microstructure and damage geometry associated with high speed impact crater in Al₂O₃ and TiB₂ particles reinforced 2024 Al composite." *Materials Characterization* 66 (2012): 9-15.
- [20] Dosta, S., M. Couto, and J. M. Guilemany. "Cold spray deposition of a WC-25Co cermet onto Al7075-T6 and carbon steel substrates." *Acta Materialia* 61.2 (2013): 643-652.
- [21] Meier, G. H., et al. "Environmental behaviour of intermetallic materials." *Structural Intermetallics*, R. Darolia, JJ Lewandowski, CT Liu, PL Martin, DB Miracle, MV Nathal (editors), TMS, Warrendale 861 (1993).
- [22] Liang, Yongfeng, and Junpin Lin. "Fabrication and Properties of γ -TiAl Sheet Materials: A Review." *JOM*, vol. 69, no. 12, 2017, pp. 2571–75, doi:10.1007/s11837-017-2551-z.

- [23] Djanarthany, S., J-C. Viala, and J. Bouix. "An overview of monolithic titanium aluminides based on Ti₃Al and TiAl." *Materials chemistry and physics* 72.3 (2001): 301-319.
- [24] Appel, F., and R. Wagner. "Microstructure and deformation of two-phase γ -titanium aluminides." *Materials science and engineering: r: reports* 22.5 (1998): 187-268.
- [25] Shu, Shili, et al. "Comparative study of the compression properties of TiAl matrix composites reinforced with nano-TiB₂ and nano-Ti₅Si₃ particles." *Materials Science and Engineering: A* 560 (2013): 596-600.
- [26] Lapin, J., L. Ondrúš, and O. Bajana. "Effect of Al₂O₃ particles on mechanical properties of directionally solidified intermetallic Ti-46Al-2W-0.5 Si alloy." *Materials Science and Engineering: A* 360.1-2 (2003): 85-95.
- [27] "Advanced-Alumina-Brochure." Coorstek.Inc, 2016.
<https://www.coorstek.com/media/1715/advanced-alumina-brochure.pdf>
- [28] Rosenberg, Zvi, and Erez Dekel. *Terminal ballistics*. Berlin: Springer, 2012.
- [29] Weeks, Carrell Elizabeth. Evaluation of a gamma titanium aluminide for hypersonic structural applications. Diss. Georgia Institute of Technology, 2005.
- [30] Taya, Minoru, and Richard J. Arsenault. *Metal matrix composites: thermomechanical behavior*. Elsevier, 2016.
- [31] Johnson Jr, Aldie E. "Mechanical properties at room temperature of four cermets of tungsten carbide with cobalt binder." (1954).
- [32] Kerper, Matthew J., et al. "Evaluation of tensile, compressive, torsional, transverse, and impact tests and correlation of results for brittle cermets." *Journal of Research of the National Bureau of Standards* 61.3 (1958): 149.

- [33] D Deng, H., and S. Nemat-Nasser. "Dynamic damage evolution in brittle solids." *Mechanics of Materials* 14.2 (1992): 83-103.
- [34] Lankford, J. "Mechanisms responsible for strain-rate-dependent compressive strength in ceramic materials." *Journal of the American Ceramic Society* 64.2 (1981): C-33.
- [35] Holland, Chance C., and Robert M. McMeeking. "The influence of mechanical and microstructural properties on the rate-dependent fracture strength of ceramics in uniaxial compression." *International Journal of Impact Engineering* 81 (2015): 34-49.
- [36] Anand, L. "Constitutive equations for the rate-dependent deformation of metals at elevated temperatures." *Journal of engineering materials and technology* 104.1 (1982): 12-17.
- [37] Bammann, Douglas J. "Modeling temperature and strain rate dependent large deformations of metals." *Applied Mechanics Reviews* 43.5S (1990): S312-S319.
- [38] Steinberg, D. J., S. G. Cochran, and M. W. Guinan. "A constitutive model for metals applicable at high-strain rate." *Journal of applied physics* 51.3 (1980): 1498-1504.
- [39] Rittel, D., N. Frage, and M. P. Dariel. "Dynamic mechanical and fracture properties of an infiltrated TiC-1080 steel cermet." *International journal of solids and structures* 42.2 (2005): 697-715.
- [40] Kaplan, W. D., et al. "Static and dynamic mechanical damage mechanisms in TiC-1080 steel cermets." *Scripta materialia* 51.1 (2004): 37-41.
- [41] Mandel, Kristin, Markus Radajewski, and Lutz Krüger. "Strain-rate dependence of the compressive strength of WC-Co hard metals." *Materials Science and Engineering: A* 612 (2014): 115-122.

- [42] Guden, M., and Ian W. Hall. "Quasi-static and dynamic compression behaviour of an FPTM alumina-reinforced aluminum metal matrix composite." *Journal of materials science* 33.13 (1998): 3285-3291.
- [43] Ramesh, K. T., and G. Ravichandran. "Dynamic behavior of a boron carbide aluminum cermet: experiments and observations." *Mechanics of Materials* 10.1-2 (1990): 19-29.
- [44] Blumenthal, W. R., G. T. Gray, and T. N. Claytor. "Response of aluminium-infiltrated boron carbide cermets to shock wave loading." *Journal of materials science* 29.17 (1994): 4567-4576.
- [45] Lu, Y. X., et al. "Microstructure and mechanical behaviour of a SiC particles reinforced Al-5Cu composite under dynamic loading." *Journal of materials processing technology* 94.2-3 (1999): 175-178.
- [46] Rhee, S. K. "Wetting of ceramics by liquid metals." *Journal of the American Ceramic Society* 54.7 (1971): 332-334.
- [47] Munson, D. E., and R. J. Lawrence. "Dynamic deformation of polycrystalline alumina." *Journal of Applied Physics* 50.10 (1979): 6272-6282.
- [48] Lankford, James. "Compressive strength and microplasticity in polycrystalline alumina." *Journal of Materials Science* 12.4 (1977): 791-796.
- [49] Semiatin, S. L., et al. "Plastic-flow behavior and microstructural development in a cast alpha-two titanium aluminide." *Metallurgical Transactions A* 23.1 (1992): 295-305.
- [50] Maloy, S. A., and G. T. Gray III. "High strain rate deformation of Ti₄₈Al₂Nb₂Cr." *Acta Materialia* 44.5 (1996): 1741-1756.
- [51] Shen, Y. F., et al. "Properties and electronic structures of titanium aluminides-alumina composites from in-situ SHS process." *Materials Science and Engineering: A* 528.4-5 (2011): 2100-2105.

- [52] Cai, Z. H., and D. L. Zhang. "Sintering behaviour and microstructures of Ti (Al, O)/Al₂O₃, Ti₃Al (O)/Al₂O₃ and TiAl (O)/Al₂O₃ in situ composites." *Materials Science and Engineering: A* 419.1-2 (2006): 310-317.
- [53] Munir, Zuhair A., and Umberto Anselmi-Tamburini. "Self-propagating exothermic reactions: the synthesis of high-temperature materials by combustion." *Materials Science Reports* 3.6 (1989): 279-365.
- [54] Gaus, Shaun P., et al. "Alumina–Aluminide Alloys (3A) Technology: II, Modeling of Ti_xAl_y–Al₂O₃ Composites Formation." *Journal of the American ceramic society* 83.7 (2000): 1606-1612.
- [55] Kamali, Ali Reza, et al. "Production of TiAl (Ti₃Al)/Al₂O₃ Nanocomposite." *Journal of Nano Research*. Vol. 3. Trans Tech Publications, 2008.
- [56] Forouzanmehr, N., F. Karimzadeh, and M. H. Enayati. "Synthesis and characterization of TiAl/ α -Al₂O₃ nanocomposite by mechanical alloying." *Journal of Alloys and Compounds* 478.1-2 (2009): 257-259.
- [57] Reimer, Ludwig. *Transmission electron microscopy: physics of image formation and microanalysis*. Vol. 36. Springer, 2013.
- [58] Wang, Z. L. "Transmission electron microscopy of shape-controlled nanocrystals and their assemblies." (2000): 1153-1175.
- [59] Fultz, Brent, and James M. Howe. *Transmission electron microscopy and diffractometry of materials*. Springer Science & Business Media, 2012.
- [60] Suryanarayana, Challapalli, and M. Grant Norton. *X-ray diffraction: a practical approach*. Springer Science & Business Media, 2013.
- [61] Li, H. Y., P. Motamedi, and J. D. Hogan. "Characterization and mechanical testing on novel (γ + α 2)–TiAl/Ti₃Al/Al₂O₃ cermet." *Materials Science and Engineering: A* 750 (2019): 152-163.

- [62] Atkinson, Alan, et al. "Advanced anodes for high-temperature fuel cells." *Materials for Sustainable Energy: A Collection of Peer-Reviewed Research and Review Articles from Nature Publishing Group*. 2011. 213-223.
- [63] Antonaia, A., et al. "Stability of W-Al₂O₃ cermet based solar coating for receiver tube operating at high temperature." *Solar Energy Materials and Solar Cells* 94.10 (2010): 1604-1611.
- [64] Amirian, B., H. Y. Li, and J. D. Hogan. "An experimental and numerical study of novel nano-grained ($\gamma + \alpha_2$)-TiAl/Al₂O₃ cermets." *Materials Science and Engineering: A* 744 (2019): 570-580.
- [65] Gil, Ignacio, Maria A. Muñoz-Morris, and David G. Morris. "The effect of heat treatments on the microstructural stability of the intermetallic Ti-46.5 Al-2W-0.5 Si." *Intermetallics* 9.5 (2001): 373-385.
- [66] Grady, Dennis E. "Length scales and size distributions in dynamic fragmentation." *International Journal of Fracture* 163.1-2 (2010): 85-99.
- [67] Hogan, James David, et al. "Fragmentation of an advanced ceramic under ballistic impact: mechanisms and microstructure." *International journal of impact engineering* 102 (2017): 47-54.
- [68] Mossino, P. "Some aspects in self-propagating high-temperature synthesis." *Ceramics International* 30.3 (2004): 311-332.
- [69] Merzhanov, A. G. "Self-propagating high temperature synthesis and powder metallurgy: Unity of goals and competition of principles." *Advances in Powder Metallurgy & Particulate Materials--1992*. 9 (1992): 341-368.
- [70] Levashov, E. A., et al. "Self-propagating high-temperature synthesis of advanced materials and coatings." *International Materials Reviews* 62.4 (2017): 203-239.

- [71] Sytschev, Alexandr E., and Alexander G. Merzhanov. "Self-propagating high-temperature synthesis of nanomaterials." *Russian chemical reviews* 73.2 (2004): 147-159.
- [72] Das, Siddhartha. "The Al-O-Ti (aluminum-oxygen-titanium) system." *Journal of Phase Equilibria* 23.6 (2002): 525-536.
- [72] Sutton, Michael A., Jean Jose Orteu, and Hubert Schreier. *Image correlation for shape, motion and deformation measurements: basic concepts, theory and applications*. Springer Science & Business Media, 2009.
- [73] Xing, H. Z., et al. "High-speed photography and digital optical measurement techniques for geomaterials: fundamentals and applications." *Rock Mechanics and Rock Engineering* 50.6 (2017): 1611-1659.
- [74] Pan, Bing. "Digital image correlation for surface deformation measurement: historical developments, recent advances and future goals." *Measurement Science and Technology* 29.8 (2018): 082001.
- [75] Pan, Bing, Huimin Xie, and Zhaoyang Wang. "Equivalence of digital image correlation criteria for pattern matching." *Applied optics* 49.28 (2010): 5501-5509.
- [76] Pan, Bing, et al. "Two-dimensional digital image correlation for in-plane displacement and strain measurement: a review." *Measurement science and technology* 20.6 (2009): 062001.
- [77] Khoo, Sze-Wei, Saravanan Karuppanan, and Ching-Seong Tan. "A review of surface deformation and strain measurement using two-dimensional digital image correlation." *Metrology and Measurement Systems* 23.3 (2016): 461-480.
- [78] Dong, Y. L., and B. Pan. "A review of speckle pattern fabrication and assessment for digital image correlation." *Experimental Mechanics* 57.8 (2017): 1161-1181.

- [79] Sutton, M. A., et al. "Determination of displacements using an improved digital correlation method." *Image and vision computing* 1.3 (1983): 133-139.
- [80] Schreier, Hubert W., Joachim R. Braasch, and Michael A. Sutton. "Systematic errors in digital image correlation caused by intensity interpolation." *Optical engineering* 39 (2000).
- [81] Knauss, Wolfgang G., Ioannis Chasiotis, and Ying Huang. "Mechanical measurements at the micron and nanometer scales." *Mechanics of materials* 35.3-6 (2003): 217-231.
- [82] Ibrahim, I. A., F. A. Mohamed, and E. J. Lavernia. "Particulate reinforced metal matrix composites—a review." *Journal of materials science* 26.5 (1991): 1137-1156.
- [83] Krell, Andreas, and Elmar Strassburger. "Order of influences on the ballistic resistance of armor ceramics and single crystals." *Materials Science and Engineering: A* 597 (2014): 422-430.
- [84] Su, Meike, et al. "Effect of heat treatment on microstructures and mechanical properties in a full lamellar PM TiAl alloy." *Materials Research* 15.3 (2012): 455-460.
- [85] Novoselova, T., S. Malinov, and W. Sha. "Experimental study of the effects of heat treatment on microstructure and grain size of a gamma TiAl alloy." *Intermetallics* 11.5 (2003): 491-499.
- [86] Xiang, Liuyi, et al. "Mechanical properties and microstructure of Al₂O₃/TiAl in situ composites doped with Cr₂O₃." *Materials Science and Engineering: A* 528.9 (2011): 3337-3341.
- [87] Schumacher, G., et al. "Microalloying effects in the oxidation of TiAl materials." *Intermetallics* 7.10 (1999): 1113-1120.
- [88] Ziegler, Tobias, Achim Neubrand, and Romana Piat. "Multiscale homogenization models for the elastic behaviour of metal/ceramic composites with lamellar domains." *Composites science and technology* 70.4 (2010): 664-670.

- [89] Bonora, Nicola, and Andrew Ruggiero. "Micromechanical modeling of composites with mechanical interface–Part II: Damage mechanics assessment." *Composites Science and Technology* 66.2 (2006): 323-332.
- [90] Cocks, Alan CF, Simon PA Gill, and Jingzhe Pan. "Modeling microstructure evolution in engineering materials." *Advances in Applied Mechanics*. Vol. 36. Elsevier, 1998. 81-162.
- [91] Tsang, H. T., C. G. Chao, and C. Y. Ma. "Effects of volume fraction of reinforcement on tensile and creep properties of in-situ TiB/Ti MMC." *Scripta Materialia* 37.9 (1997): 1359-1365.
- [92] Cseh, G., et al. "Indentation creep in a short fibre-reinforced metal matrix composite." *Materials Science and Engineering: A* 272.1 (1999): 145-151.
- [93] Talreja, Ramesh. "A conceptual framework for interpretation of MMC fatigue." *Materials Science and Engineering: A* 200.1-2 (1995): 21-28.
- [94] Majumdar, Bhaskar S., and Golam M. Newaz. "Constituent damage mechanisms in metal matrix composites under fatigue loading, and their effects on fatigue life." *Materials Science and Engineering: A* 200.1-2 (1995): 114-129.
- [3.1] Tsuda, Keiichi. "History of development of cemented carbides and cermet." SEI Technical Review 82 (2016): 16-20.
- [3.2] Mari, Daniele. (2001). Cermets and Hardmetals. Encyclopedia of Materials: Science and Technology. 1118-1123. 10.1016/B0-08-043152-6/00209-6.
- [3.3] J. Chevalier, L. Gremillard, Ceramics for medical applications: A picture for the next 20 years, Journal of the European Ceramic Society 29 (7) (2009) 1245 – 1255.
- [3.4] Wilkins, M. L., C. F. Cline, and C. A. Honodel. FOURTH PROGRESS REPORT OF LIGHT ARMOR PROGRAM. No. UCRL-50694. California Univ., Livermore. Lawrence Radiation Lab., 1969.

- [3.5] Landingham, R. L., and A. W. Casey. Final report of the light armor materials program. No. UCRL--51269. California Univ., 1972.
- [3.6] Strassburger, E., et al. "Behaviour of Al₂O₃-Al ceramic metal composites under projectile impact." *Le Journal de Physique IV* 10.PR9 (2000): Pr9-605.
- [3.7] Ischenko, A. N., et al. "Investigation of impact resistance of protective barriers made from cermets." *Russian Physics Journal* 58.9 (2016): 1347-1352.
- [3.8] Loiseau, J., et al. "Ballistic Response of Chromium/Chromium-Sulfide Cermets." *Journal of Dynamic Behavior of Materials* 1.3 (2015): 347-358.
- [3.9] Madheswaran, K., S. Sugumar, and B. Elamvazhudi. "Mechanical characterization of Aluminium–Boron carbide composites with influence of Calcium carbide particles." *International Journal of Emerging Technology and Advanced Engineering* 5.7 (2015): 492-496.
- [3.10] Rittel, D., N. Frage, and M. P. Dariel. "Dynamic mechanical and fracture properties of an infiltrated TiC-1080 steel cermet." *International journal of solids and structures* 42.2 (2005): 697-715.
- [3.11] Kaplan, W. D., et al. "Static and dynamic mechanical damage mechanisms in TiC-1080 steel cermets." *Scripta materialia* 51.1 (2004): 37-41.
- [3.12] Mandel, Kristin, Markus Radajewski, and Lutz Krüger. "Strain-rate dependence of the compressive strength of WC–Co hard metals." *Materials Science and Engineering: A* 612 (2014): 115-122.
- [3.13] Guden, M., and Ian W. Hall. "Quasi-static and dynamic compression behaviour of an FPTM alumina-reinforced aluminum metal matrix composite." *Journal of materials science* 33.13 (1998): 3285-3291.

- [3.14] Ramesh, K. T., and G. Ravichandran. "Dynamic behavior of a boron carbide aluminum cermet: experiments and observations." *Mechanics of Materials* 10.1-2 (1990): 19-29.
- [3.15] Blumenthal, W. R., G. T. Gray, and T. N. Claytor. "Response of aluminium-infiltrated boron carbide cermets to shock wave loading." *Journal of materials science* 29.17 (1994): 4567-4576.
- [3.16] Lu, Y. X., et al. "Microstructure and mechanical behaviour of a SiC particles reinforced Al–5Cu composite under dynamic loading." *Journal of materials processing technology* 94.2-3 (1999): 175-178.
- [3.17] Shen, Y. F., et al. "Properties and electronic structures of titanium aluminides–alumina composites from in-situ SHS process." *Materials Science and Engineering: A* 528.4-5 (2011): 2100-2105.
- [3.18] Xiang, Liuyi, et al. "Mechanical properties and microstructure of Al₂O₃/TiAl in situ composites doped with Cr₂O₃." *Materials Science and Engineering: A* 528.9 (2011): 3337-3341.
- [3.19] Zhang, Kun, et al. "The Microstructures and Mechanical Properties of V₂O₅-Doped Al₂O₃/TiAl In-Situ Composites by Reactive Hot Pressing Process." *Journal of materials engineering and performance* 22.12 (2013): 3933-3939.
- [3.20] Huy, Tran Duc, et al. "Microstructure and Mechanical Properties of TiAl₃/Al₂O₃ in situ Composite by Combustion Process." *Materials Transactions* 55.7 (2014): 1091-1093.
- [3.21] Kamali, Ali Reza, et al. "Production of TiAl (Ti₃Al)/Al₂O₃ Nanocomposite." *Journal of Nano Research*. Vol. 3. Trans Tech Publications, 2008.
- [3.22] Zhu, Jian Feng, Ji Qiang Gao, and Fen Wang. "Reaction Synthesis of TiAl-Al₂O₃ Composite." *Key Engineering Materials*. Vol. 336. Trans Tech Publications, 2007.

- [3.23] Gaus, Shaun P., et al. "Alumina–Aluminide Alloys (3A) Technology: II, Modeling of TixAl_y–Al₂O₃ Composites Formation." *Journal of the American ceramic society* 83.7 (2000): 1606-1612.
- [3.24] "Advanced-Alumina-Brochure." Coorstek.Inc, 2016.
<https://www.coorstek.com/media/1715/advanced-alumina-brochure.pdf>
- [3.25] "Ultra Nanoindentation Tester (UNHT³)." Anton Paar, www.anton-paar.com/en/products/details/ultra-nanoindentation-tester-unht3/.
- [3.26] ASTM C1425-15. Standard test method for monotonic compressive strength of advanced ceramics at ambient temperature, West Conshohocken (PA).
- [3.27] Hogan, James David, et al. "The effects of defects on the uniaxial compressive strength and failure of an advanced ceramic." *Acta Materialia* 102 (2016): 263-272.
- [3.28] Hu, Guangli, et al. "The compressive failure of aluminum nitride considered as a model advanced ceramic." *Journal of the Mechanics and Physics of Solids* 59.5 (2011): 1076-1093.
- [3.29] Chen, Weinong, and G. Ravichandran. "Dynamic compressive failure of a glass ceramic under lateral confinement." *Journal of the Mechanics and Physics of Solids* 45.8 (1997): 1303-1328.
- [3.30] Chen, Weinong W., and Bo Song. *Split Hopkinson (Kolsky) bar: design, testing and applications*. Springer Science & Business Media, 2010.
- [3.31] Xia, Kaiwen, and Wei Yao. "Dynamic rock tests using split Hopkinson (Kolsky) bar system—A review." *Journal of Rock Mechanics and Geotechnical Engineering* 7.1 (2015): 27-59.
- [3.32] Raghavan, V. "Al-Ni-Ti (aluminum-nickel-titanium)." *Journal of Phase Equilibria and Diffusion* 26.3 (2005): 268-272.

- [3.33] Marker, Martin CJ, et al. "Characterization of the Fe-rich corner of Al–Fe–Si–Ti." *Intermetallics* 39 (2013): 38-49.
- [3.34] Fadhil, Alaa Hassan, Mohsin A. Aswad, and Ahmed O. Al-Roubaiy. "THE STUDY OF THE THERMAL PROPERTIES OF SPINEL NICKEL ALUMINATE." *Iraqi journal of mechanical and material engineering* 16.1 (2016): 45-59.
- [3.35] Dreval, Liya, Tilo Zienert, and Olga Fabrichnaya. "Calculated phase diagrams and thermodynamic properties of the Al₂O₃–Fe₂O₃–FeO system." *Journal of Alloys and Compounds* 657 (2016): 192-214.
- [3.36] Chen, W., G. Ravichandran, and K. T. Ramesh. "A single pulse loading technique using the split Hopkinson pressure bar." *SM Report* (1995): 95-12.
- [3.37] Das, Siddhartha. "The Al-O-Ti (aluminum-oxygen-titanium) system." *Journal of Phase Equilibria* 23.6 (2002): 525-536.
- [3.38] Zhang, Kun, et al. "The Microstructures and Mechanical Properties of V₂O₅-Doped Al₂O₃/TiAl In-Situ Composites by Reactive Hot Pressing Process." *Journal of materials engineering and performance* 22.12 (2013): 3933-3939.
- [3.39] Travitzky, N., I. Gotman, and N. Claussen. "Alumina–Ti aluminide interpenetrating composites: microstructure and mechanical properties." *Materials Letters* 57.22-23 (2003): 3422-3426.
- [3.40] Forouzanmehr, N., F. Karimzadeh, and M. H. Enayati. "Synthesis and characterization of TiAl/ α -Al₂O₃ nanocomposite by mechanical alloying." *Journal of Alloys and Compounds* 478.1-2 (2009): 257-259.

- [3.41] Zhang, Houan, Ji-yong Yi, and Si-yong Gu. "Mechanical properties and microstructure of Ti (C, N) based cermets reinforced by nano-Si₃N₄ particles." *International Journal of Refractory Metals and Hard Materials* 29.2 (2011): 158-162.
- [3.42] Xiang, Liuyi, et al. "Mechanical properties and microstructure of Al₂O₃/TiAl in situ composites doped with Cr₂O₃." *Materials Science and Engineering: A* 528.9 (2011): 3337-3341.
- [3.43] Zhang, Houan, Siyong Gu, and Jiyong Yi. "Fabrication and properties of Ti (C, N) based cermets reinforced by nano-CBN particles." *Ceramics International* 38.6 (2012): 4587-4591.
- [3.44] Wu, Xiaodong, et al. "Development of adiabatic shearing bands in 7003-T4 aluminum alloy under high strain rate impacting." *Materials Science and Engineering: A* (2018).
- [3.45] Woodward, R. L., et al. "A study of fragmentation in the ballistic impact of ceramics." *International Journal of Impact Engineering* 15.5 (1994): 605-618.
- [3.46] Lankford Jr, James. "The role of dynamic material properties in the performance of ceramic armor." *International Journal of Applied Ceramic Technology* 1.3 (2004): 205-210.
- [3.47] Chen, Weinong, and Huiyang Luo. "Dynamic compressive testing of intact and damaged ceramics." *27th Annual Cocoa Beach Conference on Advanced Ceramics and Composites-A*. Vol. 268. John Wiley & Sons, 2009.
- [3.48] Huang, Feng-Lei, and Lian-Sheng Zhang. "Investigation on ballistic performance of armor ceramics against long-rod penetration." *Metallurgical and Materials Transactions A* 38.12 (2007): 2891-2895.
- [3.49] Lundberg, Patrik, René Renström, and Bengt Lundberg. "Impact of metallic projectiles on ceramic targets: transition between interface defeat and penetration." *International Journal of Impact Engineering* 24.3 (2000): 259-275.

- [3.50] Acharya, Saikat, et al. "Deformation and failure of alumina under high strain rate compressive loading." *Ceramics International* 41.5 (2015): 6793-6801.
- [3.51] Hogan, James David, et al. "On compressive brittle fragmentation." *Journal of the American Ceramic Society* 99.6 (2016): 2159-2169.
- [3.52] Luo, Huiyang, and Weinong Chen. "Dynamic compressive response of intact and damaged AD995 alumina." *International Journal of Applied Ceramic Technology* 1.3 (2004): 254-260.
- [3.53] Krell, Andreas, and Elmar Strassburger. "Order of influences on the ballistic resistance of armor ceramics and single crystals." *Materials Science and Engineering: A* 597 (2014): 422-430.
- [3.54] Kerper, Matthew J., et al. "Evaluation of tensile, compressive, torsional, transverse, and impact tests and correlation of results for brittle cermets." *Journal of Research of the National Bureau of Standards* 61.3 (1958): 149.
- [3.55] Johnson Jr, Aldie E. "Mechanical properties at room temperature of four cermets of tungsten carbide with cobalt binder." (1954).
- [3.56] Blumenthal, William R. "High strain rate compression testing of ceramics and ceramic composites." *Advances in Ceramic Armor: A Collection of Papers Presented at the 29th International Conference on Advanced Ceramics and Composites, Jan 23-28, 2005, Cocoa Beach, FL. Vol. 296.* John Wiley & Sons, 2009.
- [3.57] Frew, D. J., M. J. Forrester, and W. Chen. "Pulse shaping techniques for testing elastic-plastic materials with a split Hopkinson pressure bar." *Experimental mechanics* 45.2 (2005): 186.
- [3.58] Naghdabadi, R., M. J. Ashrafi, and J. Arghavani. "Experimental and numerical investigation of pulse-shaped split Hopkinson pressure bar test." *Materials Science and Engineering: A* 539 (2012): 285-293.

- [3.59] Vecchio, Kenneth S., and Fengchun Jiang. "Improved pulse shaping to achieve constant strain rate and stress equilibrium in split-Hopkinson pressure bar testing." *Metallurgical and materials transactions A* 38.11 (2007): 2655-2665.
- [3.60] Zhu, Dezhi, et al. "Dynamic deformation behavior of a high reinforcement content TiB₂/Al composite at high strain rates." *Materials Science and Engineering: A* 487.1-2 (2008): 536-540.
- [3.61] San Marchi, C., et al. "Quasi-static and dynamic compression of aluminum-oxide particle reinforced pure aluminum." *Materials Science and Engineering: A* 337.1-2 (2002): 202-211.
- [3.62] Appel, F. "An electron microscope study of mechanical twinning and fracture in TiAl alloys." *Philosophical Magazine* 85.2-3 (2005): 205-231.
- [3.63] Marketz, W. T., F. D. Fischer, and H. Clemens. "Deformation mechanisms in TiAl intermetallics—experiments and modeling." *International Journal of Plasticity* 19.3 (2003): 281-321.
- [3.64] Ji, Zong-Wei, et al. "Mapping deformation mechanisms in lamellar titanium aluminide." *Acta Materialia* 144 (2018): 835-843.
- [3.65] Guo, Wenqi, et al. "Nanoscale Twinned Ti-44Al-4Nb-1.5 Mo-0.007 Y Alloy Promoted by High Temperature Compression with High Strain Rate." *Metals* 8.8 (2018): 619.
- [4.1] Pickering, E. G., et al. "Effect of confinement on the static and dynamic indentation response of model ceramic and cermet materials." *International Journal of Impact Engineering* 110 (2017): 123-137.
- [4.2] San Marchi, C., et al. "Quasistatic and dynamic compression of aluminum-oxide particle reinforced pure aluminum." *Materials Science and Engineering: A* 337.1-2 (2002): 202-211.

- [4.3] Li, Yulong, K. T. Ramesh, and E. S. C. Chin. "Comparison of the plastic deformation and failure of A359/SiC and 6061-T6/Al₂O₃ metal matrix composites under dynamic tension." *Materials Science and Engineering: A* 371.1-2 (2004): 359-370.
- [4.4] Wilkins, M. L., C. F. Cline, and C. A. Honodel. *FOURTH PROGRESS REPORT OF LIGHT ARMOR PROGRAM*. No. UCRL-50694. California Univ., Livermore. Lawrence Radiation Lab., 1969.
- [4.5] Blumenthal, W. R., G. T. Gray, and T. N. Claytor. "Response of aluminium-infiltrated boron carbide cermets to shock wave loading." *Journal of Materials Science* 29.17 (1994): 4567-4576.
- [4.6] Schwarzkopf, Paul, and Richard Kieffer. *Refractory hard metals: borides, carbides, nitrides, and silicides; the basic constituents of cemented hard metals and their use as high-temperature materials*. Macmillan, 1953.
- [4.7] Ettmayer, Peter. "Hardmetals and cermets." *Annual Review of Materials Science* 19.1 (1989): 145-164.
- [4.8] Mari, D. "Cermets and hardmetals." (2014).
- [4.9] Li, Y., K. T. Ramesh, and E. S. C. Chin. "Viscoplastic deformations and compressive damage in an A359/SiCp metal–matrix composite." *Acta materialia* 48.7 (2000): 1563-1573.
- [4.10] Compton, B. G., and F. W. Zok. "Impact resistance of TiC-based cermets." *International Journal of Impact Engineering* 62 (2013): 75-87.
- [4.11] Jewell, P., et al. "Rate and microstructure influence on the fracture behavior of cemented carbides WC-Co and WC-Ni." *International Journal of Fracture* 208.1-2 (2017): 203-219.
- [4.12] Karamis, M. B., F. Nair, and A. Tasdemirci. "Analyses of metallurgical behavior of Al–SiCp composites after ballistic impacts." *Composite structures* 64.2 (2004): 219-226.

- [4.13] Travitzky (2012) Processing of ceramic–metal composites, *Advances in Applied Ceramics*, 111:5-6, 286-300, DOI: 10.1179/1743676111Y.0000000073
- [4.14] Taya, Minoru, and Richard J. Arsenault. *Metal matrix composites: thermomechanical behavior*. Elsevier, 2016.
- [4.15] Johnson Jr, Aldie E. "Mechanical properties at room temperature of four cermets of tungsten carbide with cobalt binder." (1954).
- [4.16] Kerper, Matthew J., et al. "Evaluation of tensile, compressive, torsional, transverse, and impact tests and correlation of results for brittle cermets." *Journal of Research of the National Bureau of Standards* 61.3 (1958): 149.
- [4.17] Rittel, D., N. Frage, and M. P. Dariel. "Dynamic mechanical and fracture properties of an infiltrated TiC-1080 steel cermet." *International journal of solids and structures* 42.2 (2005): 697-715.
- [4.18] Ramesh, K. T., and G. Ravichandran. "Dynamic behavior of a boron carbide aluminum cermet: experiments and observations." *Mechanics of Materials* 10.1-2 (1990): 19-29.
- [4.19] Crouch, Ian G. "Body Armour – New Materials, New Systems." *Defence Technology*, Elsevier Ltd, 2019, doi:10.1016/j.dt.2019.02.002.
- [4.20] Meier, G. H., et al. "Environmental behaviour of intermetallic materials." *Structural Intermetallics*, R. Darolia, J Lewandowski, CT Liu, PL Martin, DB Miracle, MV Nathal (editors), TMS, Warrendale 861 (1993).
- [4.21] Liang, Yongfeng, and Junpin Lin. "Fabrication and Properties of γ -TiAl Sheet Materials: A Review." *JOM*, vol. 69, no. 12, 2017, pp. 2571–75, doi:10.1007/s11837-017-2551-z.
- [4.22] Djanarthany, S., J-C. Viala, and J. Bouix. "An overview of monolithic titanium aluminides based on Ti₃Al and TiAl." *Materials chemistry and physics* 72.3 (2001): 301-319.

- [4.23] Appel, F., and R. Wagner. "Microstructure and deformation of two-phase γ -titanium aluminides." *Materials science and engineering: r: reports* 22.5 (1998): 187-268.
- [4.24] "Advanced-Alumina-Brochure." Coorstek. Inc, 2016.
<https://www.coorstek.com/media/1715/advanced-alumina-brochure.pdf>
- [4.25] Rosenberg, Zvi, and Erez Dekel. *Terminal ballistics*. Berlin: Springer, 2012.
- [4.26] Weeks, Carrell Elizabeth. *Evaluation of a gamma titanium aluminide for hypersonic structural applications*. Diss. Georgia Institute of Technology, 2005.
- [4.27] Levashov, E. A., et al. "Self-propagating high-temperature synthesis of advanced materials and coatings." *International Materials Reviews* 62.4 (2017): 203-239.
- [4.28] Cai, Z. H., and D. L. Zhang. "Sintering behaviour and microstructures of Ti (Al, O)/Al₂O₃, Ti₃Al (O)/Al₂O₃ and TiAl (O)/Al₂O₃ in situ composites." *Materials Science and Engineering: A* 419.1-2 (2006): 310-317.
- [4.29] Taotao, Ai. "Microstructure and mechanical properties of in-situ synthesized Al₂O₃/TiAl composites." *Chinese Journal of Aeronautics* 21.6 (2008): 559-564.
- [4.30] Gaus, Shaun P., et al. "Alumina–Aluminide Alloys (3A) Technology: II, Modeling of TixAly–Al₂O₃ Composites Formation." *Journal of the American ceramic society* 83.7 (2000): 1606-1612.
- [4.31] Kamali, Ali Reza, et al. "Production of TiAl (Ti₃Al)/Al₂O₃ Nanocomposite." *Journal of Nano Research*. Vol. 3. Trans Tech Publications, 2008.
- [4.32] Forouzanmehr, N., F. Karimzadeh, and M. H. Enayati. "Synthesis and characterization of TiAl/ α -Al₂O₃ nanocomposite by mechanical alloying." *Journal of Alloys and Compounds* 478.1-2 (2009): 257-259.

- [4.33] Shen, Y. F., et al. "Properties and electronic structures of titanium aluminides–alumina composites from in-situ SHS process." *Materials Science and Engineering: A* 528.4-5 (2011): 2100-2105.
- [4.34] Lapin, J., L. Ondrůš, and O. Bajana. "Effect of Al₂O₃ particles on mechanical properties of directionally solidified intermetallic Ti–46Al–2W–0.5 Si alloy." *Materials Science and Engineering: A* 360.1-2 (2003): 85-95.
- [4.35] Claussen, N., D. E. Garcia, and R. Janssen. "Reaction sintering of alumina-aluminide alloys (3A)." *Journal of materials research* 11.11 (1996): 2884-2888.
- [4.36] Zhu, Jian Feng, Ji Qiang Gao, and Fen Wang. "Reaction Synthesis of TiAl–Al₂O₃ Composite." *Key Engineering Materials*. Vol. 336. Trans Tech Publications, 2007.
- [4.37] Travitzky, N., I. Gotman, and N. Claussen. "Alumina–Ti aluminide interpenetrating composites: microstructure and mechanical properties." *Materials Letters* 57.22-23 (2003): 3422-3426.
- [4.38] Li, H. Y., P. Motamedi, and J. D. Hogan. "Characterization and mechanical testing on novel (γ + α 2)–TiAl/Ti₃Al/Al₂O₃ cermet." *Materials Science and Engineering: A* 750 (2019): 152-163.
- [4.39] Farbaniec, L., et al. "Damage evolution of hot-pressed boron carbide under confined dynamic compression." *International Journal of Impact Engineering* 99 (2017): 75-84.
- [4.40] "Global Scientific Services | We Know How." EAG Laboratories, www.eag.com/.
- [4.41] P. Motamedi, K. Bosnick, K. Cadien and J. D. Hogan, *Adv. Mater. Interfaces*, 2018, 1800957, 1800957.
- [4.42] P. Motamedi, K. Bosnick, K. Cui, K. Cadien and J. D. Hogan, *ACS Appl. Mater. Interfaces*, 2017, 9, 24722–24730.
- [4.43] Kolsky, H., 1963. *Stress Waves in Solids*. Dover Publications, New York.

- [4.44] Staehler, James M., et al. "Testing of high-strength ceramics with the split Hopkinson pressure bar." *Journal of the American Ceramic Society* 76.2 (1993): 536-538.
- [4.45] Swab, Jeffrey J., et al. "Static and dynamic compression strength of hot-pressed boron carbide using a dumbbell-shaped specimen." *Journal of Materials Science* 52.17 (2017): 10073-10084.
- [4.46] Bin, L. I. U., et al. "Compressive behavior of high particle content B₄C/Al composite at elevated temperature." *Transactions of Nonferrous Metals Society of China* 23.10 (2013): 2826-2832.
- [4.47] Tan, Z. H., et al. "The compressive properties of 2024Al matrix composites reinforced with high content SiC particles at various strain rates." *Materials Science and Engineering: A* 489.1-2 (2008): 302-309.
- [4.48] Hu, Guangli, et al. "The compressive failure of aluminum nitride considered as a model advanced ceramic." *Journal of the Mechanics and Physics of Solids* 59.5 (2011): 1076-1093.
- [4.49] Pan, Bing, et al. "Two-dimensional digital image correlation for in-plane displacement and strain measurement: a review." *Measurement science and technology* 20.6 (2009): 062001.
- [4.50] Schreier, Hubert, Jean-José Orteu, and Michael A. Sutton. *Image correlation for shape, motion and deformation measurements: Basic concepts, theory and applications*. Vol. 1. Boston, MA: Springer-Verlag US, 2009.
- [4.51] Khoo, Sze-Wei, et al. "A Review of Surface Deformation and Strain Measurement Using Two-Dimensional Digital Image Correlation." *Metrology and Measurement Systems*, vol. 23, no. 3, Jan. 2016, doi:10.1515/mms-2016-0028.
- [4.52] Vic-2D, Correlated Solutions Inc., Irmo, South Carolina. URL (<http://correlatedsolutions.com/vic-2d/>).

- [4.53] Sutton, Michael A., et al. "The effect of out-of-plane motion on 2D and 3D digital image correlation measurements." *Optics and Lasers in Engineering* 46.10 (2008): 746-757.
- [4.54] Lionello, Giacomo & Cristofolini, Luca. (2014). A practical approach to optimizing the preparation of speckle patterns for digital-image correlation. *Measurement Science and Technology*. 25. 107001. 10.1088/0957-0233/25/10/107001.
- [4.55] Jerabek, Michael, Zoltan Major, and Reinhold W. Lang. "Strain determination of polymeric materials using digital image correlation." *Polymer Testing* 29.3 (2010): 407-416.
- [4.56] Pan, B. (2013). Bias error reduction of digital image correlation using Gaussian pre-filtering. *Optics and Lasers in Eng.*, 51(10), 1161–1167.
- [4.57] Kaplan, W. D., et al. "Static and dynamic mechanical damage mechanisms in TiC-1080 steel cermets." *Scripta materialia* 51.1 (2004): 37-41.
- [4.58] Li, Wei, et al. "Texture evolution, phase transformation mechanism and nanohardness of selective laser melted Ti-45Al-2Cr-5Nb alloy during multi-step heat treatment process." *Intermetallics* 85 (2017): 130-138.
- [4.59] Li, Y., et al. "Investigation of aluminum-based nanocomposites with ultra-high strength." *Materials Science and Engineering: A* 527.1-2 (2009): 305-316.
- [4.60] Lapin, J., T. Pelachová, and O. Bajana. "High temperature deformation behaviour and microstructure of cast in-situ TiAl matrix composite reinforced with carbide particles." *Journal of Alloys and Compounds* 797 (2019): 754-765.
- [4.61] Domnich, Vladislav, et al. "Boron carbide: structure, properties, and stability under stress." *Journal of the American Ceramic Society* 94.11 (2011): 3605-3628.

- [4.62] Eshchenko, R. N., et al. "Structural transformations in the deuterium-containing intermetallic compound (Ti₃Al) D1.2 induced by high-pressure torsion." *The Physics of Metals and Metallography* 107.6 (2009): 594-600.
- [4.64] Mandel, Kristin, Markus Radajewski, and Lutz Krüger. "Strain-rate dependence of the compressive strength of WC–Co hard metals." *Materials Science and Engineering: A* 612 (2014): 115-122.
- [4.65] Wang, B. P., et al. "Strain rate-dependent compressive deformation and failure behavior of porous SiC/Ti-based metallic glass composite." *Materials Science and Engineering: A* 609 (2014): 53-59.
- [4.66] Zhu, Dezhi, et al. "Dynamic deformation behavior of a high reinforcement content TiB₂/Al composite at high strain rates." *Materials Science and Engineering: A* 487.1-2 (2008): 536-540.
- [4.67] Klein, B., et al. "Dynamic response of ceramic-metal composites: The TiC-Steel system." *Journal of applied physics* 93.2 (2003): 968-976.
- [4.68] Ashby, M. F., and C. G. Sammis. "The damage mechanics of brittle solids in compression." *Pure and Applied Geophysics* 133.3 (1990): 489-521.
- [4.69] Holland, Chance C., and Robert M. McMeeking. "The influence of mechanical and microstructural properties on the rate-dependent fracture strength of ceramics in uniaxial compression." *International Journal of Impact Engineering* 81 (2015): 34-49.
- [4.70] Johnson, Gordon R., Timothy J. Holmquist, and Stephen R. Beissel. "Response of aluminum nitride (including a phase change) to large strains, high strain rates, and high pressures." *Journal of Applied Physics* 94.3 (2003): 1639-1646.

- [4.71] Güden, Mustafa, et al. "Effect of strain rate on the compressive mechanical behavior of a continuous alumina fiber reinforced ZE41A magnesium alloy based composite." *Materials Science and Engineering: A* 425.1-2 (2006): 145-155.
- [4.72] Vogt, R., et al. "High strain rate deformation and resultant damage mechanisms in ultrafine-grained aluminum matrix composites." *Materials Science and Engineering: A* 527.21-22 (2010): 5990-5996.
- [4.73] Maloy, S. A., and G. T. Gray III. High strain rate deformation of Ti-48Al-2Cr-2Nb in the duplex morphology. No. LA-UR-95-739; CONF-950201-15. Los Alamos National Lab., NM (United States), 1995.
- [4.74] Semiatin, S. L., et al. "Plastic-flow behavior and microstructural development in a cast alpha-two titanium aluminide." *Metallurgical Transactions A* 23.1 (1992): 295-305.
- [4.75] Zeng, Shangwu, et al. "Flow behavior and processing maps of Ti-44.5 Al-3.8 Nb-1.0 Mo-0.3 Si-0.1 B alloy." *Journal of Alloys and Compounds* 698 (2017): 786-793.
- [4.76] Wu, Xiaodong, et al. "Development of adiabatic shearing bands in 7003-T4 aluminum alloy under high strain rate impacting." *Materials Science and Engineering: A* 732 (2018): 91-98.
- [4.77] Luo, Huiyang, and Weinong Chen. "Dynamic compressive response of intact and damaged AD995 alumina." *International Journal of Applied Ceramic Technology* 1.3 (2004): 254-260.
- [4.78] Lankford Jr, James. "The role of dynamic material properties in the performance of ceramic armor." *International Journal of Applied Ceramic Technology* 1.3 (2004): 205-210.
- [4.79] Krell, Andreas, and Elmar Strassburger. "Order of influences on the ballistic resistance of armor ceramics and single crystals." *Materials Science and Engineering: A* 597 (2014): 422-430
- [4.80] Jiao, T., et al. "High rate response and dynamic failure of structural ceramics." *International Journal of applied ceramic technology* 1.3 (2004): 243-253.

- [4.81] Blumenthal, William R. "High strain rate compression testing of ceramics and ceramic composites." *Advances in Ceramic Armor: A Collection of Papers Presented at the 29th International Conference on Advanced Ceramics and Composites, Jan 23-28, 2005, Cocoa Beach, FL.* Vol. 296. John Wiley & Sons, 2009.
- [4.82] Chen, Weinong W., et al. "Dynamic fracture of ceramics in armor applications." *Journal of the American Ceramic Society* 90.4 (2007): 1005-1018.
- [4.83] Behm, Nathan, et al. "Quasi-static and high-rate mechanical behavior of aluminum-based MMC reinforced with boron carbide of various length scales." *Materials Science and Engineering: A* 650 (2016): 305-316.
- [4.84] Nawale, S. P., R. T. Vyavahare, and A. S. Aradhye. "High Strain Rate Response of A356/Al₂O₃ Aluminum Alloy MMCs Using Ls-Dyna." *Procedia Engineering* 173 (2017): 1967-1974.
- [4.85] Hong, S. I., and G. T. Gray. "Dynamic mechanical response of a 1060 Al/Al₂O₃ composite." *Journal of materials science* 29.11 (1994): 2987-2992.
- [4.86] Hong, S. I., G. T. Gray III, and J. J. Lewandowski. "Dynamic deformation behavior of Al-Zn-Mg-Cu alloy matrix composites reinforced with 20 Vol.% SiC." *Acta metallurgica et materialia* 41.8 (1993): 2337-2351.
- [4.87] Bao, G., and Z. Lin. "High strain rate deformation in particle reinforced metal matrix composites." *Acta materialia* 44.3 (1996): 1011-1019.
- [4.88] Guo, Q., et al. "SEM and TEM characterization of the microstructure of post-compressed TiB₂/2024Al composite." *Micron* 43.2-3 (2012): 380-386.
- [4.89] Lankford, J. "Mechanisms Responsible for Strain-Rate-Dependent Compressive Strength in Ceramic Materials." *Journal of the American Ceramic Society* 64.2 (1981): C-33.

- [4.90] Kimberley, J., K. T. Ramesh, and N. P. Daphalapurkar. "A scaling law for the dynamic strength of brittle solids." *Acta Materialia* 61.9 (2013): 3509-3521.
- [4.91] Lankford, J. A. M. E. S., and C. R. Blanchard. "Fragmentation of brittle materials at high rates of loading." *Journal of materials science* 26.11 (1991): 3067-3072.
- [4.92] Finot, M., et al. "Micromechanical modeling of reinforcement fracture in particle-reinforced metal-matrix composites." *Metallurgical and Materials Transactions A* 25.11 (1994): 2403-2420.
- [4.93] Basak, A. K., Alokesh Pramanik, and Mohammad Nazrul Islam. "Failure mechanisms of nanoparticle reinforced metal matrix composite." *Advanced Materials Research*. Vol. 774. Trans Tech Publications, 2013.
- [4.94] Needleman, Alan. "A continuum model for void nucleation by inclusion debonding." *Journal of applied mechanics* 54.3 (1987): 525-531.
- [4.95] Ai, Taotao, et al. "Microstructural and mechanical properties of dual Ti₃AlC₂-Ti₂AlC reinforced TiAl composites fabricated by reaction hot pressing." *Ceramics International* 40.7 (2014): 9947-9953.
- [4.96] Zhang, H., K. T. Ramesh, and E. S. C. Chin. "Effects of interfacial debonding on the rate-dependent response of metal matrix composites." *Acta materialia* 53.17 (2005): 4687-4700.
- [4.97] Needleman, A. "An analysis of decohesion along an imperfect interface." *Non-Linear Fracture*. Springer, Dordrecht, 1990. 21-40.
- [4.98] Lee, Hyungsoo, et al. "Effects of SiC particulate size on dynamic compressive properties in 7075-T6 Al-SiCp composites." *Materials Science and Engineering: A* 738 (2018): 412-419.
- [4.99] Yanjun, Hao, et al. "Investigation on dynamic properties and failure mechanisms of Ti-47Al-2Cr-2Nb alloy under uniaxial dynamic compression at a temperature range of 288 K-773 K." *Journal of Alloys and Compounds* 649 (2015): 122-127.

- [4.100] Cui, Ning, et al. "Hot deformation behavior and dynamic recrystallization of a β -solidifying TiAl alloy." *Materials Science and Engineering: A* 652 (2016): 231-238.
- [4.101] Wang, Bingfeng, et al. "Mechanical properties and microstructure in a fine grained Ti-5Al-5Mo-5V-1Cr-1Fe titanium alloy deformed at a high strain rate." *Materials Science and Engineering: A* 736 (2018): 202-208.
- [4.102] Wu, Yang, et al. "Dynamic recrystallization and texture evolution of Ti-22Al-25Nb alloy during plane-strain compression." *Journal of Alloys and Compounds* 749 (2018): 844-852.
- [4.103] Simkin, B. A., et al. "Crack opening due to deformation twin shear at grain boundaries in near- γ TiAl." *Intermetallics* 15.1 (2007): 55-60.
- [4.104] Edwards, Thomas Edward James, et al. "Deformation of lamellar TiAl alloys by longitudinal twinning." *Scripta Materialia* 118 (2016): 46-50.
- [4.105] Appel, F. "An electron microscope study of mechanical twinning and fracture in TiAl alloys." *Philosophical Magazine* 85.2-3 (2005): 205-231.
- [4.106] Beran, Premysl, et al. "Complex investigation of deformation twinning in γ -TiAl by TEM and neutron diffraction." *Journal of the Mechanics and Physics of Solids* 95 (2016): 647-662.
- [4.107] Guo, Wenqi, et al. "Nanoscale Twinned Ti-44Al-4Nb-1.5 Mo-0.007 Y Alloy Promoted by High Temperature Compression with High Strain Rate." *Metals* 8.8 (2018): 619.
- [4.108] Humphreys, Frederick John, and Max Hatherly. *Recrystallization and related annealing phenomena*. Elsevier, 2012.
- [4.109] Huang, K., and R. E. Logé. "A review of dynamic recrystallization phenomena in metallic materials." *Materials & Design* 111 (2016): 548-574.
- [4.110] Randle, Valerie, and Olaf Engler. *Introduction to texture analysis: macrotexture, microtexture and orientation mapping*. CRC press, 2014.

- [4.111] Kocks, U. Fred, et al. Texture and anisotropy: preferred orientations in polycrystals and their effect on materials properties. Cambridge university press, 2000.
- [4.112] Sankaran, A., et al. "Texture and microstructure evolution during tempering of gamma-massive phase in a TiAl-based alloy." *Intermetallics* 17.12 (2009): 1007-1016.
- [4.113] Huang, Feng-Lei, and Lian-Sheng Zhang. "Investigation on ballistic performance of armor ceramics against long-rod penetration." *Metallurgical and Materials Transactions A* 38.12 (2007): 2891-2895.
- [4.114] Savio, S. G., et al. "An experimental study on ballistic performance of boron carbide tiles." *International Journal of Impact Engineering* 38.7 (2011): 535-541.
- [4.115] Mukasey, M. B., J. L. Sedgwick, and D. W. Hagy. "Ballistic Resistance of Body Armor, NIJ Standard-0101.06." US Department of Justice (www.ojp.usdoj.gov/nij) (2008).
- [4.116] Villanueva, G. Reyes, and W. J. Cantwell. "The high velocity impact response of composite and FML-reinforced sandwich structures." *Composites Science and Technology* 64.1 (2004): 35-54.
- [4.117] Rozenberg, Z., and Y. Yeshurun. "The relation between ballistic efficiency and compressive strength of ceramic tiles." *International journal of impact engineering* 7.3 (1988): 357-362.
- [4.118] Neshpor, V. C., G. P. Zaitsev, and A. L. Maystrenko. "Armour ceramics ballistic efficiency evaluation." *Abstr. of 8th CIMTEC World Ceramics Congress Forum New Materials (Florenca, Italy). –1994.–P. Vol. 102. 1994.*
- [4.119] Launey, Maximilien E., and Robert O. Ritchie. "On the fracture toughness of advanced materials." *Advanced Materials* 21.20 (2009): 2103-2110.

- [4.120] Quinn, George D., et al. "Fracture toughness of advanced ceramics at room temperature." *Journal of research of the National Institute of Standards and Technology* 97.5 (1992): 579.
- [4.121] Silva, M. V., et al. "Alumina-based ceramics for armor application: mechanical characterization and ballistic testing." *Journal of Ceramics* 2014 (2014).
- [4.122] Yang, Mijia, and Pizhong Qiao. "High energy absorbing materials for blast resistant design." *Blast Protection of Civil Infrastructures and Vehicles Using Composites*. Woodhead Publishing, 2010. 88-119.
- [4.123] Alizadeh, Ali, Mohammad Maleki, and Alireza Abdollahi. "Preparation of super-high strength nanostructured B₄C reinforced Al-2Cu aluminum alloy matrix composites by mechanical milling and hot press method: microstructural, mechanical and tribological characterization." *Advanced Powder Technology* 28.12 (2017): 3274-3287.
- [4.124] Pötschke, J., et al. "Grain growth inhibition in ultrafine hardmetals." *International Journal of Refractory Metals and Hard Materials* 66 (2017): 95-104.
- [4.125] Liu, N., et al. "Microstructure, hardness and fracture toughness of TiC based cermets with nano TiN powders addition." *Powder metallurgy* 50.2 (2007): 142-147.
- [4.126] Gopal Krishna, U. B., K. V. Sreenivas Rao, and B. Vasudeva. "Effect of boron carbide reinforcement on aluminium matrix composites." *International Journal of Metallurgical & Materials Science and Engineering (IJMMSE) ISSN* (2013): 41-48.
- [4.127] Joardar, J., S. W. Kim, and S. Kang. "Effect of nanocrystalline binder on the microstructure and mechanical properties of ultrafine Ti (CN) cermets." *Materials Science and Engineering: A* 360.1-2 (2003): 385-389.
- [4.128] Zheng, Yong, et al. "Effect of nano addition on the microstructures and mechanical properties of Ti (C, N)-based cermets." *Ceramics International* 31.1 (2005): 165-170.

- [4.129] Landingham, R. L., and A. W. Casey. Final report of the light armor materials program. No. UCRL--51269. California Univ., 1972.
- [4.130] Fukutomi, Hiroshi, et al. "Mechanism of texture formation during dynamic recrystallization of Ti-49 mol% Al." *materials transactions, jim* 35.11 (1994): 794-799.
- [4.131] Hogan, James D., et al. "The effects of microstructure and confinement on the compressive fragmentation of an advanced ceramic." *Journal of the American Ceramic Society* 98.3 (2015): 902-912.
- [4.132] Forquin, Pascal, et al. "Effect of aluminum reinforcement on the dynamic fragmentation of SiC ceramics." *International journal of impact engineering* 28.10 (2003): 1061-1076.
- [4.133] Huy, Tran Duc, et al. "Microstructure and Mechanical Properties of TiAl₃/Al₂O₃ in situ Composite by Combustion Process." *Materials Transactions* 55.7 (2014): 1091-1093.
- [4.134] Boyce, Brad L., and Thomas B. Crenshaw. "Servohydraulic methods for mechanical testing in the sub-Hopkinson rate regime up to strain rates of 500 1/s." Sandia National Laboratories Report, SAND2005-5678 (2005): 1-16.
- [4.135] Mallick, D. D., et al. "A Simple Dual-Beam Time-Multiplexed Photon Doppler Velocimeter for Pressure-Shear Plate Impact Experiments." *Experimental Mechanics* 59.1 (2019): 41-49.

Appendix A: Self-Propagating High-Temperature Synthesis (SHS): A Brief Summary

The development of high-efficiency and energy-saving fabrication techniques is of great demand nowadays. Some conventional manufacturing methods, including milling and furnace-based technologies usually takes hours or even days to complete the process. The SHS process, on the other hand, takes only seconds to generate the final product. It has attracted significant attentions recently as a relatively novel and simple method for making certain advanced ceramics, intermetallic compounds, and composites [68].

The general definition of an SHS process, given by A.G. Merzhanov [69], is that: *SHS is a self-sustained combustion process that yields practically valuable compounds and materials. Thus, practically, any self-sustained chemical reactions, including synthesis from some elementary powders, reactions from solid compounds, and thermite-type reactions can be used in an SHS process for material manufacturing* [70]. The SHS process is called “energy-saving” because one self-sustained reaction does not require any continuous energy inputs, and the whole synthesis is completed based on the energy released from the highly exothermic reactions between the reactants [68]. There are essentially two ways to initiate an SHS process: 1. By uniform pre-heating of the whole sample until an exothermic reaction starts simultaneously in every point (volume combustion mode); and 2. By local heating of the reactants to initiate the reaction in a small volume of the sample with consequent self-sustained propagation of the exothermic combustion wave

throughout the entire body (self-propagating wave mode) [70]. In both cases, the temperature scale vs. time scale is significantly different (i.e., much higher vs. much smaller) than the conventional fabrication methods that some unique materials can be formed through this process.

One such material is the ultrafine-grained or nano-grained material, providing that the process parameters (i.e., temperature, initial powder ratio, powder size) are carefully tuned [71]. According to Sytshev and Merzhanov [71], there are mainly three ways of producing nanostructured materials: 1. Solid flame combustion “solid + solid” systems; 2. Gas-phase SHS; and 3. Combustion of “solid + gas” systems. The focus in this appendix will be on the “solid + solid” systems, from which the TiAl/Ti₃Al-Al₂O₃ cermet in this thesis is made from. The diffusive combustion process in a “solid + solid” system often requires near-size reactants compared to the grain size of the final product. In other words, in order to produce an ultrafine-grained or nano-grained composite, the reactants (i.e., initial powders) have to be either ultrafine-grained or nano-grained themselves [71]. Quite often the commercially available elementary powder will not come with such small sizes; therefore, several pre-sintering steps could be taken to reduce the powder size, for example: 1. Pre-compaction of the initial powders; 2. Pre-milling of the initial powders to form a green mixture; and 3. Thermal explosion of the initial mixtures. Detailed reviews on the formation of nanostructured materials using the SHS process can be referred to Sytshev and Merzhanov [71], and a detailed review on the process parameters can be referred to Mossino [68]. The TiAl/Ti₃Al-Al₂O₃ cermet studied in the thesis, as mentioned above, is made from a “solid + solid” SHS system with initial powders being Aluminum (Al) and Titanium dioxide (TiO₂). Composites including an oxide-based ceramic phase (i.e., Al₂O₃ in this case) has drawn particular attentions because of their high hardness, oxidation resistance, chemical and thermal stability, and corrosion resistance in the impact and wear applications [70]. By combining some interpenetrating

metallic or intermetallic phases into the oxide-based ceramics, the toughness (which is a drawback of advanced ceramics) can be greatly improved. The TiAl/Ti₃Al-Al₂O₃ is an example for which a combination of improved toughness and flexural strength with high stiffness and strength is achieved.

Shen et al. [51] studied the SHS process to form a similar two-phase TiAl/Ti₃Al-Al₂O₃ cermet in detail. The chemical reactions from the initial powders of aluminum and titanium dioxide to from the final composite is documented as follows [51]:



This is different from the ideally stoichiometrically-matched reaction, where:



This is because the possibility of forming two units of Ti-Al phase to keep a balanced amount between elements. Also, from the phase diagram of Ti-Al [72], the γ -based TiAl and the α_2 -based Ti₃Al lamellae phases may coexist as the temperature is in the range of 500 – 1125 °C (when Al content was ~ 35–50 at.%). The existence of the three phases in the cermet can be proven from the XRD spectrum plot (see Fig. 3.4 in Chapter 3). A reaction model (see Fig. A.1) is also proved in Shen et al. [51].

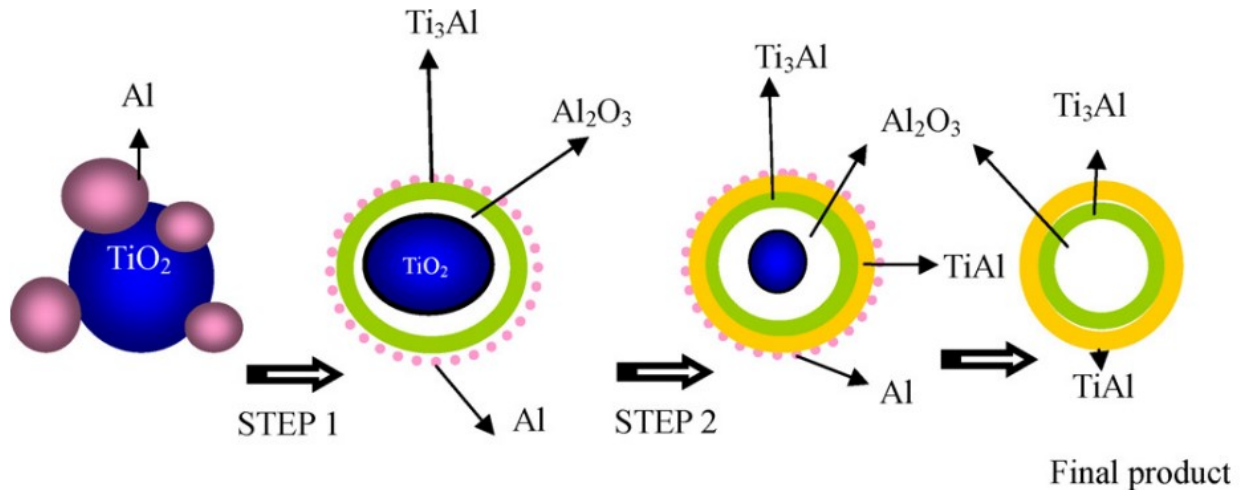


Figure A.1: Reaction model of 3TiO₂-7Al powder at high temperatures. This image is taken from Shen et al. [51].

Some critical conditions were identified in Shen et al. [51] for maintaining a good self-sustained reaction process: 1. A molar ratio TiO₂:Al = 3:7; and 2. An adiabatic temperature of 1733 K (i.e., the melting temperature of TiAl, which exceeds 1700 K). The SHS process will be greatly compromised if these conditions are deviated (e.g., excess Al in the initial mixture) due to the lack of energy to sustain the combustion wave propagation. Detailed explanation and experimental investigation can be referred to Shen et al. [51]. In short, the SHS process remains an open area of investigation if this is to be implemented into industrial-scale mass manufacturing. Even though some have been employed in the field of specialized ceramic composite pipeline (e.g., Sunny Steel Enterprise Ltd, China), the potential of SHS can be further developed if some improvements can be made in standardizing the process parameters and lowering the pre-sintering cost.

Appendix B: Digital Image Correlation

(DIC): A Brief Summary

B.1 A Brief Summary of the DIC theory

Digital image correlation often refers to the class of non-contact techniques that use digital images analysis to extract full-field shape, deformation and/or motion measurements [72]. Three major types of DIC technique have been developed from the advancement in image processing and patching methods, and this includes: 1. 2D-DIC for in-plane measurements; 2. 3D-DIC for surface 3D deformation of both curved and in-plane objects (also referred to as stereo-DIC), and 3. Digital volume correlation (DVC) for internal full-field deformation of opaque solids or biological tissues [73]. Schematics of the setups can be referred to Pan [74]. In this thesis, 2D-DIC has been used to obtain the in-plane surface strain maps for both quasi-static and dynamic experiments, and hence, it is the focus of this Appendix.

The principle of DIC is to match the same set of pixels in two images recorded before and after the deformation of an object [73]. For a series of images extracted from a video, the first image (i.e., undeformed state of the object) is often referred to as the “reference image,” and the subsequent images are referred to as the “deformed images.” Figure B.1 shows an example of a matching performed in a typical DIC algorithm [75]. The image on the left is the “reference image,” where a subset (red box) is defined in the image with the center pixel position at point P . In order to obtain the displacement of this subset, the DIC algorithm searches the position of point P (denoted as P') in the deformed image (image on the right) by finding the similarities in grayscale intensity level. One of the major constituents of a DIC algorithm is the “correlation criterion”,

from which an evaluation of the degree of similarities between the reference and deformed subsets is performed at a defined searching area (yellow box). Once the position and displacement of P' are located, then other pixels can be obtained by some shape functions.

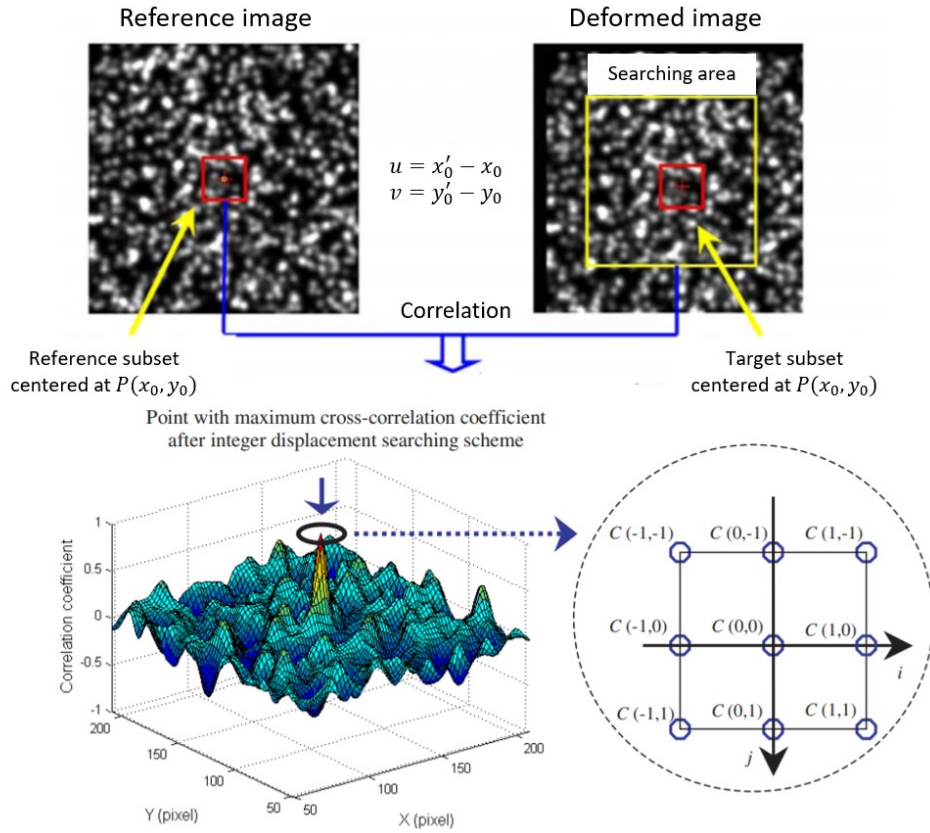


Figure B.1: Schematic of a reference subset before deformation and a target subset after deformation. The center position of the target subset is obtained through searching the peak position of the distribution of the correlation coefficient. The insert shows a 3 x 3 local discrete correlation coefficient distribution, where $C(0, 0)$ is the point with the maximum correlation coefficient obtained from an integer pixel displacement searching scheme. This image is taken from Pan [75, 76].

For a typical DIC analysis, the displacement is described with respect to the undeformed or reference geometry (image); therefore, a Lagrangian description of the deformed body is given [77]. Hence, the displacement of material surface regarding the subsets can be written as [77]:

$$\vec{D}(x, y) = u(x, y)\hat{i} + v(x, y)\hat{j} \quad (1)$$

It is assumed that the light intensity level is only a function of the change in the displacement field, no other noise from the environment is considered. The above equation can be further written as [77]:

$$I_f(x_i + u, y_i + v) = I_i(x_i, y_i) + \Delta I(x_i + \Delta u, y_i + \Delta v) + I_n \quad (2)$$

where I_n is the sum of effects on intensity except for displacement, I_f is the final intensity level, and I_i is the initial intensity level (undeformed). With this information, first-order shape functions are used to locate the initially square subset in the deformed image. The first-order shape functions can be expressed as [77]:

$$x' = x + u + \frac{\partial u}{\partial x} dx + \frac{\partial u}{\partial y} dy \quad (3)$$

$$y' = y + v + \frac{\partial v}{\partial x} dx + \frac{\partial v}{\partial y} dy \quad (4)$$

(x, y) and (x', y') are the coordinates in the reference and deformed images. Here, u and v are the rigid body translation, $\frac{\partial u}{\partial x}$ and $\frac{\partial v}{\partial y}$ are the normal strains, $\frac{\partial u}{\partial y}$ and $\frac{\partial v}{\partial x}$ are the shear strains, and dx and dy are the distance from the subset center to an arbitrary point within the same subset. The first order shape function is able to capture most of the deformation that could happen on a 2D surface. Numerous DIC algorithms have been developed in the past 40 years to improve the correlation between the reference and deformed subsets. The first improved algorithm was proposed by Sutton et al. [79] in 1983, where the light intensity reflected by the images can be stored as grey level from 0 to 255. A correlation coefficient, C , was determined to employ the bilinear interpolation. C can be expressed as [79]:

$$C\left(u, v, \frac{\delta u}{\delta x}, \frac{\delta v}{\delta y}, \frac{\delta u}{\delta y}, \frac{\delta v}{\delta x}\right) = \int \int [f(x) - g(x')]^2 dx \quad (5)$$

Here $u, v, \frac{\delta u}{\delta x}, \frac{\delta v}{\delta y}, \frac{\delta u}{\delta y}, \frac{\delta v}{\delta x}$ are the deformation parameters for the first-order shape functions. $f(x)$ and $g(x')$ are the intensity values in the reference and deformed images. A DIC problem can then be treated as an optimization problem. By minimizing the square of the intensity difference, the displacement parameters can be obtained by a series of iterations. Further improvements were made based on this theory to enhance the computational efficiency and accuracy. These include the Newton-Raphson method, the least square correlation method, the peak finding algorithm (fast-and-simple method), and the zero-normalized cross correlation (ZNCC) method. These methods either modify the form of the correlation coefficient, use higher-order shape functions, or use higher-order interpolation schemes. A more recent classification has been given to define two main categories of correlation criteria: 1. Cross-correlation criterion; and 2. Sum of squared difference correlation criterion. Detailed formulations and explanations of these criteria can be referred to Pan et al. [76]. In this thesis, the ZNCC criterion has been applied for correlation. The formulation of the ZNCC criterion is documented here [76]:

$$C_{ZNSSD} = \sum_{i=-M}^M \sum_{j=-M}^M \left[\frac{f(x_i, y_j) - f_m}{\Delta f} - \frac{g(x'_i, y'_j) - g_m}{\Delta g} \right]^2 \quad (6)$$

$$f_m = \frac{1}{(2M + 1)^2} \sum_{i=-M}^M \sum_{j=-M}^M f(x_i, y_j) \quad (7)$$

$$g_m = \frac{1}{(2M + 1)^2} \sum_{i=-M}^M \sum_{j=-M}^M g(x'_i, y'_j) \quad (8)$$

$$\Delta f = \sqrt{\sum_{i=-M}^M \sum_{j=-M}^M [f(x_i, y_j) - f_m]^2} \quad (9)$$

$$\Delta g = \sqrt{\sum_{i=-M}^M \sum_{j=-M}^M [g(x'_i, y'_j) - g_m]^2} \quad (10)$$

where (x_i, y_i) and (x'_i, y'_i) are the coordinates of interpolation points in the reference (undeformed) and deformed frames, respectively; f and g refer to the intensity functions; $f(x_i, y_j)$ refers to the intensity function based on the displacement field in the reference frame; $g(x'_i, y'_i)$ refers to the intensity function in the deformed frames; and $(2M + 1)$ indicates the dimensions of the subset is always odd. Note that these criteria can be used with first or higher-order shape functions (i.e., can be used in stereo-DIC or DVC), as well as lower and higher-order interpolation scheme. An interpolation scheme is used to obtain sub-pixel grayscale intensity information before applying the correlation criteria. Different interpolation schemes, including bilinear interpolation, bicubic interpolation, and bicubic B-spline interpolation have been used for DIC applications throughout the years [76]. According to Schreier et al. [80] and Knauss et al. [81], a higher interpolation scheme should always be used as it provides higher registration accuracy and better convergence character of the algorithm than the simple interpolation schemes do.

B.2 Speckle Pattern

Another important aspect of DIC is to apply a good speckle pattern, which is used to enhance the surface contrast and minimize the correlation errors. Dong and Pan [78] conducted a thorough review of the speckle pattern fabrication and assessment methods for DIC, where detailed documentation has been given for the most relevant techniques. In general, a “good” speckle pattern should contain some highly contrast, isotropic, random, and stable grayscale features to realize accurate DIC measurements [78]. Different types of speckle patterns, including nature texture patterns and artificially-made patterns can be used in DIC applications. In this thesis, an

ultrafine point airbrush with a 0.15 mm diameter nozzle has been used to apply a nondestructive sub-micron artificial pattern on the specimen surface. Detailed experimental protocol of applying speckle patterns and its optimization can be referred to Chapter 4 of this thesis, and it is omitted here.

Lastly, shown in Figure B.2 is a flow chart demonstrating the procedures to obtain the stress-strain curves in both quasi-static and dynamic tests. After all the frames are extracted to the VIC-2D 6 software (detail can be found in Chapter 4), the first image is chosen as the reference frame, where an AOI is selected based on the overall quality of the video. Appropriate settings are selected (i.e., subset size, correlation criterion, filters) before analysis, and post-analysis tools (i.e., remove rigid motion, preliminary data smoothing) are performed after each analysis. If the contour and 1-D strain-time plot are satisfied in terms of stress uniaxiality and smoothness, the strain-time data along with the stress-time data will be exported to MATLAB for matching. Peak-matching and wave-front-matching are performed for quasi-static and dynamic tests, respectively. In the dynamic experiments, the stress and strain data are matched from the triggered signal front (in contrast with peak load in quasi-static) because no single distinct point of material failure and stress-strain evolution could be traced during impact loading of the cermet. In both cases, strain data is smoothed over every three points for each of plotting and interpolation.

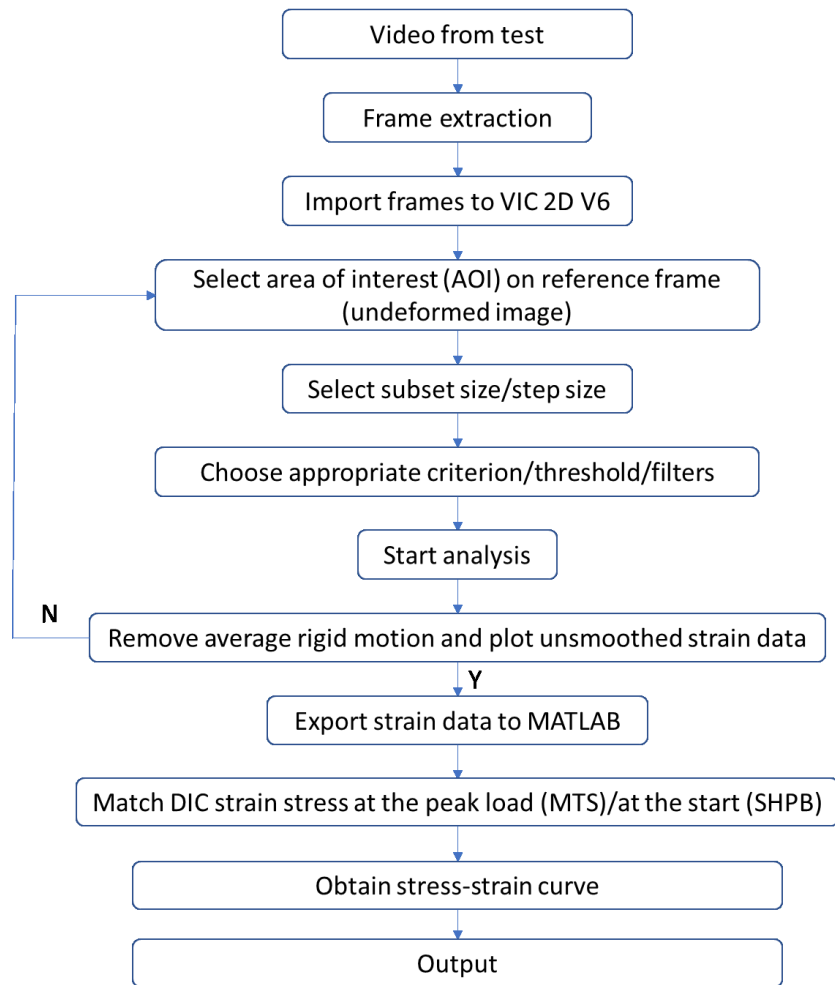


Figure B.2: Flowchart summarizing data processing procedures by using the testing apparatus coupled with digital image correlation to obtain stress-strain curves with MATLAB.

Appendix C: Supplementary Scanning Electron Microscopy/Transmission Electron Microscopy Micrographs

In this appendix, additional SEM and TEM micrographs which were not used in Chapter 3 and 4 will be presented here for the completeness of this thesis. Note that these micrographs are all for the TiAl/Ti₃Al-Al₂O₃ cermet under different conditions.

C.1 *As-received material*

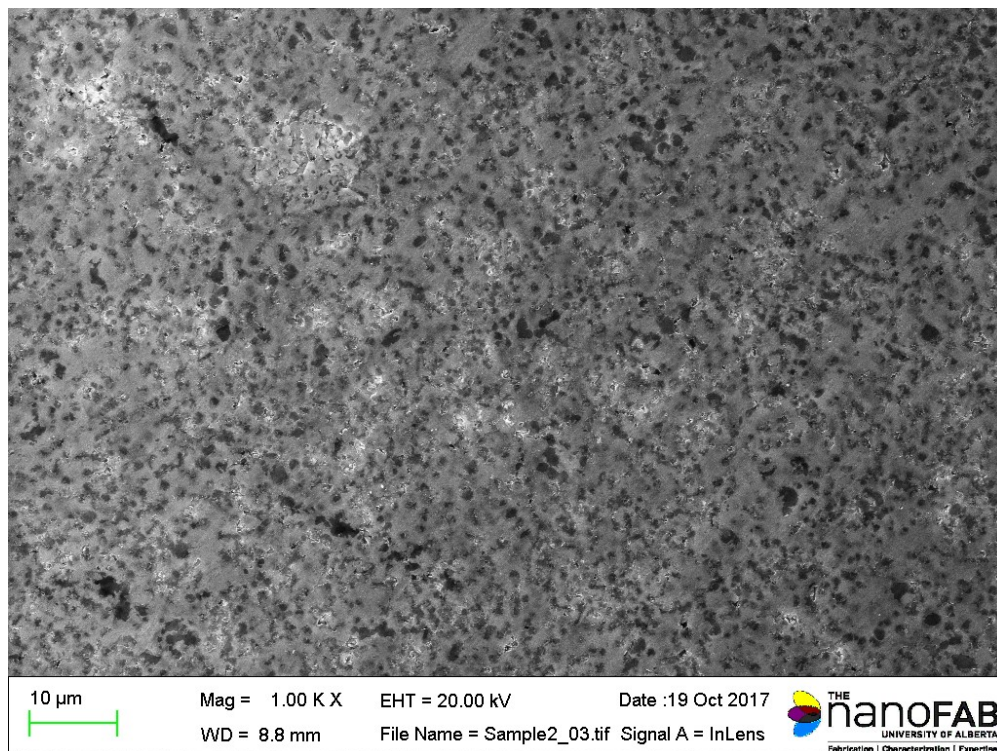


Figure C.1: FE-SEM image of polished as-received specimen surface showing surface features, such as pores and defects.

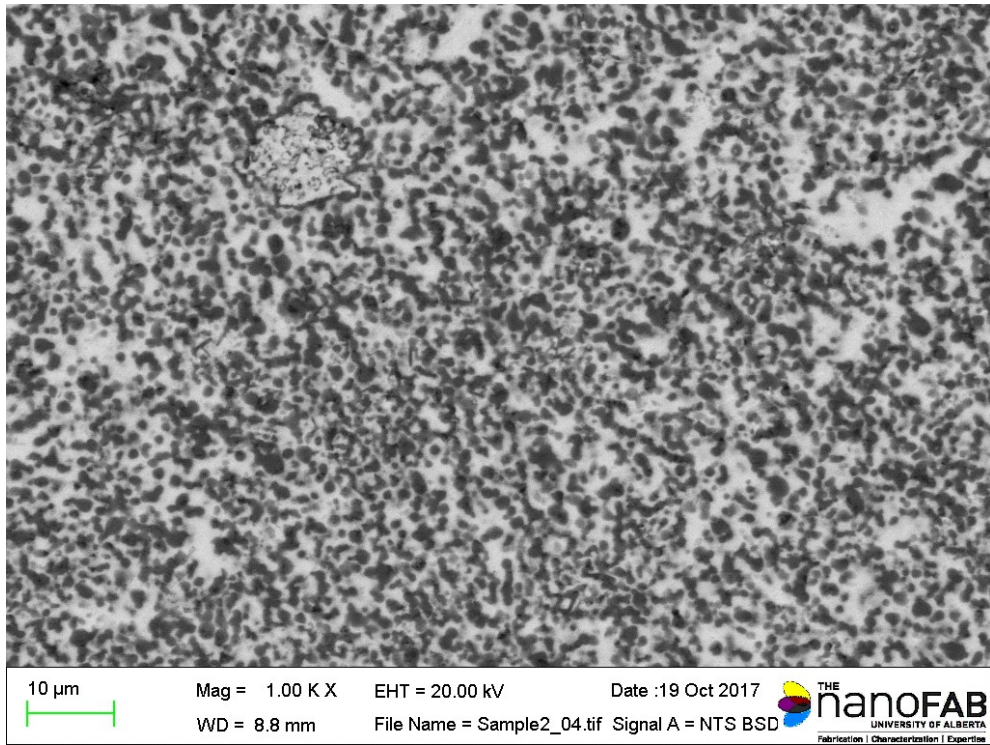


Figure C.2: The corresponding BSE-SEM micrograph of Fig. C1 showing phase distributions.

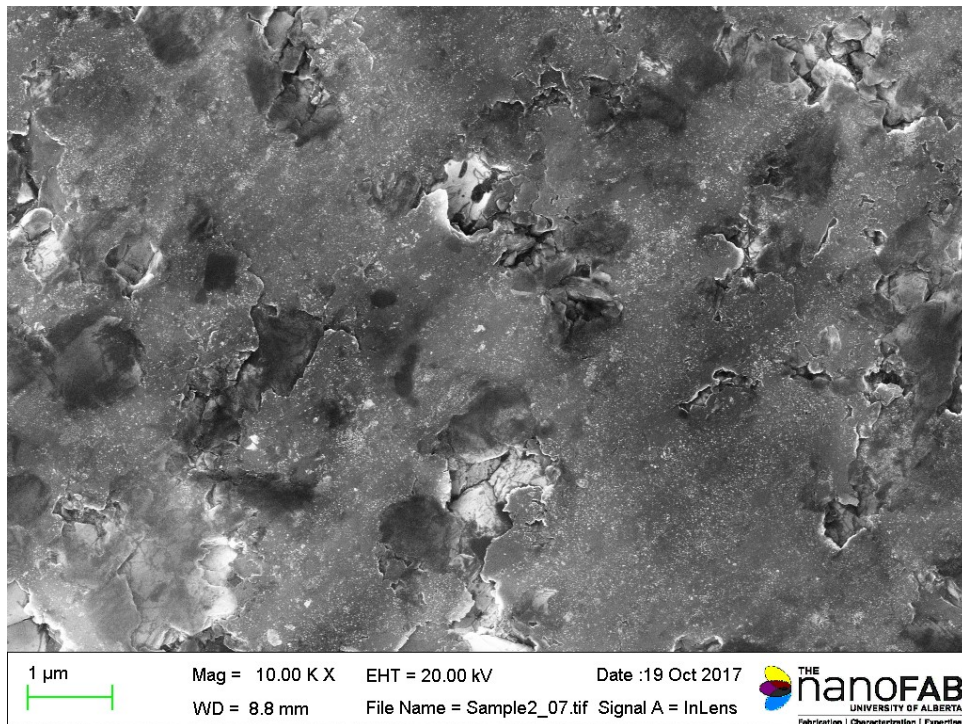


Figure C.3: FE-SEM micrograph showing a magnified view of the pores on the polished as-received specimen surface.

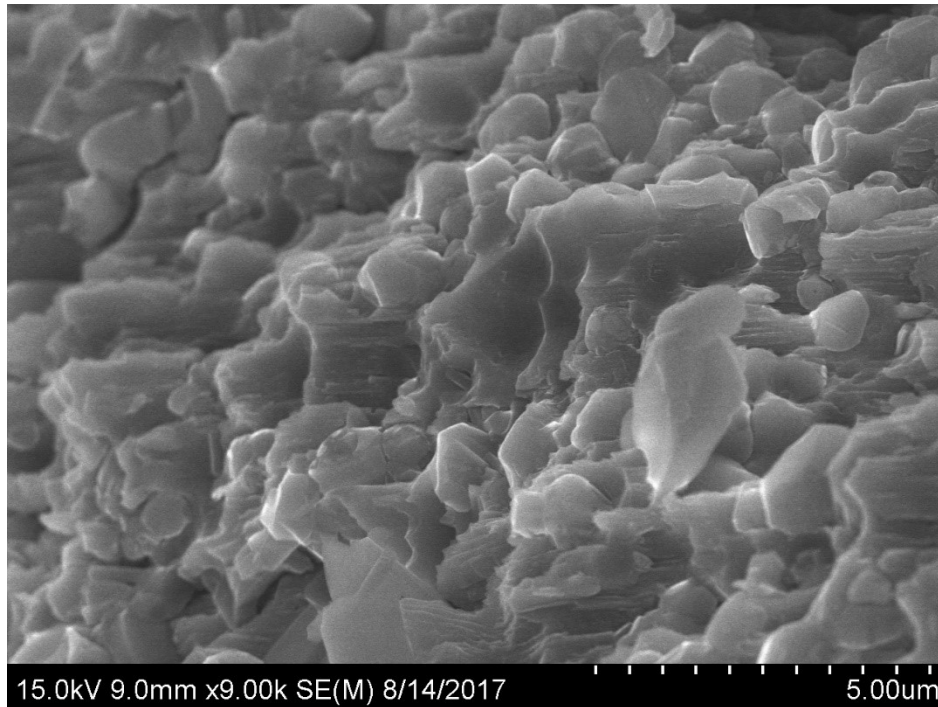


Figure C.4: FE-SEM micrograph on the fracture surface (not from testing) of the specimen showing two-phase titanium aluminide lamellar structure, equiaxed titanium aluminide and alumina grains.

C.2 Fracture surface of fragments recovered from quasi-static testing

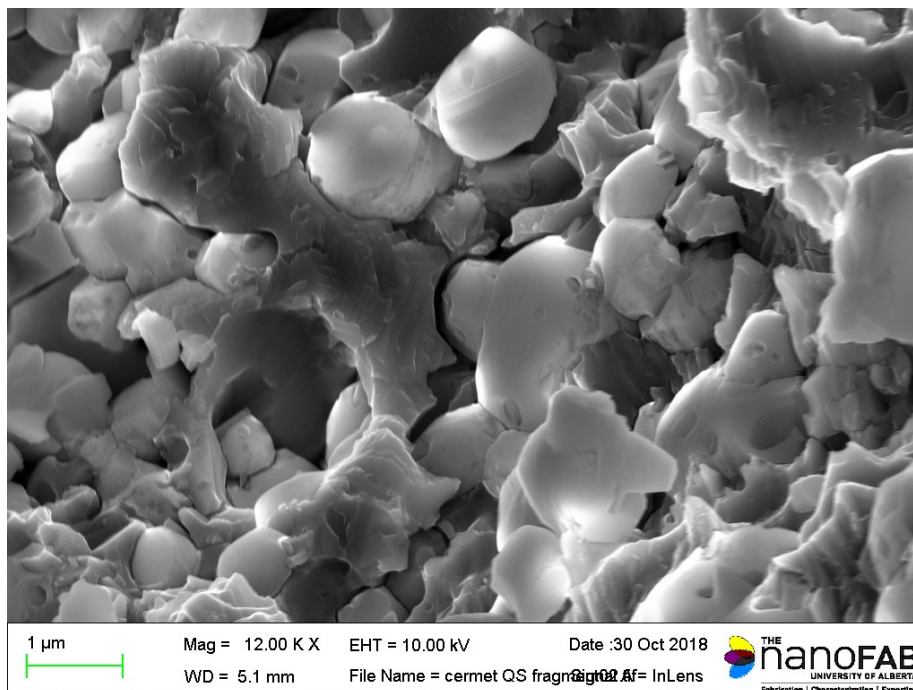


Figure C.5: FE-SEM micrograph on the fracture surface of a fragment recovered from quasi-static testing showing intergranular cracking and particle delamination.

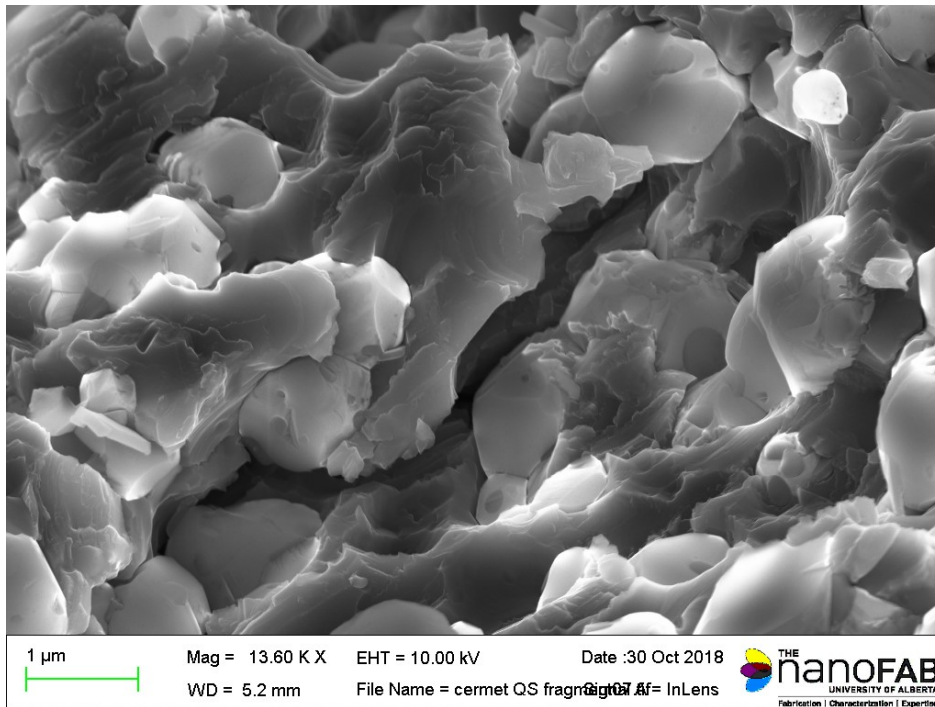


Figure C.6: FE-SEM micrograph on the fracture surface of a fragment recovered from quasi-static testing showing tearing of the titanium aluminide phase (gray color).

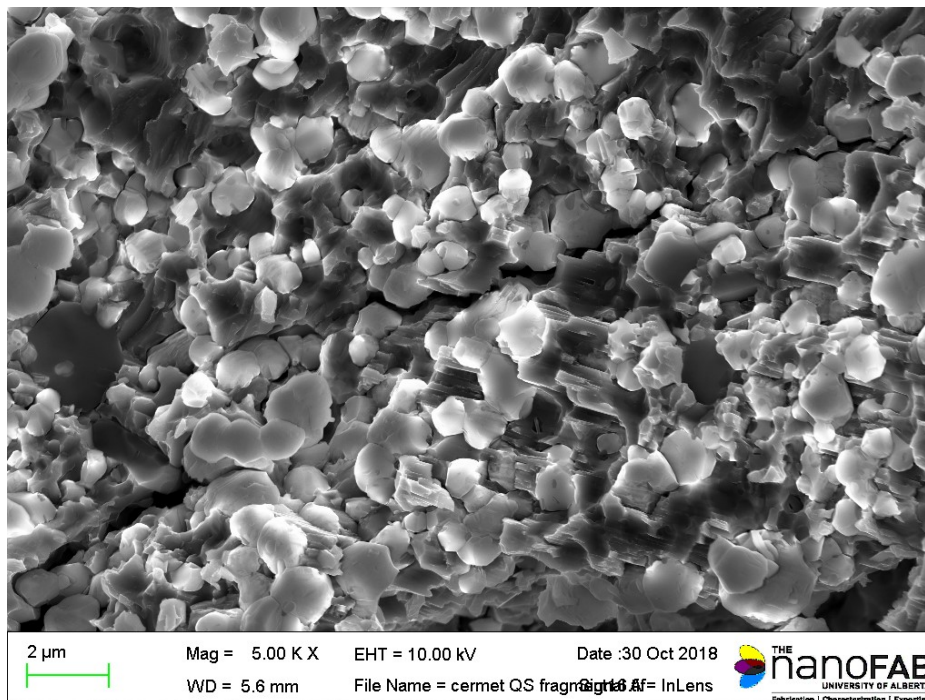


Figure C.7: FE-SEM micrograph on the fracture surface of a fragment recovered from quasi-static testing showing a dominating crack formed roughly in the direction of compression.

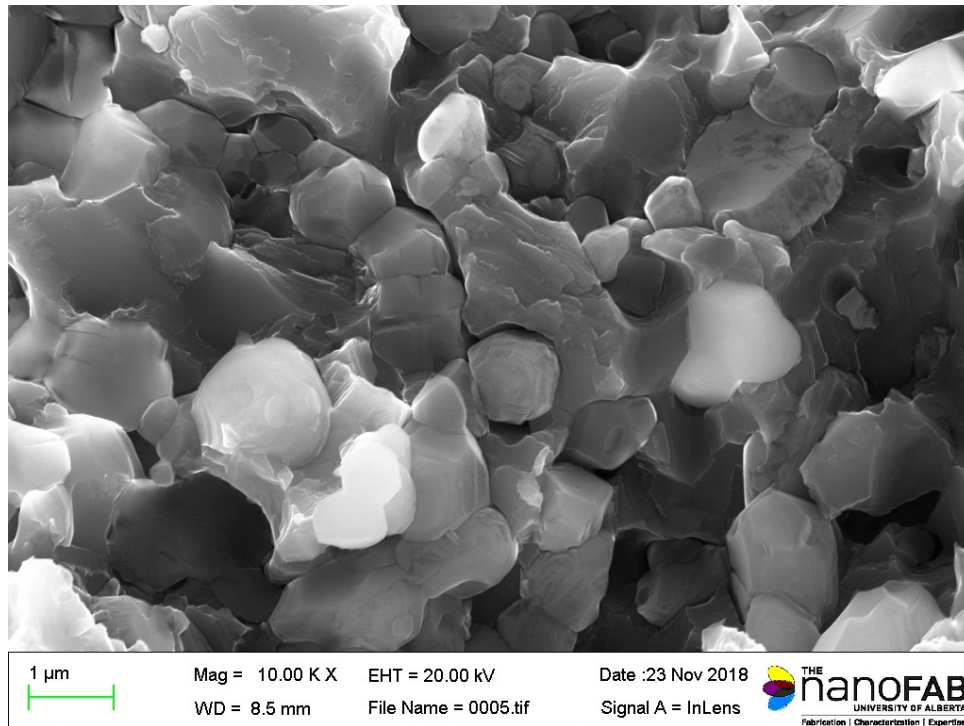


Figure C.8: FE-SEM micrograph on the fracture surface of a fragment recovered from quasi-static testing showing particle pulled-out in the vicinity of a microcrack.

C.3 Polished fracture surface of fragments recovered from quasi-static testing

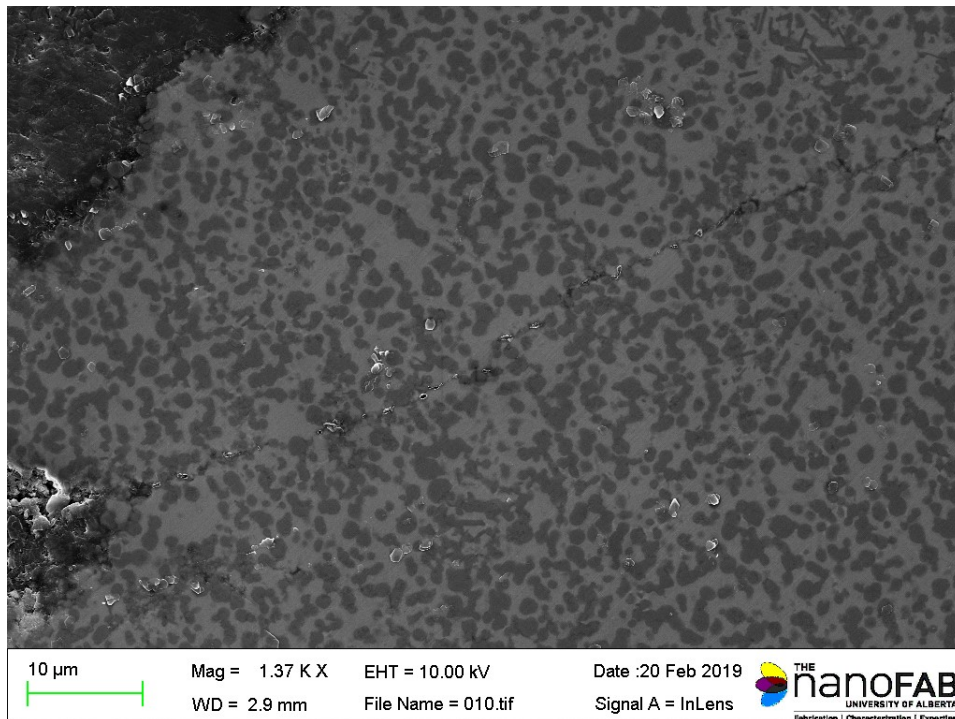


Figure C.9: FE-SEM micrograph on the polished fracture surface of a fragment recovered from quasi-static testing showing a microcrack across the field of view with voids along the path.

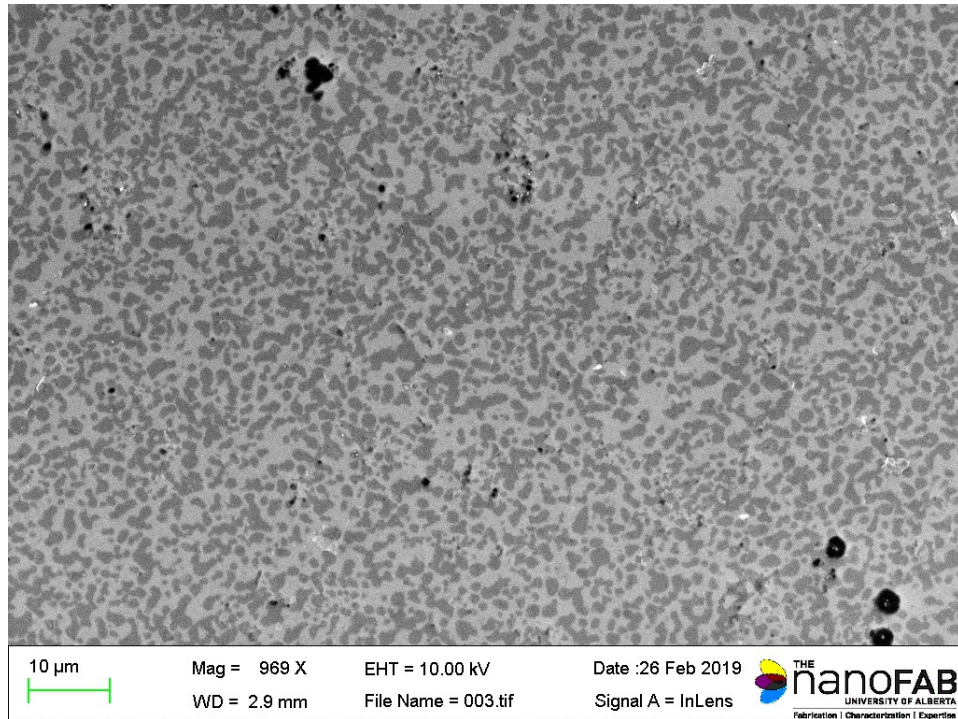


Figure C.10: FE-SEM micrograph on the polished fracture surface of a fragment recovered from quasi-static testing showing some void growth (black dots). Minimum amount of particle fractures is observed.

C.4 Fracture surface of fragments recovered from dynamic testing

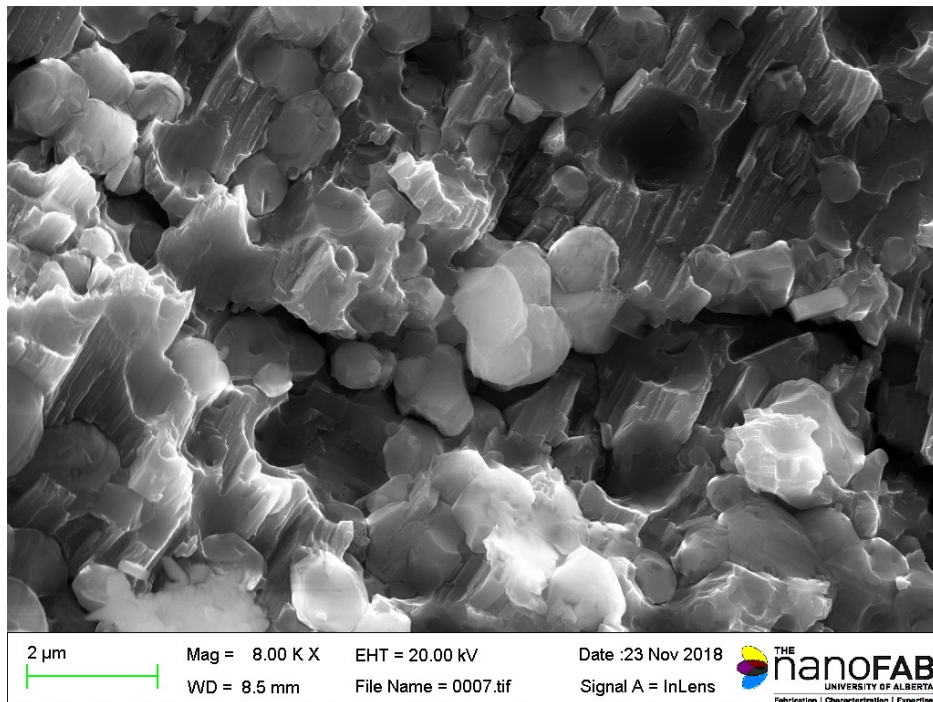


Figure C.11: FE-SEM micrograph on the fracture surface of a fragment recovered from dynamic testing showing extensive cleavage of the titanium aluminide phase and alumina particle pulled-out.

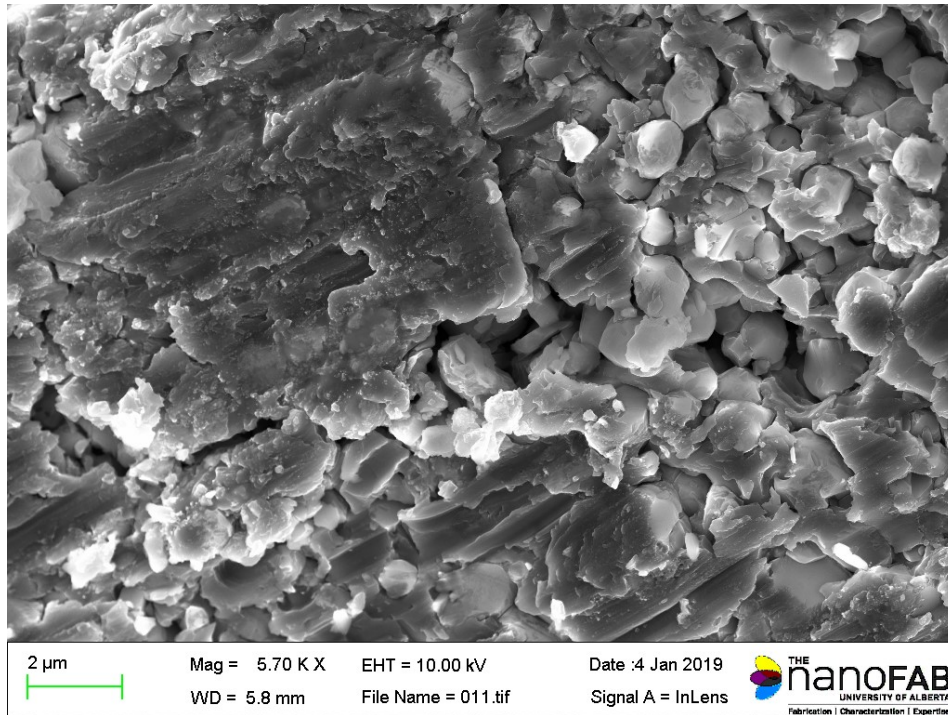


Figure C.12: FE-SEM micrograph on the fracture surface of a fragment recovered from dynamic testing showing planar tearing of titanium aluminide and alumina particle fracture.

C.5 Polished fracture surface of fragments recovered from dynamic testing

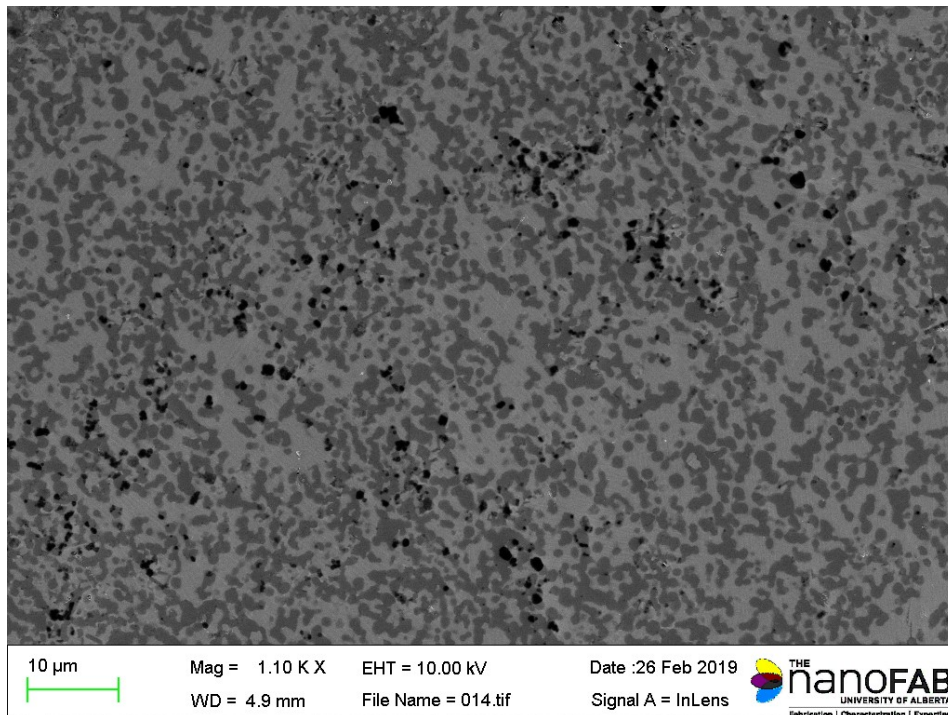


Figure C.13: FE-SEM micrograph on the polished fracture surface of a fragment recovered from dynamic testing showing extensive void growth within or surrounding the alumina phase (gray).

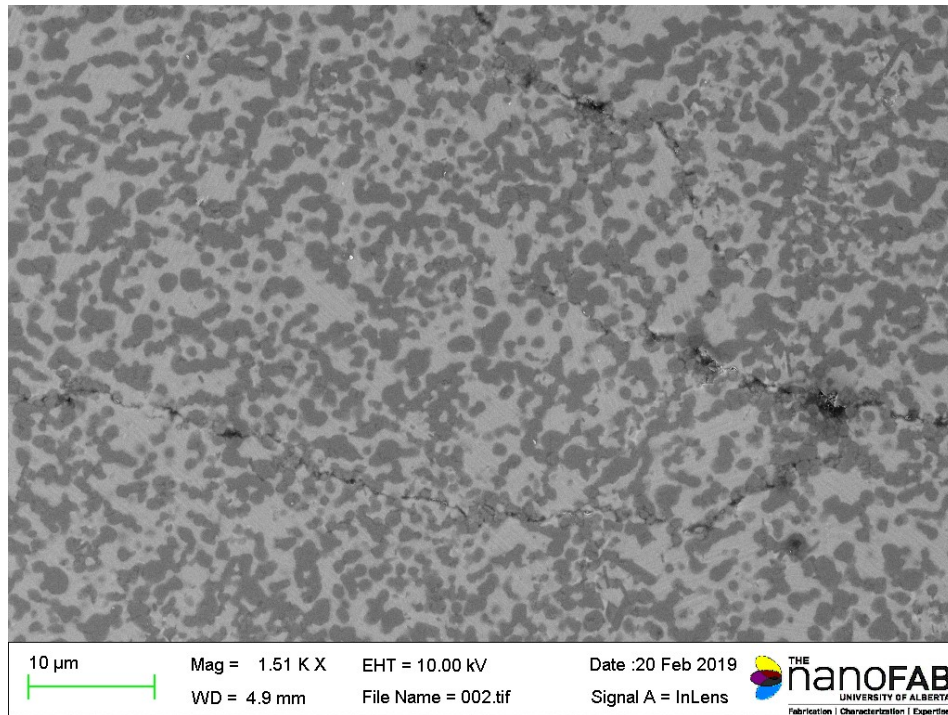


Figure C.14: FE-SEM micrograph on the polished fracture surface of a fragment recovered from dynamic testing showing a triple junction of microcracks and extensive particle fracture. Transgranular fracture is also dominant.

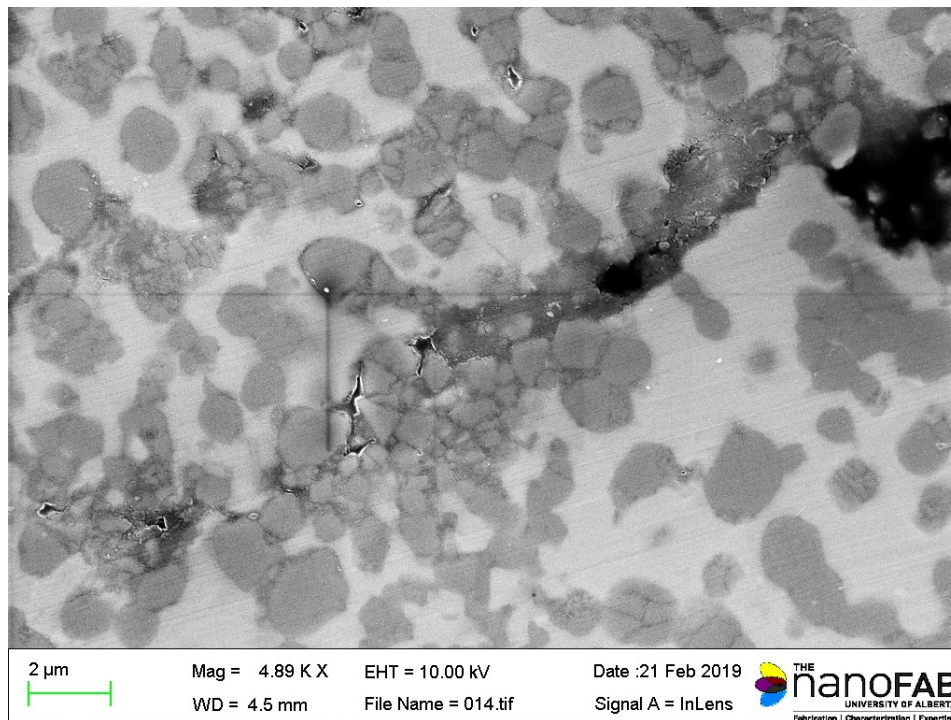


Figure C.15: FE-SEM micrograph on the polished fracture surface of a fragment recovered from dynamic testing showing a magnified view of particle fracture. The extent of particle damage along and in the vicinity of a microcrack is significant.

C.6 TEM investigation on the as-received material

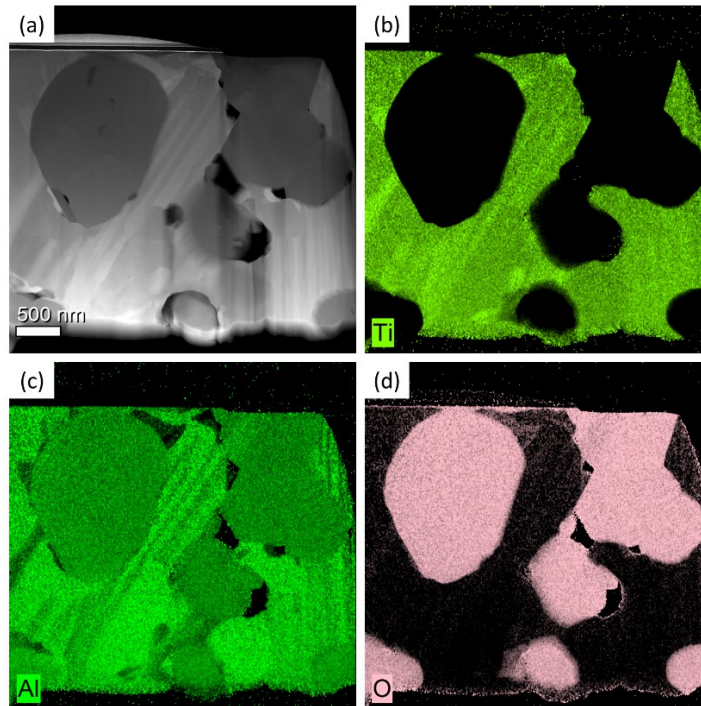


Figure C.16: (a) S-TEM micrograph on an as-received specimen showing individual alumina grains and alumina clusters (gray). The titanium aluminide phase exhibits randomly orientated lamellar structure and equiaxed grains; (b) Corresponding Ti element map of (a); (c) Corresponding Al element map of (a); (d) Corresponding O element map of (a).



Figure C.17: Bright field TEM micrograph on an as-received specimen showing a magnified view of an alumina grain, where dislocations and residual stresses resulting from manufacturing are observed.

C.7 TEM investigation on the dynamically deformed material

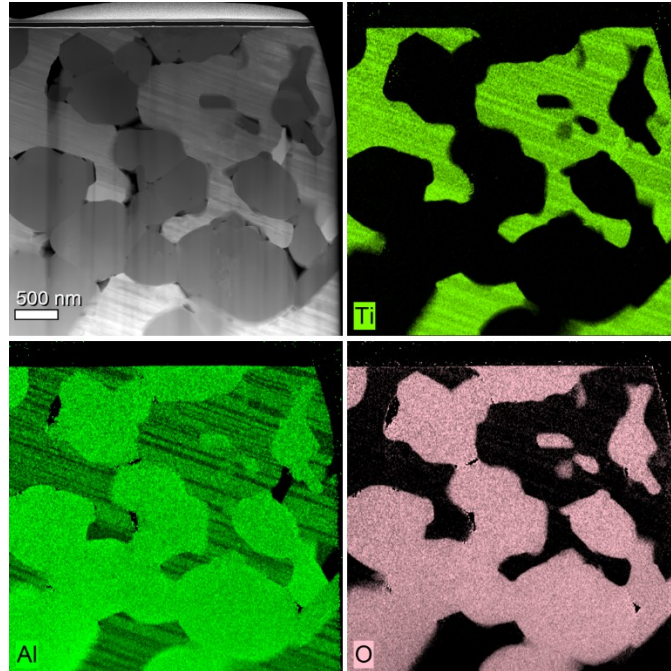


Figure C.18: (a) S-TEM micrograph on a dynamically deformed specimen showing alumina clusters (gray). The titanium aluminide phase exhibits uniformly orientated lamellar structure and no equiaxed grains is observed; (b) Corresponding Ti element map of (a); (c) Corresponding Al element map of (a); (d) Corresponding O element map of (a).

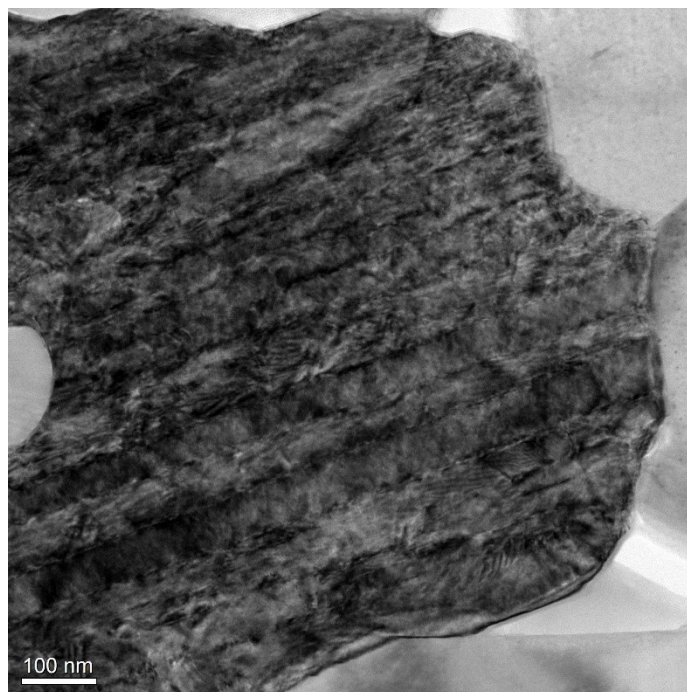


Figure C.19: Bright field TEM micrograph on a dynamically deformed specimen showing uniformly orientated ($\gamma + \alpha_2$) titanium aluminide lamellar structure with extensive dislocations located in between the lamella.

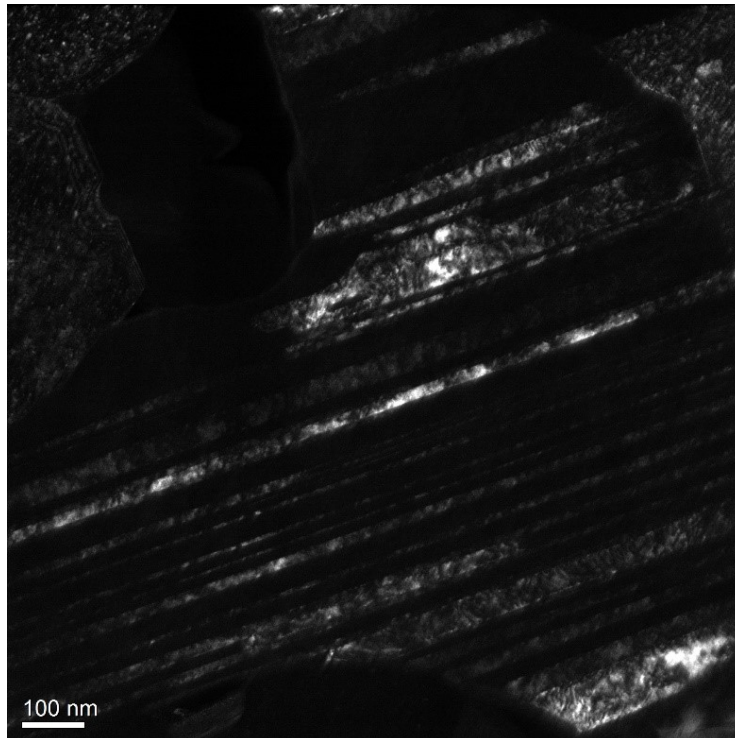


Figure C.20: Dark field TEM micrograph on a dynamically deformed specimen focusing on the lamellar structure. A large variation of lamellar width is observed. EDS examination demonstrates an alternating γ/α_2 feature.

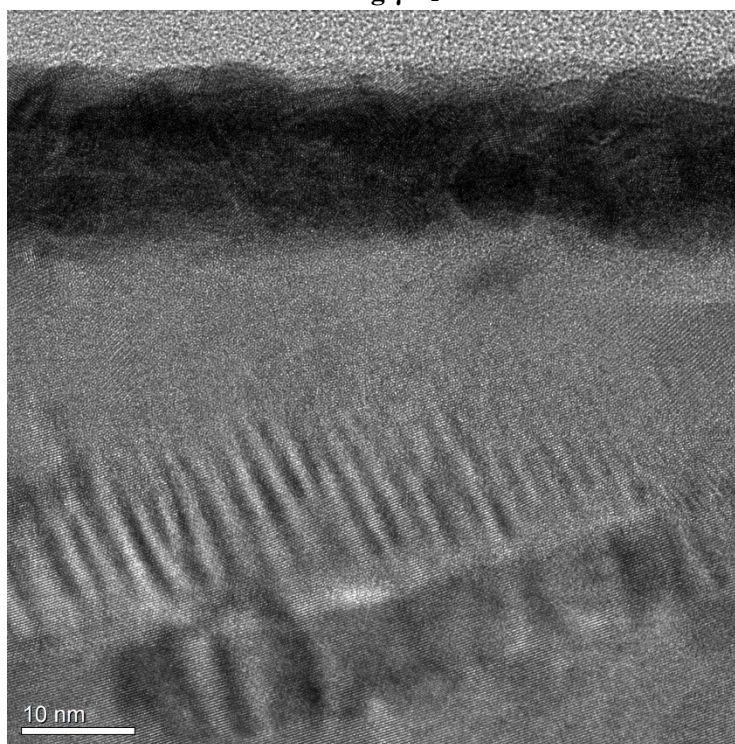


Figure C.21: Bright field TEM micrograph on a dynamically deformed specimen showing twinning within a lamellae.

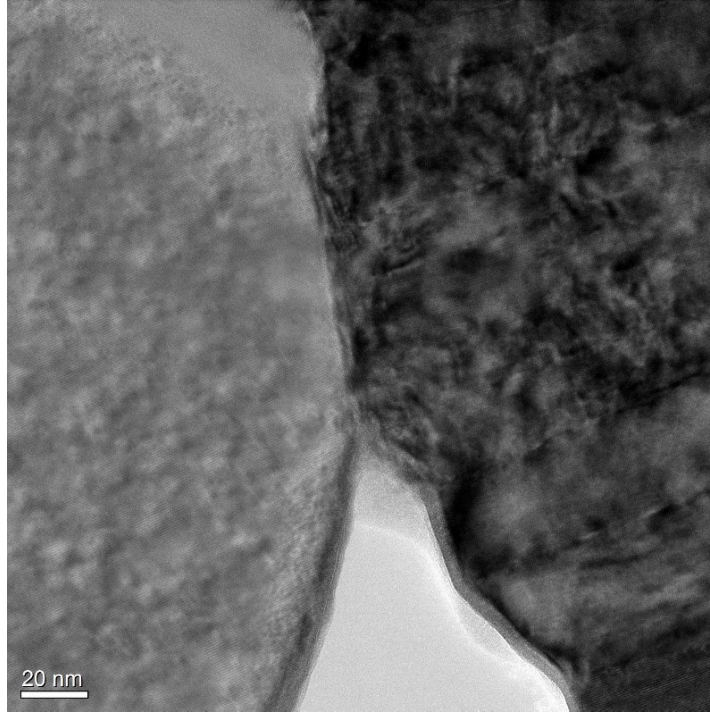


Figure C.22: High-resolution TEM micrograph on a dynamically deformed specimen showing dislocation pileup at the alumina (white)-titanium aluminide (black) interface.